

DISSERTATION

SUBMITTED TO THE
COMBINED FACULTY OF MATHEMATICS, ENGINEERING AND
NATURAL SCIENCES
OF HEIDELBERG UNIVERSITY, GERMANY
FOR THE DEGREE OF
DOCTOR OF NATURAL SCIENCES

Put forward by

Tobias Dieter Schmitt

Born in Weinheim, Germany

Oral examination: 08.02.2024

An Open-Path Observatory for Greenhouse Gases based on High Resolution Fourier Transform Spectroscopy

Tobias Dieter Schmitt

Referees: PROF. DR. ANDRÉ BUTZ
PROF. DR. WERNER AESCHBACH

Kurzfassung

Messungen atmosphärischer Treibhausgase (THGs) wie zum Beispiel Kohlendioxid (CO_2) und Methan (CH_4) tragen entscheidend dazu bei unsere Kenntnisse von THG Quellen und Senken zu verbessern. Dies ist nicht nur wichtig um unser Klimasystem besser zu verstehen, sondern auch um anthropogene Emissionen von THGs zu quantifizieren, zu überprüfen und zu attribuieren. Hierfür sind urbane Räume von besonderer Wichtigkeit, stellen aber aufgrund der stark strukturierten Emissionsmuster eine besondere Herausforderung dar. Hier stelle ich die Entwicklung, Konstruktion und Implementierung eines Langpfad-Observatoriums vor, das THG Konzentrationen entlang eines 1.55 km langen Pfades gemittelt misst. Ich analysiere die Leistungsfähigkeit des Aufbaus und vergleiche sie mit In-situ-Messungen um Schlussfolgerungen über die jeweilige Repräsentativität der beiden Messmethoden auf der Kilometerskala zu ziehen.

Bei fünf minütig gemittelten Mischungsverhältnissen erreicht das Langpfad-Observatorium Präzisionen von 1.4 ppm (0.32 %) für CO_2 und 8.3 ppb (0.40 %) für CH_4 . Insgesamt stimmen die Langpfad- und In-situ-Messungen gut überein, aber für bestimmte Bedingungen, wie zum Beispiel Südostwinde treten Unterschiede von bis zu 20 ppm für CO_2 auf. Solche Unterschiede könnten Emissionsschätzungen, die typischerweise mittels Verknüpfung von Messungen mit atmosphärischen Transportmodellen auf Kilometerskalen errechnet werden, erheblich beeinträchtigen. Ich lege dar, dass die Messungen des Langpfad-Observatoriums eine solide Basis für weitere Analysen zur Frage der Repräsentativität von Konzentrationsmessungen bilden und einzigartige Möglichkeiten zur Validierung und Verbesserung spektroskopischer Datenbanken bieten und des Langpfad-Observatoriums dadurch allgemein zu Verbesserungen im Bereich der atmosphärischen Fernerkundung von THG beitragen kann.

Abstract

Measuring the atmospheric concentrations of greenhouse gases (GHGs) like carbon dioxide (CO_2) and methane (CH_4) is crucial to improve our knowledge of their sources and sinks. This is essential to understand our climate system, but also to quantify, verify, and attribute anthropogenic emissions of GHGs. For the latter, urban areas are particularly important, but pose unique challenges due to often highly structured emission patterns. Here, I present the design, setup, and implementation of an open-path observatory, which measures averaged GHGs concentrations along a 1.55 km long path and evaluate its performance. I compare these measurements to in-situ measurements to evaluate their respective representativeness on a kilometer-scale grid.

Averaging over five minutes, the open-path observatory achieves precisions of 1.4 ppm (0.32 %) and of 8.3 ppb (0.40 %) for CO_2 and CH_4 dry air mole fractions, respectively. Overall, the open-path and in-situ measurements agree well, but I also identify conditions, such as south-easterly winds, where discrepancies of up to 20 ppm occur in CO_2 . Such differences can seriously impact emission estimates obtained from pairing measurements with kilometer-scale atmospheric transport models. I demonstrate that the observatory can provide a sound measurement basis for further investigations into the representativeness issue and offers unique opportunities to validate and improve spectroscopic databases. Both can contribute to general improvements to atmospheric remote sensing of GHGs.

Publications

- **Schmitt, T. D.**, Kuhn, J., Kleinschek, R., Löw, B. A., Schmitt, S., Cranton, W., Schmidt, M., Vardag, S. N., Hase, F., Griffith, D. W. T., and Butz, A.: An open-path observatory for greenhouse gases based on near-infrared Fourier transform spectroscopy, *Atmos. Meas. Tech.*, 16, 6097–6110, <https://doi.org/10.5194/amt-16-6097-2023>, 2023.
- Löw, B. A., Kleinschek, R., Enders, V., Sander, S. P., Pongetti, T. J., **Schmitt, T. D.**, Hase, F., Kostinek, J., and Butz, A.: A portable reflected-sunlight spectrometer for CO₂ and CH₄, *Atmos. Meas. Tech.*, 16, 5125–5144, <https://doi.org/10.5194/amt-16-5125-2023>, 2023.

Contents

Publications	i
List of Figures	viii
List of Tables	ix
Acronyms	xi
1 Introduction	1
2 Molecular Spectra in the Atmosphere	9
2.1 The Origin of Discrete Spectral Lines	10
2.2 Description of Molecules and Vibration-Rotation Spectra	13
2.2.1 Molecular Vibration	14
2.2.2 Molecular Rotation	15
2.2.3 Combined Vibration-Rotation Spectra	17
2.2.4 Relevant Transition Bands	20
2.3 Profiles of Isolated Lines	23
2.3.1 Doppler Broadening	24
2.3.2 Pressure Broadening	24
2.3.3 The Voigt Profile	25
2.3.4 Advanced Line Profiles	25
2.4 Collisional Line Mixing	26
2.5 Collision Induced Absorption	27
2.6 Absorption Spectroscopy	28
3 Operating Principle of Fourier Transform Spectrometry	31
3.1 Concept of a Fourier Transform Infrared (FTIR) Spectrometer	31
3.2 Resolution of a FTIR Spectrometer	34
3.3 Optical Throughput and Self-Apodization	35
3.4 Sampling the Interferogram	38

3.5	Technical Implementations	39
3.5.1	Cube Corner Interferometers	39
3.5.2	Rapid-Scan Interferometers	40
3.5.3	Detectors and Detector Readout Electronics	41
3.6	From Interferogram to Spectrum	44
3.6.1	Apodization	44
3.6.2	Phase Correction	45
3.7	Instrument Line Shape (ILS)	47
4	Methods	51
4.1	Open-Path Setup	51
4.1.1	Location	51
4.1.2	Open-path optics	53
4.1.3	Spectrometer	56
4.1.4	Detectors and Detector Optics	57
4.1.5	Instrument Settings	61
4.1.6	Resulting Spectrum	62
4.2	Trace Gas Retrieval	62
4.2.1	Absorption Cross-Sections	65
4.2.2	Retrieval Configurations	65
4.2.3	ILS	66
4.3	Dry Air Mole Fractions	66
4.4	Precision of Time Series	67
4.5	Bias Correction to in-situ Data	68
5	Results	71
5.1	Overview of the 2023 Campaign	71
5.2	Detector Performances	72
5.2.1	Spectra and Noise Performance	72
5.2.2	Timeseries and Target Gas Performance	76
5.3	Comparison of Different Modes of Operation	79
5.3.1	Spectrum and Fit Quality	79
5.3.2	Time Resolution	81
5.3.3	Direct Comparison of Target Gas Performance	85
5.4	Optimal Operation Configurations	86
5.5	Open-Path Measurements of Carbon Dioxide and Methane	88
5.5.1	Path Average Temperature and Line Mixing	88
5.5.2	Mole Fractions	92

5.5.3	ILS Fluctuations	93
5.6	Comparison of Open-Path and In-Situ Measurements	95
5.6.1	Diurnal Cycle	96
5.6.2	Statistical Analysis	100
5.6.3	Wind Direction Dependency	102
5.6.4	Implication of the Instrument Differences for Emission Es- timations.	107
6	Summary and Conclusion	111
	Acknowledgements	115
	Bibliography	119

List of Figures

2.1	Morse potential and harmonic approximation with vibrational states.	15
2.2	P, Q, and R branch of a vibrational rotational transition.	19
2.3	Exemplary transmission spectrum for a vibrational rotational transition.	20
2.4	Morse potential for the ground state and first electronic excited state of O ₂	23
3.1	Schematic of a Fourier Transform Spectrometer.	32
3.2	Calculation of an ILS according to the simple model.	50
4.1	Location of the absorption path.	52
4.2	Roof top observatory and night time view of reflector array.	53
4.3	Schematic of the open-path optics.	54
4.4	Picture of the reflector array.	56
4.5	Schematic of the custom detector electronics.	59
4.6	Typical IFG with TE detector at 0.55 cm ⁻¹ resolution.	63
4.7	Typical spectrum with TE detector at 0.55 cm ⁻¹ resolution.	64
4.8	Bias correction of xCO ₂ and xCH ₄ open-path measurements.	69
5.1	Example spectrum with RT detector at 0.55 cm ⁻¹ resolution.	73
5.2	Noise performance comparison for RT and TE detector.	75
5.3	xCO ₂ and xCH ₄ as measured with the RT and the TE detector.	77
5.4	xCO ₂ and xCH ₄ as measured with the RT and the TE detector. Zoom in transition period.	78
5.5	Typical example of a spectrum measured in high resolution mode (resolution of 0.11 cm ⁻¹).	80
5.6	Spectrum and residual for benchmark measurements.	82
5.7	Spectrum and residual for high resolution measurements.	83
5.8	Allan deviations for xCO ₂ and xCH ₄ for open-path in one minute mode and in-situ measurements.	84
5.9	Fixed and fitted temperature in comparison.	89
5.10	Fit residuals for fixed and fitted temperature.	91

5.11 Full timeseries of $x\text{CO}_2$ and $x\text{CH}_4$ for open-path and in-situ measurements.	97
5.12 Ten days of $x\text{CO}_2$ and $x\text{CH}_4$ open-path and in-situ measurements. .	98
5.13 Diurnal cycle of $x\text{CO}_2$ for weekdays and weekends.	99
5.14 Histogram of differences between open-path and in-situ measurements of $x\text{CO}_2$ and $x\text{CH}_4$	101
5.15 Overview of methane emissions in Heidelberg.	102
5.16 Example for night time $x\text{CO}_2$ enhancement of in-situ measurements compared to open-path results.	103
5.17 Differences between open-path and in-situ measurements of $x\text{CO}_2$ and $x\text{CH}_4$ by wind direction.	105
5.18 Emission map of anthropogenic CO_2 in the region around Heidelberg.	106
5.19 Simulated night time wind field in the city of Heidelberg.	108

List of Tables

4.1	Settings for the FTIR instrument.	61
4.2	Spectral windows and corresponding fitted trace gases.	66
4.3	Bias correction factors for open-path $x\text{CO}_2$ and $x\text{CH}_4$ measurements.	70
5.1	Overview of the employed instrument settings.	72
5.2	Theoretical noise contributions for RT and TE detector.	74
5.3	Precision of 5 min gas measurements for RT and TE detector.	79
5.4	Precision of gas measurements for the different operation modes, after resampling on a 5 min grid.	86
5.5	Relative precisions of measured total CDs and dry air mole fractions.	92
5.6	Sensitivity of retrieved trace gas results on ILS modulation efficiency.	94

Acronyms

ADC analog to digital converter

BS beam splitter

CRDS cavity ring-down spectroscopy

CIA collision induced absorption

CD column density

EM electromagnetic

EMI electromagnetic interference

FFT fast Fourier transform

FOV field of view

FT Fourier transform

FTIR Fourier-transform infrared spectroscopy

FWHM full width at half maximum

GHG greenhouse gas

HWHM half width at half maximum

HTP Hartmann-Tran profile

HITRAN high-resolution transmission molecular absorption database

InGaAs indium gallium arsenide

IUP Institute of Environmental Physics

ILS instrument line shape

IFG interferogram

MCT mercury cadmium telluride

MIR mid infrared

NIR near infrared

NBM Norton-Beer medium

NBS Norton-Beer strong

NBW Norton-Beer weak

OPI old building of the physics institute

OPD optical path difference

RANS Reynolds-averaged Navier-Stokes

RT room temperature

SNR signal to noise ratio

SDV speed-dependent Voigt

TE thermoelectric

UV ultraviolet

ZPD zero path difference

1 Introduction

Earth and humankind currently experience a rapid climate change, which is driven by anthropogenic emissions of greenhouse gases (GHGs) (Intergovernmental Panel On Climate Change, 2023). The rate at which global surface temperature has changed in the last decades is unprecedented over at least the last 2000 years (e.g., Mann et al., 1999; Mann, 2007; Rohde and Hausfather, 2020) and the current climate state is most likely the hottest in the current interglacial period (Kaufman and McKay, 2022). Anthropogenic emissions of GHGs are by far the dominant driver for this development (Haustein et al., 2017, 2019; Gillett et al., 2021), with carbon dioxide (CO₂) and methane (CH₄) contributing the most (Etmann et al., 2016). Currently, the atmospheric concentration of both are higher than within at least the last 800 000 years (Lüthi et al., 2008; Loulergue et al., 2008; Schilt et al., 2010; Jouzel, 2013; Keeling and Keeling, 2017). The changing climate is already affecting humankind across the globe, for example in the form of more frequent extreme weather events like heatwaves, storms, and heavy precipitation (e.g., Collins et al., 2010; Shepherd, 2014; Diffenbaugh and Scherer, 2011). These effects will continue to increase in frequency and intensity, and will pose a substantial challenge or even threat to large parts of the global population (Xu et al., 2020).

Because of this outlook, the international community has pledged itself to limit global warming below 2.0 °C, ideally below 1.5 °C, with respect to the period of 1850–1900 (Paris Agreement, United Nations Framework Convention on Climate Change (UNFCCC), 2015). It is possible, that the warming already exceeds this goal of 1.5 °C by now. Hence, decisive action in form of substantial reductions of CO₂ and CH₄ emissions is required (Intergovernmental Panel On Climate Change, 2022). But effective, efficient, and informed policy decisions must rely on a solid database and on independent monitoring and evaluation thereof. A large part of the current data base relies on bottom up calculations on a yearly and national basis. But since many policies are implemented and take effect on smaller scales, direct measurements of GHG fluxes are desirable and would furthermore significantly extend the toolbox for independent monitoring (?Mueller

et al., 2021).

This is especially the case for urban areas, which are a major and growing contributor to anthropogenic GHG emissions (Marcotullio et al., 2013). As a result, the reduction of direct and indirect urban emissions are the target of many mitigation strategies and efforts (e.g., “EU Covenant of Mayors for Climate & Energy”). But it is necessary to independently validate and monitor the reported emissions of cities by measurement driven methods, since the reported emission inventories contain considerable uncertainties (Gurney et al., 2021). Further, improving on these uncertainties and on the temporal and spatial resolution of the existing emission inventories can help policy makers to achieve their emission goals (Gurney and Shepson, 2021; Jungmann et al., 2022). The ideal tool to achieve this improvement would be a spatially resolved measurement of GHG emissions within urban areas in real time.

The measurement basis for such validation efforts can come in the form of fluxes or concentrations. Fluxes are typically measured with eddy covariance instruments on flux towers (Swinbank, 1951; Rebmann et al., 2018), but their measurement principle relies on spatially homogeneous conditions (Aubinet et al., 1999). Thus, in heterogeneous environment like urban areas, the attribution of the measured fluxes to emissions is situation specific and depends most obviously on the atmospheric state (e.g., Velasco and Roth, 2010; Davis et al., 2017; Stagakis et al., 2019, 2023). Concentration measurements can also provide a handle on emissions, since the observed atmospheric enhancement is directly linked to the integrated emissions (e.g., Gurney et al., 2002; Rodenbeck et al., 2003; Beck et al., 2013; Wang et al., 2018; Kostinek et al., 2021; Luther et al., 2022; An et al., 2022; Chandra et al., 2022; Chevallier et al., 2022). As a result, both types of measurements require knowledge about atmospheric transport to translate their information to emissions. Only simulations can provide this transport information at the required level of detail, especially in complex and heterogeneous environments like urban areas (Davis et al., 2017; Shekhar et al., 2020). Mesoscale transport models (Grell et al., 2005; Baklanov et al., 2014; Rieger et al., 2015) on grid scales of 10 km are a well established tool for providing the atmospheric transport component for emission estimates (Wang et al., 2006; Brioude et al., 2011, 2013). Since a higher spatial resolution is preferable to resolve subscale processes (Gerbig et al., 2008), these models are more and more operated on grid scales of 1 km (Shin and Dudhia, 2016; Zheng et al., 2019; Park et al., 2020), especially for urban areas (Staufer et al., 2016; Sargent et al., 2018; Zhao et al., 2019), and recently on even smaller scales (Zhao et al., 2023). Modelling atmospheric transport at

such small scales poses unique challenges, for example with the parameterization of turbulence (Kountouris et al., 2018) or the necessity to simulate even the topography of buildings and street canyons (Zhong et al., 2016). At the extremely local end, Reynolds-averaged Navier-Stokes (RANS) models are now capable of city scale simulations on 10 m grids (Berchet et al., 2017a; Vardag and Maiwald, 2023). Emission estimates from measurements are typically based on atmospheric inversion calculations with such transport models. Drastically simplified, these calculations perform a forward run of the model, where the measurements are simulated based on *a priori* knowledge of the emissions. In the inversion step, the emissions are then adapted to best fit the observations. The increasing spatial resolution of the transport models increases also the requirements on the *a priori* information, since every inversion requires some knowledge on spatial and temporal structure of the emissions, due to the finite information content of the measurement (Kaminski et al., 2001). Spatially (and temporally) resolved emission inventories typically provide this *a priori* information, but also their resolution varies significantly and spans scales from 100 km (e.g., Sindelarova et al., 2022), via 10 km (e.g., Solazzo et al., 2021; Dou et al., 2023) and 1 km (e.g., Oda et al., 2018), down to the street level (e.g., Ulrich et al., 2023). They also differ vastly in their aggregation methods, accuracy, and sector resolution (Oda et al., 2019; Super et al., 2020), especially on the urban/city scale (Arioli et al., 2020). The continuously improving resolution and quality of both, atmospheric transport models and emission inventories, allows for increasingly better predictions of atmospheric measurements. This in turn might bring increasing interest to the question if the measurements themselves are representative for the spatial scale their information is used on.

There are different methods to measure GHG concentrations in and around a source region of interest for the purpose of emission quantification. Satellite missions like GOSAT and OCO-2 cover large parts of the globe on a regular basis with spectroscopic remote sensing of the atmosphere (e.g., Butz et al., 2011; Hammerling et al., 2012; Hakkarainen et al., 2016; Hu et al., 2018). Their trade offs are a comparatively low spatial resolution and they typically rely on sunlight. They are often in a sun-synchronous orbit, which means they revisit the same site only on a fixed time of the day. This can introduce sampling bias. They are especially useful for analysis of GHG fluxes on the continental and sub-continental scale (e.g., Frankenberg et al., 2008; Basu et al., 2013; Metz et al., 2023), but also demonstrated applicability to urban areas and similar targets (e.g., Kort et al., 2012; Nassar et al., 2017; Kiel et al., 2021). It is possible for space-borne measure-

ments to achieve spatial resolutions on the scale of tens of meters, but their typical application is the quantification of strong point source emissions, rather than area fluxes (e.g., Guanter et al., 2021; Cusworth et al., 2021). A related remote sensing technique are ground based sun-viewing spectrometers, which also sound the full atmosphere column (Wunch et al., 2010, 2011; Gisi et al., 2012). They also rely on sunlight, but due to their stationary nature can provide a densely sampled record during daylight hours for a single point in space. Because of this, they are typically operated in networks (e.g., Hase et al., 2015; Frey et al., 2019) to provide measurements over a region of interest. The most localized measurement technique are in-situ sensors (Bousquet et al., 1996; Derwent et al., 2002; Masarie et al., 2014; Keeling and Keeling, 2017). They measure concentrations at a single point, at high temporal resolution and around the clock. Due to their nature of sampling air from a point it is usually possible to calibrate them against known standard gas mixtures. This allows *a posteriori* correction of inaccurate measurements and instrument drifts and enables in-situ systems to produce highly accurate results (e.g., Hall et al., 2021). To estimate emissions, they can be deployed in networks (e.g., Shusterman et al., 2016) or on moving platforms (e.g., Fiehn et al., 2020). Since they only sample air in the lower troposphere, they are more sensitive to local emissions than the two remote sensing techniques above, which average over the full atmospheric column. On the other hand their concentration measurements are so localized, that it is unclear how representative these are for the spatial grid cells of the transport models they are coupled with to estimate emissions. Remote sensing GHG concentrations integrated along a horizontal path combines these two features: Such a measurement is sensitive to local emission patterns and inherently averages the concentration on hundreds or thousands of meters, matching the grid scales of atmospheric transport models.

These horizontal path integrated measurements (called open-path measurements within this work) have the following characteristics: They rely on artificial light sources instead of the sun and can provide measurements around the clock. They rely on spectroscopic information to calculate gas amounts from the measured spectra and are as accurate as the utilized spectral database. And as already mentioned, they are only sensitive to concentrations in the lower atmospheric layer and inherently operate on the spatial scales of atmospheric transport models. This puts them in a promising middle ground between highly localized, sensitive and available in-situ measurements and spatially averaged, less sensitive and less available remote sensing techniques. Thus, they are an interesting candidate to build a bridge in two related fields of local and regional emission

estimates: They could bridge the measurement gap between in-situ and satellite measurements and help to develop methods to best synthesize the information from the two most widely used measurement types. And they could provide a bridge between atmospheric transport models and in-situ measurements, by informing on the representativeness of the measurements for the model grid scales.

There are various absorption spectroscopic techniques available for open-path measurements. Laser systems offer the advantage of high brightness with good collimation of the light beam, making them highly practical for measurements along long paths. Their downside is their low spectral coverage (at least for traditional lasers). Systems based on continuous wave lasers (e.g., Dobler et al., 2013; Lian et al., 2019) typically measure at a few discrete spectral points. Typically one point is located on a sufficiently strong spectral absorption line of a target gas and another one in a transparent region next to it. This does of course not provide any information on the shape of the absorption line and often leads to results which are correlated with environmental parameters like humidity, temperature, and pressure. Further, they are basically limited to measure a single species. The use of tunable diode lasers extends this technique to the measurement of a full absorption line or even a few spectrally close ones (e.g., Bailey et al., 2017). This can reduce the correlations to environmental factors. Laser frequency combs drastically improve on the spectral coverage and can span many hundreds of wavenumbers. This gives such setups access to full rotational-vibrational absorption bands and multiple species at very high resolutions, typically also removing their reliance on separate temperature, pressure, and humidity information. In the context of atmospheric remote sensing they are typically deployed in a dual-comb setup (e.g., Coddington et al., 2016; Truong et al., 2016; Olson et al., 2018; Waxman et al., 2019; Galtier et al., 2020; Giorgetta et al., 2021). However, these systems in their current state of development typically require labor intensive maintenance to keep them running stably. A technique which provides even larger spectral coverage is Fourier-transform infrared spectroscopy (FTIR). With the use of thermal light sources, such spectrometers can measure spectra spanning several thousand wavenumbers, providing simultaneous access to a plethora of species and their respective spectral features. FTIR open-path systems working in the mid infrared (MIR) are well established (e.g., Wiacek et al., 2018; Bai et al., 2020; You et al., 2021). These MIR systems are typically limited to absorption path lengths of a few hundred meters, due to the low brightness of the available light sources and the interference with the thermal emissions of the measured gases themselves. Shifting the spectral range to the near infrared (NIR)

allows the use of hotter thermal light sources like halogen lamps, enabling such systems to achieve path lengths exceeding kilometers.

Griffith et al. (2018) pioneered such FTIR open-path measurements of GHGs in the NIR in a demonstration study at the Institute of Environmental Physics (IUP) in the city of Heidelberg, Germany. They based their system on an IRCube, a compact and robust FTIR spectrometer manufactured by Bruker Optics. Since then they improved the setup in portability and light throughput, optimizing it for field deployments (Deutscher et al., 2021). The FTIR open-path system at the heart of this work focuses on a different, complementary set of features:

1. Providing long term records of path averaged GHG concentrations above Heidelberg.
2. Providing flexibility for methodological exploration and for testing the parameter space of open-path measurement design.

To achieve this, our atmospheric observatory utilizes a Bruker Optics IFS 125HR, a high resolution research spectrometer with a modular and spacious layout, configurable spectral resolution, and the possibility to easily switch between various detectors.

Within the work presented in this thesis, I developed and set up this open-path observatory, which includes the open-path optics, custom detector electronics for low light FTIR spectroscopy, and the system integration with the spectrometer itself. Further, I developed and implemented software and routines to operate and characterize the instrument and to retrieve information on GHGs from the measured spectra. Subsequently, I used the first eight months of measurements to characterize the systems performance and potential. In the following, I first describe the necessary fundamentals of absorption spectroscopy in Chapter 2. In Chapter 3, I give a comprehensive overview of the operating principle of a FTIR instrument. In Chapter 4, I lay out the details of the open-path setup and its design, and of the retrieval which extracts information from the spectra. I further describe the methods I use to further process and analyze the resulting data on GHGs. In Chapter 5, I present the results from the first eight months of the ongoing deployment. They include an analysis of different instrument and measurement configurations (choice of detector, spectral resolution, temporal resolution) and of different ways to evaluate the data. The chapter concludes with an analysis of the full time series of CO₂ and CH₄ measurements, where I show that the system detects different patterns than the local in-situ sensor showcasing that representativeness is a key issue under heterogeneous emission landscapes

and challenging meteorological conditions. The thesis concludes with Chapter 6, where I give a final summary and analysis of my findings, as well as an outlook on further research opportunities with the now operational permanent open-path GHG observatory.

2 Molecular Spectra in the Atmosphere

Remote sensing of gases relies on measurements of spectra and the subsequent identification and quantification of gas amounts using their spectroscopic signatures. Thorough knowledge of these signature is necessary for accurate results. To predict and understand them requires quantum mechanical calculations. While highly accurate laboratory measurements still yield better results than pure *ab-initio* calculations, they are important to fill gaps, attribute spectral residuals, and identify physical and efficient ways to parameterize these spectroscopic signatures (Hartmann et al., 2018; Fleurbaey et al., 2021; Birk et al., 2021; Malarich et al., 2023; Rothman et al., 1987, 2005, 2013). Hence, this chapter deals with the physical origins of molecular spectra in the atmosphere, how we can parameterize the spectroscopic signatures of gases, and how we can use them to quantify gas amounts with remote sensing. First, we take a look at the quantum mechanical origin of isolated spectral lines and derive some other useful results along the way. Second, we discuss vibration-rotation spectra of molecules. This continues with a discussion of line broadening and the profile of absorption lines, followed by a brief overview of two collisional effects in the form of line mixing and collision induced absorption (CIA). The chapter concludes with the fundamentals of absorption spectroscopy in the atmosphere and how we can calculate gas amounts from measured spectra. The first two sections are mostly based on Bransden et al. (2003). The following sections on line profiles and collisional effects follow Hartmann et al. (2021), who provide an extensive and fundamental discussion of collisional effects on the spectra of molecules. In general Bransden et al. (2003), Bernath (2005), and Hartmann et al. (2021) provide a solid quantum mechanical treatment of the matter, but may not be the best choice to build a first basic understanding. Petty (2006) and also to some extent Griffiths and De Haseth (2007) provide a more intuitive, although slightly more superficial approach. Herzberg (1989, 1991) provides an extensive overview of the transition bands for many molecules, how they result from the symmetry of their structure,

and on the numbering of vibrational bands, which is relevant to understand most notations of specific transition lines.

2.1 The Origin of Discrete Spectral Lines

The Schrödinger equation describes the time evolution of the wave function $|\Psi\rangle$ of a (non relativistic) quantum mechanical system, where the Hamiltonian \mathbf{H} is the quantum mechanical operator which corresponds to the energy of the system:

$$i\hbar \frac{\partial}{\partial t} |\Psi\rangle = \mathbf{H} |\Psi\rangle, \quad (2.1)$$

with the imaginary unit i and the reduced Planck constant \hbar . If a Hamiltonian is explicitly time independent, we denote it as \mathbf{H}_0 . The eigenstates $|\psi_k\rangle$ of \mathbf{H}_0 have a defined energy E_k ,

$$\mathbf{H}_0 |\psi_k\rangle = E_k |\psi_k\rangle, \quad (2.2)$$

and form a complete basis in which $|\Psi\rangle$ can be expressed. This equation is usually called the time independent Schrödinger equation. There are two direct corollaries to this: First, these eigenstates have a trivial time evolution (given by a phase term) and are thus stationary states. Second, they have a well defined energy. In the end, the latter results in discrete spectra if the stationary states of a system are coupled via electromagnetic (EM) radiation: To satisfy energy conservation, the transition from one eigenstate to another has to absorb/release the energy difference between the two states in form of a photon.

In the following, I provide a more detailed argument by outlining the typical quantum mechanical calculations which give rise to discrete lines. This enables us to acknowledge the central simplifications and also to later understand why the discrete spectra are not infinitely sharp in practice. The Hamiltonian of a particle with mass m in a potential V is

$$\mathbf{H}_0 = \frac{1}{2m} (-i\hbar \nabla)^2 + V, \quad (2.3)$$

where the first term describes the kinetic energy of the particle. For a (spinless) particle of charge q in an EM field (described by the vector potential \mathbf{A}) the Hamiltonian is

$$\mathbf{H} = \frac{1}{2m} (-i\hbar \nabla - q\mathbf{A})^2 + V. \quad (2.4)$$

For simplicity (and since this is not an essay on theoretical quantum mechanics)

we already adopted the Coulomb gauge ($\nabla \cdot \mathbf{A} = 0$) and do not further discuss the gauge invariance. We can now separate this Hamiltonian in an unperturbed part without the EM field (\mathbf{H}_0 , Equation 2.3) and a part which describes the interaction of the particle with the EM field (\mathbf{H}_{int}):

$$\mathbf{H} = \mathbf{H}_0 + \mathbf{H}_{\text{int}}, \quad (2.5)$$

with

$$\mathbf{H}_{\text{int}} = -\frac{i\hbar q}{m} \mathbf{A} \cdot \nabla + \frac{q^2}{2m} \mathbf{A}^2. \quad (2.6)$$

If we now assume, that the interaction is comparatively small, we can use perturbation theory to analyze the reaction of the particle to the perturbation of \mathbf{H}_0 . For this we assume the system in an initial state $|\psi_i\rangle$ and that the perturbation starts at $t = 0$. We also assume incoherent radiation and drop interference terms. The probability to find the system in the final state $|\psi_f\rangle$ is then

$$p_f(t) \propto \left| \int_0^t \langle \psi_f | \mathbf{H}_{\text{int}} | \psi_i \rangle \exp(i\omega_{fi}t') dt' \right|^2, \quad \text{with } \hbar\omega_{fi} = E_f - E_i. \quad (2.7)$$

Two more assumptions now give rise to discrete absorption lines: First we make the so called weak field approximation and drop the \mathbf{A}^2 term in \mathbf{H}_{int} . Then we assume a plane wave with wave vector \mathbf{k} , linear polarization $\boldsymbol{\varepsilon}$ and angular frequency ω . The vector potential at time t and point \mathbf{x} is then

$$\mathbf{A} = \boldsymbol{\varepsilon} A_0 \cos(\mathbf{k} \cdot \mathbf{x} - \omega t + \delta). \quad (2.8)$$

It is easy to extend this to a superposition of plane waves by integrating over ω and having A_0 and δ be functions of ω , but I keep the following discussion limited to a single plain wave for simplicity and also set the phase δ to zero. The probability for $|\psi_f\rangle$ now reads

$$p_f(t) \propto \left| A_0 \int_0^t M_{fi} \exp(i(\omega_{fi} - \omega)t') dt' \right|^2, \quad (2.9)$$

where M_{fi} is the matrix element

$$M_{fi} = \langle \psi_f | \exp(i\mathbf{k} \cdot \mathbf{x}) \boldsymbol{\varepsilon} \cdot \nabla | \psi_i \rangle, \quad \text{with } |\mathbf{k}| = c\omega. \quad (2.10)$$

Here, the term $\omega_{fi} - \omega$, meaning the difference between the angular frequencies of transition and the interacting radiation or also the detuning between the two,

appears for the first time. Since this detuning is in the exponent of an oscillatory term, the probability $p_f(t)$ is only non zero if $\omega_{fi} \approx \omega$. This is the origin of isolated lines, since the EM radiation can only cause a transition from an initial state $|\psi_i\rangle$ to a final state $|\psi_f\rangle$, if its frequency is tuned to the frequency matching the energy difference between the two states. We can further see, that the integral can be non zero even for a slightly detuned ω , but only for a finite time t . This property gives rise to the Lorentzian line shape of pressure broadening discussed in Subsection 2.3.2 (and also to the natural line width, which is not relevant in the context of this thesis).

We get further insights on the strength of the transition, if we now tune our electric field exactly to the transition frequency. The probability $p_f(t)$ then reduces to

$$p_f(t) \propto A_0^2 |M_{fi}(\omega_{fi})|^2 t, \quad (2.11)$$

which means that the system has a transition rate of

$$\frac{d}{dt} p_f(t) \propto A_0^2 |M_{fi}(\omega_{fi})|^2. \quad (2.12)$$

We see that the rate at which our system changes into a new final state depends on two factors: First the intensity of the EM field A_0^2 , and further on the strength of the transition itself. The strength of the transition is calculated as $|M_{fi}(\omega_{fi})|^2$, with the matrix element $M_{fi}(\omega_{fi})$. The dependency on the EM field intensity implies, that double the amount of radiation causes double the amount of transitions. As a result, the absorption rate of EM radiation is proportional to the amount of EM radiation and the strength of the transition at this frequency. This is essentially the well known Beer-Lambert law (Equation 2.30), which forms the basis for all radiative transport in this thesis and which I discuss further in Section 2.6. The second result is, that we need to calculate $M_{fi}(\omega_{fi})$ in order to get access to the strength of the transition. This calculation of the effect of the interaction on the initial state and the resulting overlap with the final state is at the core of all *ab-initio* calculations of transition probabilities and absorption cross-sections.

To get some insight on what governs this strength of the transition, we now make a final approximation in this quantum mechanical description of the interaction between EM fields and charged particles: $\mathbf{k} \cdot \mathbf{x}$ is small, due to the very small extend of atoms and molecules, and since we deal with visible or infrared

radiation. Hence, we can expand $\exp(\mathbf{ik} \cdot \mathbf{x})$:

$$\exp(\mathbf{ik} \cdot \mathbf{x}) = 1 + (\mathbf{ik} \cdot \mathbf{x}) + \frac{1}{2!}(\mathbf{ik} \cdot \mathbf{x})^2 + \dots \quad (2.13)$$

For many applications it is sufficient to only keep the first term and approximate $\exp(\mathbf{ik} \cdot \mathbf{x})$ with unity. This is the so-called dipole approximation, because after introducing the dipole operator $\mathbf{D} = -e\mathbf{x}$ (where e is the elementary charge) and some calculations (e.g. Bransden et al., 2003, p. 195f) the matrix element takes the form

$$M_{fi} = \frac{m\omega_{fi}}{\hbar e} \boldsymbol{\varepsilon} \cdot \mathbf{D}_{fi}, \quad (2.14)$$

with $\mathbf{D}_{fi} = \langle \psi_f | \mathbf{D} | \psi_i \rangle$. The matrix element of the transition is now proportional to the projection of the matrix element of the dipole operator on the plane of polarization. We call transitions, where this term dominates the matrix element, electric dipole transitions. The other terms in Equation 2.13 are typically only important in two cases: First, if a high level of accuracy is required, the subsequent terms can sometimes not be neglected, and second, if \mathbf{D}_{fi} is zero. In the latter case we call the transition electric dipole forbidden and the subsequent terms are now the dominant contribution to M_{fi} . For example the term $\mathbf{ik} \cdot \mathbf{x}$ in Equation 2.13 gives then rise to magnetic dipole and electric quadrupole transitions.

2.2 Description of Molecules and Vibration-Rotation Spectra

Up to now, the discussion concerned a charged particle in a potential and within an external EM field. The most instructive case for this is a charged particle within the potential of a harmonic oscillator or an electron in an attractive central potential, so basically the hydrogen atom. But the results also apply to more complex cases like molecules (which we are interested in), as I outline in the following.

Typically, the quantum mechanical treatment of molecules revolves around the Born-Oppenheimer approximation: Since electrons are more than three orders of magnitude lighter than the nuclei of atoms, their motion is near instantaneous in comparison to the nuclei. As a result, we can neglect the motion of the nuclei in a first step and just calculate the eigenstates and energies of the electrons, with the position of the nuclei as a parameter. This gives rise to an effective potential, in which the nuclei move, and which depends on the electronic state of the molecule. If we now assume a diatomic molecule like O_2 , we can describe the

relative position of the nuclei with a single vector \mathbf{R} (separating and ignoring the center of mass movement). In this case, our description is again equivalent to a single particle in a potential and all our results apply. For molecules of three or more nuclei this becomes more complex and typically involves the decomposition of the problem in eigenmodes of the nuclei's movement and treating them separately. Hence, I limit the following discussion mostly to a diatomic molecule. At the end of the section, I give a short overview of the transition bands most relevant in this thesis and on the underlying transitions.

2.2.1 Molecular Vibration

For a two atomic molecule in an electronic ground state, the Morse potential (Morse, 1929) is a good description of the effective potential in which the nuclei move. Figure 2.1 shows the Morse potential and the energies of the first 11 eigenstates for radial motion within this potential. It is common to perform a harmonic approximation to the Morse potential for fundamental discussions. The figure shows that this approximation gives a good estimate of the ground state energy, and is still quite accurate for the energy of the first excited state. For larger excitations the approximation gets steadily worse, but it provides a good starting point to interpret the excited states within the potential: In states with higher energy, the molecule's wave function can extend over a wider part of the potential, but is still centered around the equilibrium distance. This is similar to the classical concept of oscillation around an equilibrium position. Hence, we refer to these energy levels as molecular vibrations and label the level of excitation with the vibrational quantum number ν , starting at $\nu = 0$ for the ground state. This is the same for the Morse potential, except that the mean nucleus separation depends on the level of excitation.

The harmonic approximation also grants some insight into the allowed transitions between vibrational levels. As mentioned earlier, in the dipole approximation the matrix element takes the form of Equation 2.14 and is only non zero if $\mathbf{D}_{fi} = \langle \psi_f | \mathbf{D} | \psi_i \rangle$ is not zero. In case of the harmonic oscillator, \mathbf{D}_{fi} is non zero when the difference in vibrational excitation between the initial and final level is $\Delta\nu = \pm 1$ and vanishes for all other cases¹. Many textbooks thus formulate a selection rule of $\Delta\nu = \pm 1$ for vibrational transitions of molecules. But since this is a result from the harmonic approximation, which is inadequate for higher

¹This results from the expression of the position operator in terms of ladder operators and can be found in most books providing an introduction to quantum mechanics and the harmonic oscillator.

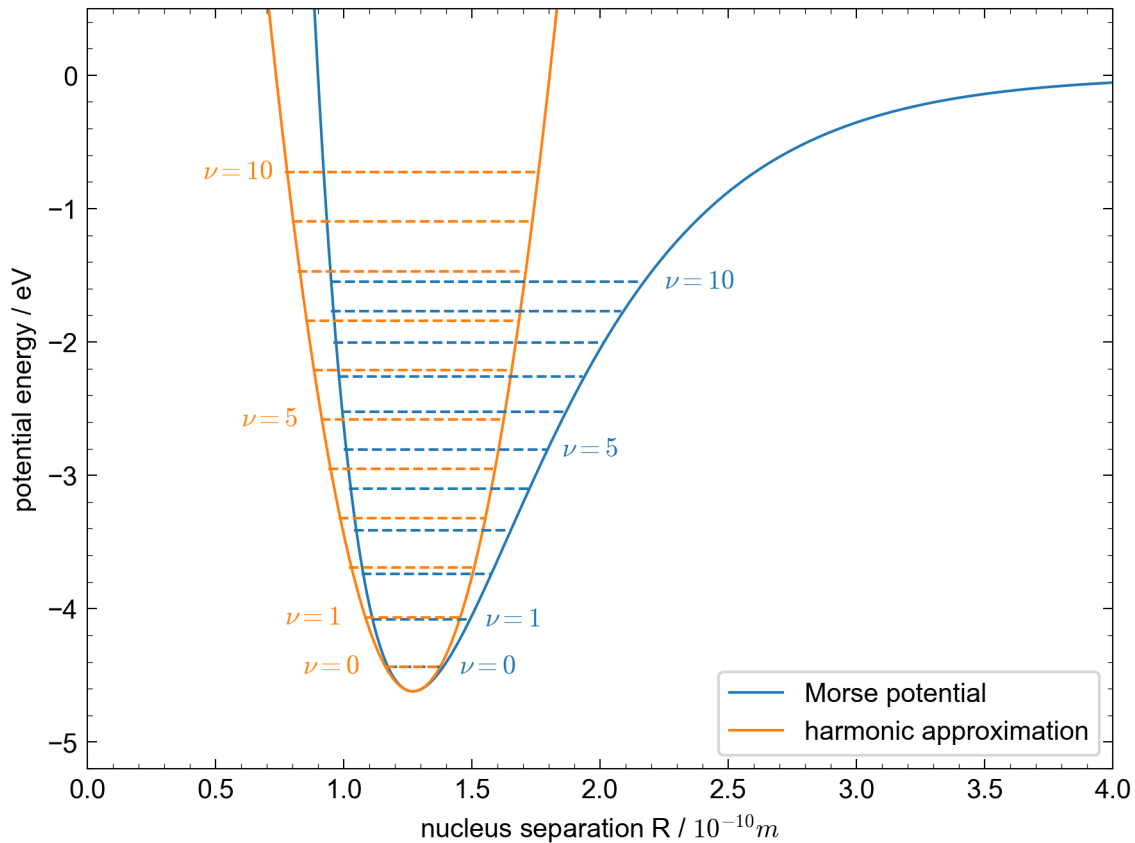


Figure 2.1: Morse potential for a diatomic molecule (in this example HCl) and its harmonic approximation. The dashed lines give the first 11 energy levels for the vibrational quantum number $\nu = 0$ to 10 for both potentials respectively. Molecule specific parameters are taken from Bransden et al. (2003). Formulas for the calculation of the eigen energies can also be found there.

vibrational excitations, this is not true in practice. As a matter of fact, all major transitions relevant within this work do not comply with this selection rule. Transitions of higher $\Delta\nu$ are possible due to the, in some cases small, anharmonicity of the Morse potential. But since they are a product of only the anharmonic terms, they are less likely/weaker than transitions which satisfy $\Delta\nu = \pm 1$ and are also allowed for a harmonic oscillator. As a final remark, we acknowledge, that the energy spacing between vibrational levels is on the order of 100 meV, which is equivalent to a photon of wavenumber 1000 cm^{-1} or wavelength of $10 \mu\text{m}$.

2.2.2 Molecular Rotation

Up to now, we covered the radial motion of the molecule's nuclei in a potential, but ignored the rotational motion. It is common, within the quantum mechanical

treatment of a diatomic molecule in the Born Oppenheimer approximation, to separate the angular momentum of the nuclei from the rest of the Hamiltonian and obtain the following Hamiltonian for the rotational energy:

$$\mathbf{H}_{\text{rot}} = \frac{\hbar^2}{2\mu} \frac{J(J+1)}{R^2}, \quad (2.15)$$

where J is the rotational quantum number, corresponding to the total angular momentum of the molecule, R is the nucleus separation, and $\mu = (M_A M_B)/(M_A + M_B)$ is the reduced mass of the two nuclei of masses M_A and M_B . Like for vibration, we can address this part of the nuclei's motion in an approximated form first, to draw conclusions on the basic structure and then acknowledge the shortcomings of this approximation and estimate how the un-approximated reality differs.

First, in the rigid rotator approximation, we can assume the internuclear distance to be constant at an equilibrium position R_0 . Equation 2.15 then simplifies to a scalar and the resulting energies are given by

$$E_J = \frac{\hbar^2}{2\mu R^2} J(J+1) = \frac{\hbar^2}{2I_0} J(J+1), \quad (2.16)$$

where we redefine $I_0 = \mu R^2$ as the moment of inertia of the molecule in a classical analogy. Since a photon in the dipole approximation carries an angular momentum of $J = 1$, a transition between two rotational states must include a change in angular momentum of $\Delta J = \pm 1$ to satisfy the conservation of angular momentum. Thus a transition can only occur between neighboring states.

A transition between two rotational states with rotational quantum numbers J and $J + 1$ corresponds to an energy difference of

$$\Delta E = E_{J+1} - E_J = \frac{\hbar^2}{I_0} (J+1). \quad (2.17)$$

Thus, a transition corresponding to a change in the rotational quantum number of $\Delta J = +1$ gives rise to multiple lines at energies depending linearly on the quantum number J of the initial state and which are equidistantly spaced by a molecule specific rotational energy constant \hbar^2/I_0 . For our earlier example of HCl, $\hbar^2/I_0 \approx 5 \text{ meV}$, which is equivalent to a photon of wavenumber 40 cm^{-1} or wavelength of $250 \mu\text{m}$. We see, that the energy of rotational transitions is smaller than the energy of vibrational transitions by more than an order of magnitude.

A treatment of Equation 2.15 without the rigid rotator approximation yields

two correction terms to the energies E_J :

$$E_{J,\text{cor}} = -a \left(\nu + \frac{1}{2} \right) J(J+1) - bJ^2(J+1)^2, \quad (2.18)$$

where a and b are molecule specific constants². The first correction term describes the dependency of the rotational energy levels on the current vibrational state, since for larger vibrational excitations ν the effective nucleus separation increases for the Morse potential (Figure 2.1). The second correction term is more interesting, since it is not linear in $J(J+1)$ but quadratic. It can be interpreted as an increase of the nucleus separation with increasing J , so the result of a centrifugal force in a classical interpretation, correcting the rigid rotator assumption. Both correction terms account for a larger effective nuclear separation than our initial assumption. Since the rotational energy is proportional to R^{-2} , both corrections terms are negative.

Including these two correction terms yields a correction to the transition energies (Equation 2.17) of

$$\Delta E_{\text{cor}} = -2a \left(\nu + \frac{1}{2} \right) (J+1) - 4b(J+1)^2(J+1), \quad (2.19)$$

bringing the energy difference between the rotation states J and $J+1$ to

$$\Delta E = E_{J+1} - E_J = \left(\frac{\hbar^2}{I_0} - 2a \left(\nu + \frac{1}{2} \right) - 4b(J+1)^2 \right) (J+1). \quad (2.20)$$

We can see that the first correction term just contributes a correction of the energy spacing for the different transitions. The second term however distorts the equidistant spacing, since now the energy spacing is dependent on $(J+1)^2$, causing a deviation to lower energies for larger values of J .

2.2.3 Combined Vibration-Rotation Spectra

Vibrational and rotational transitions often occur simultaneously. As we saw, the energies of rotational transitions are much lower than those of vibrational transitions. They are even lower than the typical thermal energy $k_B T \approx 26$ meV at room temperature ($T \approx 300$ K), where k_B is the Boltzmann constant. Thus, in a large ensemble of gas molecules many rotational states can be excited and the molecules

²Their dependency on the microscopic parameters of the molecule can be found in Bransden et al. (2003, p. 521).

can also transition between rotational excitations via collisions with each other. The energies of vibrational transitions are typically substantially larger than 26 meV and most molecules are in the vibrational ground state. As a result, most vibrational transitions are transitions from the ground state $\nu = 0$ to some excited state.

In a diatomic molecule, and for many vibrational transitions in general, a vibrational transition must be accompanied by a rotational transition. This is again due to the angular momentum of a photon in dipole approximation and the conservation of total angular momentum. The accompanying rotation transition must still follow

$$\Delta J = \pm 1. \quad (2.21)$$

If the vibrational transition corresponds to an energy difference of ΔE_ν and the rotational transition to an energy difference of ΔE_J , the combined transition is of energy $\Delta E_\nu \pm \Delta E_J$. This results in two branches, one at slightly higher energies called R branch ($\Delta J = +1$) and one at slightly lower energies called P branch ($\Delta J = -1$), as can be seen in Figure 2.2. The dependency of ΔE_J on the initial rotational excitation J and the fact that the molecules can be in many different initial rotational excitations at typical temperatures causes a further substructure of these branches, which is similar to that of purely rotational transitions discussed before. The result is a spectrum like the one in Figure 2.3, composed of multiple (mostly) equidistant lines in each branch according to Equation 2.20.

Figure 2.2 also indicates the existence of a Q branch ($\Delta J = 0$) without any rotational transitions. This branch would be a cluster of lines exactly at the energy of the vibrational transition, since transitions would occur from all possible initial rotational states, giving it a high degree of degeneracy. This Q branch is allowed for cases, where the difference in angular momentum can be accounted for by other means. Examples are transitions which include an electronic transition with a change in angular momentum of the electrons, or combinations of vibrations which contain angular momentum of the nuclei, typically including a break of the molecule's symmetry. The latter are especially common for initial states which are not in the vibronic ground state³. The two examples most relevant to this thesis are the Q branches of O₂ at an approximate wavenumber of 7880 cm⁻¹ and of CH₄ at 6000 cm⁻¹. The first one is a combination of vibrational rotational transitions with an electronic one, while the latter case is a symmetry changing transition, where the angular momentum is taken up in other form by the nuclei.

³Those are often called hot bands, due to the high temperatures needed to have a sufficient number of molecules in this initial state.

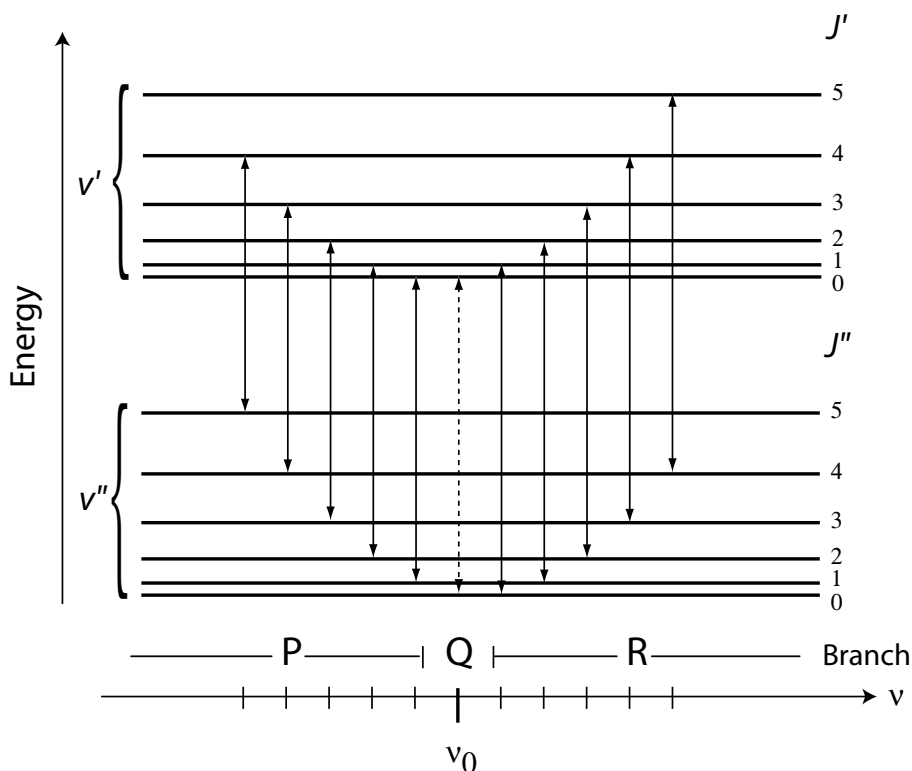


Figure 2.2: Schematic of the energy structure behind combined vibrational rotational transition with $\Delta J = \pm 1$ and for a vibronic transition energy corresponding to the wavenumber ν_0 . All transition for $\Delta J = +1$ form the R branch at higher energies/wavenumbers, while the transition for $\Delta J = -1$ form the P branch at lower energies/wavenumbers. If $\Delta J = 0$ is not forbidden, all corresponding transitions form a highly degenerated Q branch at ν_0 , independently of their initial J . The line spacing within each branch is equidistant, since the energies were calculated within the rigid rotator approximation. Figure taken with kind permission from Petty (2006).

For a final remark on bands of vibration-rotation transitions we look again at Figure 2.3 and note that all absorption lines are of different depth. While the exact calculation of line depth is a complicated matter, we can observe a general trend: Lines at around $J = 10$ are strongest in both branches, while the lines closer to the center (lower J) and further out (higher J) continuously decrease in strength. This is largely an effect of the population of the corresponding initial states. It is rather obvious, that radiation corresponding to a line, whose initial state is not present in a population of molecules, can not interact with anything and does not appear in a spectrum. For higher temperatures, the average amount of energy stored in the rotational degree of freedom increases, increasing the population of states with higher J and shifting the intensity of the spectral band away from the

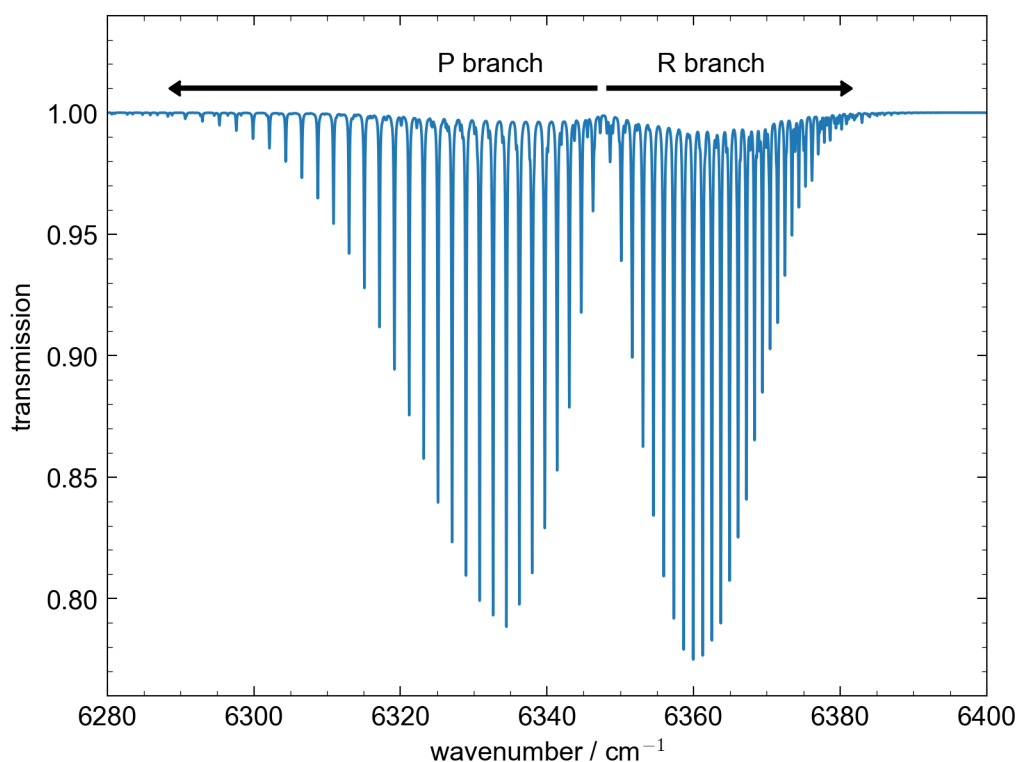


Figure 2.3: Exemplary transmission spectrum for a vibrational rotational transition comprised of a P and R branch. The decreasing spacing of the rotational lines with higher wavenumbers/energies due to the centrifugal corrections is clearly visible.

center and further out.

2.2.4 Relevant Transition Bands

The following overview over some relevant transition bands is based on Herzberg (1989, 1991). It is designed to provide some basic understanding of the underlying transitions and the resulting structure of the bands. The explanations I provide are by no means extensive and a detailed discussion would typically require group theory and a discussion of symmetries and point groups. Thus, for any further explanations, I would like to direct the curious reader to the above mentioned books by Gerhard Herzberg as a starting point. Since the here presented conventions might be in wide use, but are not necessarily universal, I still refer to the transition bands by their rough wavelength in the spectrum in the rest of this thesis.

CO₂ General Notation

The numbering scheme for the quantum states of CO₂ follows the convention $\nu_1\nu_2l\nu_3n$, where the vibrational quantum number ν_1 refers to the symmetric stretch mode, ν_2 refers to the bending mode, and ν_3 refers to the asymmetric stretch mode. The quantum number l refers to the possible rotational excitation that is possible once the vibrational bending mode ν_2 is excited and breaks the symmetry of the molecule. The number n is a practical addition to the convention since in the case of the linear CO₂ molecule, the two vibrational modes ν_1 and ν_2 have fundamental energies which form so-called Fermi resonances. The fundamental modes correspond to 1337 cm^{-1} and 667 cm^{-1} for ν_1 and ν_2 , respectively. Thus, for example the energy levels corresponding to $\nu_1 = 1$ and $\nu_2 = 2$ “collide”, their eigenstates mix and the result are new energy eigenstates which are a mix of both and can not be attributed to one of the vibrational states. The energies of these new energy eigenstates do not all correspond exactly to the combined energy of the excitations, but are rather “pushed” apart. Typically, the closer one of these energy eigenstate is to the initial resonance energy, the stronger the coupling to this band is. To indicate this, the vibrational states corresponding to such Fermi resonances are denoted by giving the maximum value for ν_1 and setting ν_2 to zero, but numerating all states corresponding to this resonance with the number n from high to low energy. Thus, for the above example of the $\nu_1 = 1$ and $\nu_2 = 2$ Fermi resonance, the resulting states are denoted as 10001 and 10002.

CO₂ 2 μ 2.0 μm Band

The underlying vibrational transitions for the 2.0 μm band of CO₂ are the 2001n-00001 transitions, where 2001n refers to the final state and 00001 to the initial state (in this case the ground state). The three vibrational bands in the 2.0 μm region are the transitions 20011-00001, 20012-00001, and 20013-00001. They all include a single excitation of the asymmetric stretching mode and a combined excitation of the symmetric stretching mode and bending mode, with an energy corresponding to a twofold excitation of the symmetric stretching mode. The 20012-00001 band is the strongest of the three, since the 20012 final state is closest to the resonance energy.

CO₂ 1.6 μm Band

The underlying vibrational transitions for the 1.6 μm band of CO₂ are the 3001n-00001 transitions, where 3001n refers again to the final state and 00001 is the initial

and ground state. Thus the transitions are quite similar to those of the 2.0 μm band, but contain a larger excitation of the resonant ν_1 and ν_2 modes. As a result, one more combination is possible and the resulting transitions are 30011-00001, 30012-00001, 30013-00001, and 30014-00001. The 30012-00001 and 30013-00001 band are the two strongest bands, since their respective final states are closest to the resonance energy.

CH₄ 1.65 μm Band

The underlying vibrational transitions for the 1.65 μm band of CH₄ are a two fold excitation of the ν_3 vibrational mode. This mode corresponds to a translation of the central carbon atom and a corresponding translation of all four hydrogen atoms in the opposite direction (similar to the asymmetric stretching mode for CO₂). The transition contains a Q branch, which is a result of the different symmetries the excited state can have and the possibility to take up angular momentum in the motion of nuclei.

O₂ 1.3 μm Band

This transition is an exception in the context of this thesis, since its origin is not a vibrational, but an electronic transition from the ground state $X^3\Sigma_g^-$ to the excited state $a^1\Delta_g$. Without diving deeper in the notation of these two states, we just note that because of this the transition band is sometimes referred to as O₂- Δ band. Due to the “gerade” symmetry of the states, the transition is electric dipole forbidden, but is an allowed magnetic dipole transition. Electric quadrupole components also provide a minor contribution to the transition (Gordon et al., 2010). Due to this, the transition is comparatively weak, but due to the high abundance of O₂ in the atmosphere the band is suitable for atmospheric remote sensing. A comparison with the 1.65 μm band of CH₄ provides a nice demonstration of that: even though the atmospheric concentration of methane is about five orders of magnitude lower than the concentration of O₂, both absorption bands are similar in strength. Since we did not really discuss electronic transition, Figure 2.4 provides a depiction of the transition at hand. The transition can be visualized as transition between the two vibrational ground states of two Morse potentials, each corresponding to one of the two electronic states. The transition band contains a Q branch, since the electronic transition can take up angular momentum.

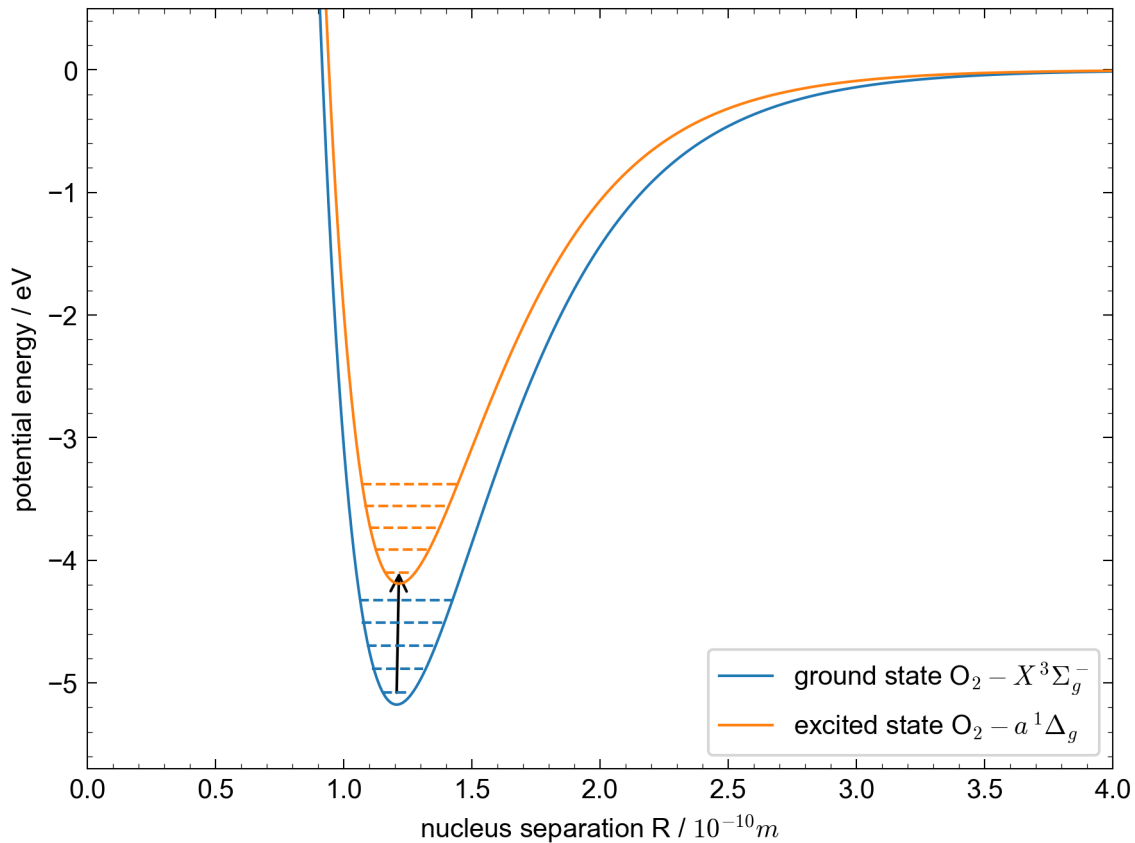


Figure 2.4: Morse potential for the ground state and first electronic excited state of O_2 . The dashed lines indicate the first vibrational. The black arrow indicates the transition corresponding to the O_2 - Δ band at approximately $1.3 \mu\text{m}$. Molecule specific parameters are taken from Herzberg (1989). Formulas for the calculation of the eigen energies can also be found there.

2.3 Profiles of Isolated Lines

Up to now, we concerned ourselves only with the spectral position of transition lines and to some extent with their strength. In the following, we take a look at the shape of individual lines, which effects influence it, and how we can parameterize it. First, we take a look at the shift caused by the relative motion of the molecules (Doppler broadening). Then, we analyze the effect of collisions between the molecules and how this results in pressure broadening. Further, we combine both effects in the Voigt profile. Finally, we briefly discuss some more advanced profiles like the speed-dependent Voigt (SDV) and Hartmann-Tran profiles.

2.3.1 Doppler Broadening

Molecules in a gas are constantly in motion and at speeds of several hundred m s^{-1} . Thus they are in a different inertial frame of reference than an observer who measures their absorption or emission spectrum and the spectra experience a Doppler shift. The doppler shift of an EM wave of wavenumber $\tilde{\nu}$ observed at a relative velocity of v is

$$\tilde{\nu}' = \tilde{\nu} \left(1 - \frac{v}{c}\right), \quad (2.22)$$

where c is the speed of light. The velocities of molecules in a gas mixture with an equilibrated temperature T is governed by the Maxwell-Boltzmann distribution and the velocity along an arbitrary axis x follows a Gaussian distribution:

$$p(v_x) = \frac{1}{v_T \sqrt{\pi}} \exp\left(-\frac{v_x^2}{v_T^2}\right), \quad (2.23)$$

where $p(v_x)$ is the probability for the velocity along x -axis v_x , and v_T is the most probable velocity. The most probable velocity is specific to the molecule's mass m and given by $v_T = \sqrt{2k_B T/m}$.

The result is a Gaussian broadening of the observed line according to

$$f_D(\tilde{\nu} - \tilde{\nu}_0) = \frac{\sqrt{\ln(2)}}{\alpha_D \sqrt{\pi}} \exp\left(-\frac{\ln(2)(\tilde{\nu} - \tilde{\nu}_0)^2}{\alpha_D^2}\right), \quad (2.24)$$

where $\tilde{\nu}_0$ is the center of the line and the half width at half maximum (HWHM) α_D is given by

$$\alpha_D = \tilde{\nu}_0 \sqrt{\frac{2 \ln(2) k_B T}{m c^2}}. \quad (2.25)$$

A quick estimation shows, that for a molecule like CO_2 the relative broadening at room temperature is approximately $\alpha_D/\tilde{\nu}_0 \approx 1 \times 10^{-6}$.

2.3.2 Pressure Broadening

Molecules in a gas constantly undergo collisions and exchange energy. These collisions can change the quantum mechanical state of the molecule, for example by changing to a different rotational state. Hence, the collisions "interrupt" the interaction of the molecule with the EM radiation. We earlier deduced from Equation 2.9 that a transition line is only infinitely sharp, if the interaction time approaches infinity and otherwise also small perturbances can result in a finite result of the integral for the transition probability. Calculation of the transition

probability as a function of spectral detuning and for a characteristic life time of the molecule's state yields a Lorentzian shape for the line:

$$f_L(\tilde{\nu} - \tilde{\nu}_0) = \frac{\alpha_L / \pi}{(\tilde{\nu} - \tilde{\nu}_0)^2 + \alpha_L^2}, \quad (2.26)$$

where α_L is the HWHM. α_L is approximately linear in pressure and at room temperature and atmospheric pressure for typical transitions within this work $\alpha_L / \tilde{\nu}_0 \approx 1 \times 10^{-5}$. Thus pressure broadening is the dominant broadening effect for vibration-rotation spectra in the lower levels of the atmosphere.

Apart from the broadening of the transition lines, collisions of molecules also cause a minor distortion to the potential energy of the molecule. This results in a slight shift of energy which is also approximately proportional to pressure. Typically, this is a measured quantity for each line and parameterized as a linear shift of the line center with pressure.

2.3.3 The Voigt Profile

The Voigt profile allows to account for both pressure and Doppler broadening by convolving the two line profiles:

$$f_V(\tilde{\nu} - \tilde{\nu}_0) = f_L(\tilde{\nu} - \tilde{\nu}_0) * f_D(\tilde{\nu} - \tilde{\nu}_0). \quad (2.27)$$

This profile is in wide use, since it is well understood, covers the two most relevant effects of line broadening, and requires only a limited amount of information to calculate: For the calculation of the Doppler broadening the knowledge of molecular mass and temperature is sufficient. The pressure broadening is typically parameterized by a broadening coefficient linear in pressure and an exponent for the temperature dependency. Further, a parameter accounting for the pressure shift is needed. All of these are typically measured quantities, specific for each line. So a knowledge of three parameters is sufficient to calculate the Voigt profile for a transition line at a specific pressure and temperature.

2.3.4 Advanced Line Profiles

The Voigt profile can not adequately cover some more intricate effects of collisions between molecules. Maybe the most obvious example is the speed dependency of the pressure broadening and pressure shift, which was first discovered by Mattick et al. (1973). This speed dependency results in a sum of Lorentzian profiles with

different broadenings and shifts to describe the pressure effects. Importantly, this sum is not again a Lorentzian profile. There are multiple line profiles which try to include this effect by ad hoc modifications. One such example is the SDV profile, which includes a second parameter for the pressure shift and pressure broadening, respectively. By now, there are profile models which are based on a physical description of the underlying processes, enabling them to parameterize such effects more correctly. One example of such models is the Hartmann-Tran profile (HTP)(Ngo et al., 2013, 2014), which is today the recommended profile for high resolution spectroscopy (Tennyson et al., 2014). But the use of these profiles requires the measurement of the respective parameters and the publication in spectroscopic databases like HITRAN (Gordon et al., 2022), as well as the availability of software to perform the non trivial calculation for these profiles in an efficient way. Further, in many atmospheric remote sensing applications the accuracy of the Voigt profile might not be the limiting factor. Hence, the HTP is not widely used yet in this field of application, even though the availability of parameters improved within the recent years (Gordon et al., 2022).

2.4 Collisional Line Mixing

Collisional line mixing causes a change of the shape and strength of spectral lines which are in near proximity and correspond to molecular states which experience efficient collisional coupling. More precisely, it requires that a molecule has a high probability to transition between the two initial and the two final states due to collisions with other molecules. A perfect example are rotational substructures of spectral bands with narrow spacing⁴: Due to the low energies of rotational excitations way below the thermal energy $k_B T$, molecules regularly transition between rotational states. Let us consider a molecule in a state $|\nu, J\rangle$, described by a vibrational quantum number ν and a rotational quantum number J . Collisions allow for efficient transitions between states of different J : $|\nu, J\rangle \leftrightarrow |\nu, J'\rangle$. If we now consider a band of vibrational rotational transitions, for example from the ground state $\nu = 0$ to the excited state $\nu = 1$, the resulting spectrum is made up of branches as in Figure 2.3. Within a branch, neighboring lines differ in their rotational excitation by one, so the two initial states are $|0, J\rangle$ and $|0, J + 1\rangle$. Then, the corresponding final states (assuming a transition in the R branch, so $\Delta J = +1$) are $|1, J + 1\rangle$ and $|1, J + 2\rangle$. We denote transitions under the absorption of a photon with γ_J , with J being the rotational quantum number of

⁴Making this is of course especially relevant for Q branches.

the initial state. Thus, we now consider the two spectral lines which we identify with γ_J and γ_{J+1} , and write

$$\begin{aligned} |0, J\rangle &\xrightarrow{\gamma_J} |1, J + 1\rangle \\ |0, J + 1\rangle &\xrightarrow{\gamma_{J+1}} |1, J + 2\rangle. \end{aligned}$$

But the transition from $|0, J\rangle$ to $|0, J + 1\rangle$ can also include the following process:

$$|0, J\rangle \xrightarrow{\text{collision}} |0, J + 1\rangle \xrightarrow{\gamma_{J+1}} |1, J + 2\rangle \xrightarrow{\text{collision}} |1, J + 1\rangle,$$

where the molecule first changes its rotational state due to a collision, then undergoes a different vibrational rotational transition and then changes its rotational state again due to a collision. This means, that we can not consider the individual lines in isolation to calculate their shape and intensity, but have to account for mixing processes due to the collisions in a thermodynamically equilibrated gas mixture.

The exact effects of line mixing on the intensity and shape of lines is difficult to predict and typically involves costly computation. But in general line mixing transfers intensity from weaker lines to stronger ones. The following argument can motivate this behavior: Let ρ_J be the population of the state J and $p_{J \rightarrow J'}$ be the probability to transition from state J to J' via collision. Assuming thermodynamic equilibrium, the populations and transition probabilities must satisfy the detailed balance relation and the total number of transitions in each direction must be equal:

$$p_{J \rightarrow J'} \rho_J = p_{J' \rightarrow J} \rho_{J'}.$$

If now $\rho_J > \rho_{J'}$, this requires $p_{J \rightarrow J'} < p_{J' \rightarrow J}$. Thus, the coupling from the less populated state J' to the more populated state J is more efficient. In general, this leads to an intensity transfer of weaker absorption regions to stronger ones, amassing more intensity at the center of gravity of close transition lines.

2.5 Collision Induced Absorption

Up to now, we only considered the intrinsic coupling of molecular states to the EM field, for example due to their permanent dipole moment. This neglects effects like temporarily induced dipole moments due to collisions with other molecules. Since these induced dipoles give rise to absorption bands, the effect is called collision induced absorption (CIA). These CIA bands are typically broad

and can span hundreds of wavenumbers, and are thus sometimes indistinguishable from the continuum background in a spectroscopic measurement. But they can also show narrower substructures in the range of tens of wavenumbers. Parameterizations of these CIA bands is available for some molecules and spectral regions (Karman et al., 2019).

2.6 Absorption Spectroscopy

Now turning to a macroscopic scale, the intensity of light is typically quantified by a measure of power. The basic quantity to discuss the transport of this power in space is the spectral radiance

$$I_{\tilde{\nu}} = \frac{\partial^3 P}{\partial A \partial \Omega \partial \tilde{\nu}}, \quad (2.28)$$

which describes how this power is distributed over an Area A , solid angle Ω , and along the spectral dimension $\tilde{\nu}$. In general, the change of spectral radiance along a path s through the atmosphere is described by the radiative transfer equation (e.g. Petty, 2006):

$$\frac{\partial I_{\tilde{\nu}}}{\partial s} = -\beta_{a,\tilde{\nu}} I_{\tilde{\nu}} - \beta_{s,\tilde{\nu}} I_{\tilde{\nu}} + \beta_{a,\tilde{\nu}} B_{\tilde{\nu}} + \beta_{s,\tilde{\nu}} \int_{4\pi} P_{\tilde{\nu}}(\theta) I_{\tilde{\nu}}(\theta) \cos(\theta) d\Omega, \quad (2.29)$$

where $\beta_{a,\tilde{\nu}}$ and $\beta_{s,\tilde{\nu}}$ are the coefficients of absorption and scattering, $B_{\tilde{\nu}}$ is the thermal emission according to Planck's law, and $P_{\tilde{\nu}}(\theta)$ is the scattering phase function. The four additive terms on the right hand side of Equation 2.29 describe the absorption of radiation, the scattering of radiation out of the beam, thermal emission along the path, and finally the scattering of radiation into the beam.

For the application within this work, we can simplify this equation and neglect all terms but the absorption of radiation: Atmospheric scattering at molecules or particles is typically spectrally broad and much broader than the narrow absorption features of molecular vibration-rotation transitions which we are interested in. Hence, out of beam scattering blends in with our broad band description of the initial intensity $I_{\tilde{\nu},0}$ and does not interfere with our analysis of narrow spectral features. Further, the design of the instrument setup makes it insensitive to the two additive terms describing thermal emission and into beam scattering. Section 4.1 elaborates on the reasons for this. Also, thermal emission of the atmosphere does not play a major role in the regime of NIR radiation. This reduction of the radiative transfer equation purely due to the absorption term is typically

called the Beer-Lambert law. In the following, we derive an expression of this law, which is most practical for the contents of this thesis.

If we reduce the right hand side of Equation 2.29 solely to the absorption term, we can easily integrate the equation and find

$$I_{\tilde{\nu}} = I_{\tilde{\nu},0} \exp \left(- \int_0^s \beta_{a,\tilde{\nu}}(s') \, ds' \right), \quad (2.30)$$

where we account for the possibility that $\beta_{a,\tilde{\nu}}$ changes along the path. Since the molecular absorption depends linearly on the number of molecules and the molecule's spectroscopic signature, which we describe with the absorption cross-section $\sigma_{\tilde{\nu},i}$, we can split up the absorption coefficient:

$$\beta_{a,\tilde{\nu}}(s') = \sum_i \sigma_{\tilde{\nu},i}(s') n_i(s'), \quad (2.31)$$

where we sum over all molecules i with their respective absorption cross-sections $\sigma_{\tilde{\nu},i}$ and number densities n_i . The transmission from Equation 2.30 now reads

$$\frac{I_{\tilde{\nu}}}{I_{\tilde{\nu},0}} = \exp \left(- \int_0^s \sum_i (\sigma_{\tilde{\nu},i}(s') n_i(s')) \, ds' \right). \quad (2.32)$$

Under the assumption, that the absorption cross-sections are constant along the path (which is typically valid for constant temperature and pressure along the path), we can write

$$\frac{I_{\tilde{\nu}}}{I_{\tilde{\nu},0}} = I_{\tilde{\nu},0} \exp \left(- \sum_i \sigma_{\tilde{\nu},i} \int_0^s n_i(s') \, ds' \right). \quad (2.33)$$

We can now define the column density (CD) of a molecule CD_i as the integral over the number density along a path and finally arrive at

$$\frac{I_{\tilde{\nu}}}{I_{\tilde{\nu},0}} = \exp \left(- \sum_i \sigma_{\tilde{\nu},i} CD_i \right). \quad (2.34)$$

In this form, our transmission depends on the absorption cross-section and the total CD of each molecule. Either summing up their products for each molecule and calculating a total transmission from that or calculating a transmission for each molecule and multiplying them is possible. The implementation of this law to retrieve CD of gases from spectra is later described in Section 4.2.

3 Operating Principle of Fourier Transform Spectrometry

Fourier transform spectrometry relies in a broad definition on the coherence of a radiation source, which is then measured in a time- or spatial-domain. A Fourier transform (FT) of this measurement then yields a spectrum over temporal or spatial frequencies. This work focuses on a measurement principle commonly referred to as FTIR. FTIR as a measurement technique is not limited to the infrared, but can also be applied to the visible and ultra-violet spectral regions.

This chapter gives a description of FTIR spectrometry, focusing on the instrument type used within this thesis and rigorous mathematical descriptions which can be directly implemented in software. Griffiths and De Haseth (2007) explain in great depth all intricacies of FTIR Spectrometry, typically including illustrative and detailed examples and focusing more on a conceptual understanding. Within this thesis, I follow their notation where applicable, to allow for easy cross referencing.

3.1 Concept of a Fourier Transform Infrared (FTIR) Spectrometer

At the heart of any FTIR instrument is an interferometer. It fulfills the role of a selector for certain wavelengths. Unlike a typical wavelength selector built around a grating or prism, it does not select a narrow band around a central wavelength. The transmission is rather a mix of wavelengths as a function of the operational state of the interferometer. Most commonly, the implementation is similar to a Michelson interferometer as depicted in Figure 3.1.

Let us assume a given optical path difference (OPD) of δ between the two arms of the interferometer. A monochromatic source of light of wavelength λ_0 or wavenumber $\tilde{\nu}_0 = 1/\lambda_0$ and intensity $I(\tilde{\nu}_0)$ enters the interferometer. In this case, the beams in each arm pick up a phase of $\Delta\phi = 2\pi\tilde{\nu}_0\delta$. Adding two oscillations that differ only in the above phase shift and applying trigonometric

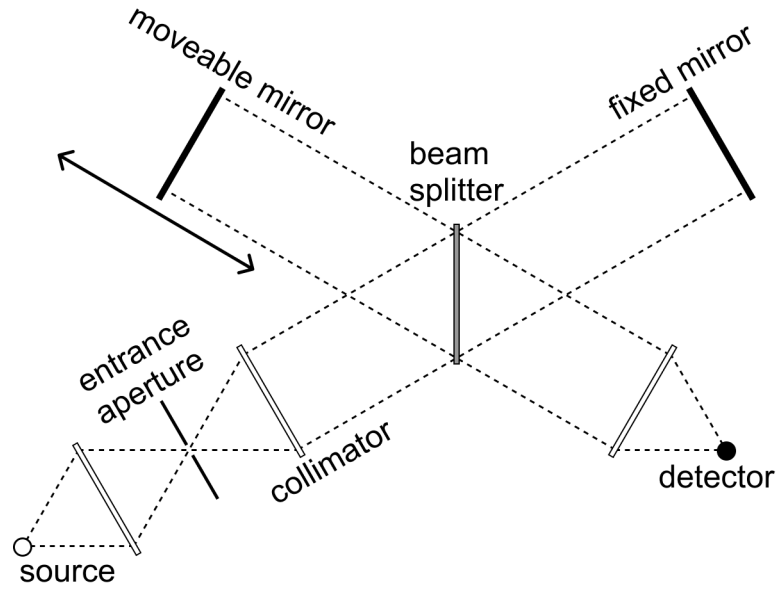


Figure 3.1: Schematic of a Fourier Transform Spectrometer. A thermal source emits radiation, which is focused on the entrance aperture of the instrument. The collimator passes a parallel light beam to the interferometer, where the beam splitter separates the light in the two arms of the interferometer. In both arms a mirror returns the light back to the beam splitter (BS), where it recombines and interferes. It is then focused on a detector, which measures the intensity of the radiation depending on the position of the moveable mirror.

identities yields the light intensity at the detector \hat{I} as a function of the OPD δ

$$\hat{I}(\delta) = 0.5 I(\tilde{\nu}_0) (1 + \cos(2\pi\tilde{\nu}_0\delta)). \quad (3.1)$$

This shows, that $\hat{I}(\delta)$ is constituted of a constant and a modulated component. In the context of FTIR they are called the dc and ac component respectively. The modulated ac component contains all of the spectral information and is generally referred to as the interferogram (IFG), denoted here as $I(\delta)$:

$$I(\delta) = 0.5 I(\tilde{\nu}_0) \cos(2\pi\tilde{\nu}_0\delta). \quad (3.2)$$

In all practical applications, there are additional factors that affect the magnitude of the measured signal: All optical elements (such as the beam splitter, mirrors, filters, etc.), the detector material and the amplifier introduce factors, which are typically also wavenumber dependent. We combine all of these factors in a single instrument specific parameter $G(\tilde{\nu})$. In a well controlled system, $G(\tilde{\nu})$ varies only slowly with wavenumber and does not change between mea-

measurements, resulting in two important corollaries: First, if accurate radiometric information is important, $G(\tilde{\nu})$ can be calibrated rather well, at least in the context of the difficulty that accurate radiometric measurements present. Second and most importantly, parts of $I(\tilde{\nu})$ which vary rapidly compared to $G(\tilde{\nu})$, can be easily separated from these instrument effects. Note, that molecular transitions typically belong in this category. We absorb all wavenumber dependencies in a single parameter $B(\tilde{\nu}) = 0.5 G(\tilde{\nu})I(\tilde{\nu})$, which gives the spectral intensity as measured by the instrument. Additionally, we denote the IFG measured by the instrument as $S(\delta)$. The equation for the IFG (Equation 3.2) now reads

$$S(\delta) = B(\tilde{\nu}_0) \cos(2\pi\tilde{\nu}_0\delta). \quad (3.3)$$

We extend our description from a monochromatic light source at wavenumber $\tilde{\nu}_0$ to a continuum source by integrating over all wavenumbers:

$$S(\delta) = \int_{-\infty}^{\infty} B(\tilde{\nu}) \cos(2\pi\tilde{\nu}\delta) d\tilde{\nu}. \quad (3.4)$$

This allows us to make two observations, first on the shape of the IFG and second concerning its relationship to $B(\tilde{\nu})$. Concerning the shape, we can see that at zero path difference (ZPD), meaning $\delta = 0$, all cosines are in phase and hence the integral is maximal. We call this the center burst of the IFG. For any wide and continuous spectrum $B(\tilde{\nu})$, the different cosine components are quickly out of phase. Hence, far out from the center burst, they only produce minor modulations. We can further see, that $S(\delta)$ is the cosine Fourier transform of $B(\tilde{\nu})$. Hence, we can formulate the back transformation

$$B(\tilde{\nu}) = \int_{-\infty}^{\infty} S(\delta) \cos(2\pi\tilde{\nu}\delta) d\delta. \quad (3.5)$$

This is the core equation of FTIR spectroscopy and means, that measuring the IFG $S(\delta)$ with an instrument and Fourier transforming it yields the spectrum $B(\tilde{\nu})$ of the observed source.

In practice there are still some limitations to this result: Obviously, we can not measure the IFG up to infinite OPD, which gives rise to a limited resolution of our resulting spectrum. Also, the capabilities of a real electro optical system in terms of light throughput and noise are limited, which results in an additional limit to resolution and a trade-off with signal to noise ratio (SNR). Finally, we can not sample the IFG on a continuous OPD grid, but have to make do with a specific sampling grid and perform a discrete Fourier transform on this data.

The rest of this chapter discusses such issues and how to resolve them and their corresponding trade-offs.

3.2 Resolution of a FTIR Spectrometer

An interferometer for a FTIR instrument will always be finite in size and hence only allow for finite OPD up to an instrument specific maximum optical path difference (OPD_{\max} , in equations denoted as Δ_{\max}). This modifies Equation 3.5 for the spectrum measured by a real instrument $B'(\tilde{\nu})$ in practice to

$$B'(\tilde{\nu}) = \int_{-\Delta_{\max}}^{\Delta_{\max}} S(\delta) \cos(2\pi\tilde{\nu}\delta) d\delta \quad (3.6)$$

$$= \int_{-\infty}^{\infty} D(\delta) S(\delta) \cos(2\pi\tilde{\nu}\delta) d\delta. \quad (3.7)$$

$D(\delta)$ is the so-called boxcar truncation function and defined as

$$D(\delta) = \begin{cases} 1 & \text{if } -\Delta_{\max} \leq \delta \leq \Delta_{\max} \\ 0 & \text{else} \end{cases}. \quad (3.8)$$

Since the FT of a product of functions is the convolution of the FT of each function, Equation 3.7 can be written as

$$B'(\tilde{\nu}) = f(\tilde{\nu}) * B(\tilde{\nu}), \text{ with } f(\tilde{\nu}) = \mathcal{F}[D(\delta)](\tilde{\nu}). \quad (3.9)$$

with $\mathcal{F}[D(\delta)](\tilde{\nu})$ denoting the FT of $D(\delta)$. We can see, that the measured spectrum $B'(\tilde{\nu})$ is a convolution of the true spectrum $B(\tilde{\nu})$ with $f(\tilde{\nu})$. Hence, the measured spectrum of an infinitely sharp monochromatic line of wavenumber $\tilde{\nu}_0$ is $f(\tilde{\nu} - \tilde{\nu}_0)$, which is why we call $f(\tilde{\nu})$ instrument line shape (ILS). The FT of the boxcar truncation function is given by

$$f(\tilde{\nu}) = 2\Delta_{\max} \frac{\sin(2\pi\tilde{\nu}\Delta_{\max})}{2\pi\tilde{\nu}\Delta_{\max}} \quad (3.10)$$

$$= 2\Delta_{\max} \text{sinc}(2\pi\tilde{\nu}\Delta_{\max}). \quad (3.11)$$

We can see that $f(\tilde{\nu})$ is centered around zero and has the shape of an (non-normalized) cardinal sine (sinc) function. The first intersections with the $\tilde{\nu}$ -axis are at $\tilde{\nu} = \pm 0.5 \Delta_{\max}$. Hence, the central peak of two lines separated by Δ_{\max} would be fully resolved at the base line. Accordingly, we define the *nominal reso-*

lution $\Delta\tilde{\nu}$ of our FTIR instrument as

$$\Delta\tilde{\nu} = \frac{1}{\Delta_{\max}}. \quad (3.12)$$

Hence, the nominal resolution of an FTIR instrument improves by the same factor as the maximal optical path difference of which the interferometer is capable of.

There are many other definitions for the resolution $\Delta\tilde{\nu}$, like the full width at half maximum (FWHM) of the ILS or a modification of the Rayleigh criterion for FTIR. All of these definitions only differ from Equation 3.12 by a constant factor, typically between 0.5 and 1. Thus, when comparing values for resolutions quoted by different sources it is important to consider the utilized resolution criterion. In practice, referring to OPD_{\max} of the interferometer instead of a resolution helps to avoid ambiguities. Within this thesis, all quoted resolutions use the definition of Equation 3.12, which is further emphasized by calling it *nominal resolution*. This is especially important to users of spectrometers made by the company Bruker Optics, since they use the definition $\Delta\tilde{\nu} = 0.9/\Delta_{\max}$ within their user interface.

It is important to note, that Equation 3.9 holds also if $D(\delta)$ is not the boxcar truncation function of Equation 3.8. $D(\delta)$ might be modified due to apodization (Subsection 3.6.1) or self-apodization (Section 3.3). In these cases, the ILS $f(\tilde{\nu})$ is still the FT of $D(\delta)$ and changes accordingly.

3.3 Optical Throughput and Self-Apodization

Up to now, we just considered rays of light which travel parallel to the optical axis within the interferometer. In a real instrument we depend on a finite light throughput, which necessitates that we collimate an extended (not infinitesimally small) light source. A typical implementation collimates the light of an illuminated spherical aperture with radius r , using a mirror of effective focal length f . This results in a maximal beam divergence of $\alpha_{\max} = \arctan(r/f)$ in the collimated beam, with α denoting the angle between the optical axis and the respective ray of light. Simple geometry shows, that a beam of light at an angle of α in an Michelson interferometer experiences only an OPD of $\delta \cos(\alpha)$, with δ still being the OPD of a ray of light along the optical axis (Griffiths and De Haseth, 2007, Section 2.6). Plugging this into Equation 3.4, we find for the IFG measured under a specific angle α

$$S(\delta, \alpha) = \int_{-\infty}^{\infty} B(\tilde{\nu}) \cos(2\pi\tilde{\nu}\delta \cos(\alpha)) d\tilde{\nu}. \quad (3.13)$$

We can now integrate over all solid angles which pass through our interferometer to calculate $\hat{S}(\delta)$, the IFG as measured by our Instrument:

$$\hat{S}(\delta) = \frac{1}{\Omega} \int_0^{2\pi} \int_0^{\alpha_{\max}} S(\delta, \alpha) \sin(\alpha) d\alpha d\phi \quad (3.14)$$

$$= \frac{2\pi}{\Omega} \int_0^{\alpha_{\max}} \int_{-\infty}^{\infty} B(\tilde{\nu}) \cos(2\pi\tilde{\nu}\delta \cos(\alpha)) d\tilde{\nu} \sin(\alpha) d\alpha \quad (3.15)$$

$$= \frac{2\pi}{\Omega} \int_{-\infty}^{\infty} B(\tilde{\nu}) \int_0^{\alpha_{\max}} \cos(2\pi\tilde{\nu}\delta \cos(\alpha)) \sin(\alpha) d\alpha d\tilde{\nu}, \quad (3.16)$$

where Ω denotes the total solid angle over which we integrate, and which is necessary for normalization. From here we can substitute $\beta = \tilde{\nu} \cos(\alpha)$, to again find a cosine FT:

$$\hat{S}(\delta) = \frac{2\pi}{\Omega} \int_{-\infty}^{\infty} B(\tilde{\nu}) \frac{1}{\tilde{\nu}} \int_{\tilde{\nu} \cos(\alpha_{\max})}^{\tilde{\nu}} \cos(2\pi\beta\delta) d\beta d\tilde{\nu}. \quad (3.17)$$

We use a generalized rectangular function to absorb the integration boundaries for the integration over β , which we define as

$$\text{rect}(x, a, b) = \begin{cases} 1 & \text{if } a \leq x \leq b \\ 0 & \text{else} \end{cases}. \quad (3.18)$$

We observe, that $\text{rect}(x - y, a - y, b - y)$ is always the same for all values of y , and for easier reading substitute $w = 1 - \cos(\alpha_{\max})$. This, together with Equation 3.18, leads to the final transformations

$$\hat{S}(\delta) = \frac{2\pi}{\Omega} \int_{-\infty}^{\infty} B(\tilde{\nu}) \frac{1}{\tilde{\nu}} \int_{-\infty}^{\infty} \text{rect}(\beta, \tilde{\nu} \cos(\alpha_{\max}), \tilde{\nu}) \cos(2\pi\beta\delta) d\beta d\tilde{\nu} \quad (3.19)$$

$$= \frac{2\pi w}{\Omega} \int_{-\infty}^{\infty} \cos(2\pi\beta\delta) \int_{-\infty}^{\infty} B(\tilde{\nu}) \frac{1}{\tilde{\nu} w} \text{rect}(\beta, \tilde{\nu} \cos(\alpha_{\max}), \tilde{\nu}) d\tilde{\nu} d\beta \quad (3.20)$$

$$= \frac{2\pi w}{\Omega} \int_{-\infty}^{\infty} \cos(2\pi\beta\delta) \int_{-\infty}^{\infty} B(\tilde{\nu}) \frac{1}{\tilde{\nu} w} \text{rect}(\beta - \tilde{\nu}, -\tilde{\nu} w, 0) d\tilde{\nu} d\beta. \quad (3.21)$$

We can now identify the Fourier transform of $\hat{S}(\delta)$:

$$\hat{B}(\tilde{\nu}) = \int_{-\infty}^{\infty} B(x) \frac{1}{xw} \text{rect}(\tilde{\nu} - x, -xw, 0) dx. \quad (3.22)$$

$\hat{B}(\tilde{\nu})$ is the spectrum as measured by a real instrument, that accepts light with a beam divergence of up to α_{\max} . We can see that $\hat{B}(\tilde{\nu})$ is a convolution of the true spectrum $B(x)$ with a spectral rectangle of variable width xw . This obviously limits the achievable resolution of our measured spectrum, depending on the

wavenumber and the maximum beam divergence. Equation 3.22 further shows, that the spectrum is shifted, since the spectral rectangle is not centered around zero. At each wavenumber, the spectrum is shifted by half the rectangle width towards lower wavenumbers. All of this becomes even more apparent if we calculate the measured spectrum for a spectral delta peak $B(\tilde{\nu}) = \delta(\tilde{\nu} - \tilde{\nu}_0)$ using Equation 3.22:

$$\hat{B}(\tilde{\nu}) = \frac{1}{\tilde{\nu}_0 w} \text{rect}(\tilde{\nu} - \tilde{\nu}_0, -\tilde{\nu}_0 w, 0) \quad (3.23)$$

$$= \frac{1}{\tilde{\nu}_0(1 - \cos(\alpha_{\max}))} \text{rect}(\tilde{\nu}, \tilde{\nu}_0 \cos(\alpha_{\max}), \tilde{\nu}_0). \quad (3.24)$$

We can see, that the delta peak at $\tilde{\nu}_0$ is transformed into a rectangle between $\tilde{\nu}_0 \cos(\alpha_{\max})$ and $\tilde{\nu}_0$.

In the previous section we defined a function, which convolved with the real spectrum yields the measured spectrum, the ILS. Equation 3.22 shows, that we have to deal with a wavenumber dependent ILS once we have diverging beams in the interferometer. Ideally, the contribution of the spectral rectangle is small compared to the ILS resulting from a finite IFG (Section 3.2). In these cases, it can be a valid simplification to set the width of the spectral rectangle constant within in certain wavenumber range, and calculate a constant ILS within this range. If we assume a constant width $\Delta = \tilde{\nu}_0 w = \tilde{\nu}_0(1 - \cos(\alpha_{\max}))$, the measured spectrum takes the form

$$\hat{B}(\tilde{\nu}) = \int_{-\infty}^{\infty} B(x) \frac{1}{\Delta} \text{rect}(\tilde{\nu} - x, -\Delta, 0) dx \quad (3.25)$$

$$= B(\tilde{\nu}) * \left(\frac{1}{\Delta} \text{rect}(\tilde{\nu}, -\Delta, 0) \right). \quad (3.26)$$

Since a folding operation is associative, we can just fold the rectangle into the ILS resulting from a finite IFG and handle it as one single ILS for this spectral domain. For computational reasons, which I discuss in Section 3.7, it is useful to transform this equation to IFG space. The dependency between ideal IFG $S(\delta)$ and the IFG including beam divergence $\hat{S}(\delta)$ is then

$$\hat{S}(\delta) = S(\delta) \mathcal{F} \left[\frac{1}{\Delta} \text{rect}(\tilde{\nu}, -\Delta, 0) \right] (\delta) \quad (3.27)$$

$$= S(\delta) \text{sinc}(\pi \Delta \delta). \quad (3.28)$$

Since this looks similar to apodization functions (discussed in Subsection 3.6.1), this effect of diverging beams within the interferometer is often called self-apodization.

As mentioned, it is desirable to keep self-apodization small. This is of course done by limiting the solid angle from which the instrument accepts light. But this means limiting the light throughput of the instrument and decreasing SNR of the measured spectra. So if light throughput and self-apodization are both issues, it is necessary to balance them against each other. To determine the acceptable limit for divergence of light in the interferometer, we can formulate the following condition: The largest angles should still contribute positively to the net modulation at maximum optical path difference for the largest frequency. This condition is violated, once the difference in OPD at maximum OPD for the center ray and the most angled rays increase beyond half a wavelength (corresponding to a phase difference of π) for the highest wavenumber $\tilde{\nu}_{\max}$. A brief calculation shows, that this is equivalent to limiting the width of the self-apodization rectangle to half the nominal resolution $\Delta\tilde{\nu}$:

$$\tilde{\nu}_{\max}(1 - \cos(\alpha_{\max})) = \frac{\Delta\tilde{\nu}}{2}. \quad (3.29)$$

If we now assume small angles for α_{\max} and use a Taylor expansion around zero, for the cosine, limit it to the first non constant term, and solve for α_{\max} we arrive at the popular equation

$$\alpha_{\max} = \sqrt{\frac{\Delta\tilde{\nu}}{\tilde{\nu}_{\max}}}, \quad (3.30)$$

or for the total solid angle Ω_{\max} , which is proportional to the light throughput, at

$$\Omega_{\max} = 2\pi\alpha_{\max}^2 = 2\pi\frac{\Delta\tilde{\nu}}{\tilde{\nu}_{\max}}. \quad (3.31)$$

3.4 Sampling the Interferogram

Since we would like to digitize the IFG for processing and evaluation, we need to sample it at discrete points. These points need to be equidistant (in OPD) to allow the usage of algorithms like the fast Fourier transform (FFT) and in general for easier data handling. In Section 3.2 we defined how large the covered OPD interval needs to be. This leaves the question, how far the sampling points should be spaced out. However, this is easily answered by the well known Nyquist-Shannon sampling theorem, which states that a signal must be sampled at twice the rate of its largest frequency. This allows for full reconstruction of the signal with no aliasing. Since wavenumbers are spatial frequencies, we can directly apply this and conclude, that the sampling rate must be at least twice that of the

largest wavenumber, where the spectrum is not zero. For a maximum wavenumber of $10\,000\text{ cm}^{-1}$ follows a minimal sampling frequency of $20\,000\text{ cm}^{-1}$, which means 2×10^6 sampling points per meter.

3.5 Technical Implementations

This section is about concrete technical implementations of a FTIR instrument as utilized within this work. Some of these details are only listed for the sake of completeness and do not significantly impact the operating principle of the instrument. This section does not cover aberrations within FTIR optics, detector non-linearities, so-called ghost lines and sampling errors, since these are today well under control by the manufacturers for NIR spectrometers like the one used in this thesis. If these topics are of interest, they are well described in Hase (1995) and Hase (2000).

3.5.1 Cube Corner Interferometers

Up to now, we only discussed a typical Michelson interferometer as depicted in Figure 3.1, which uses plane mirrors in the interferometer arms. This comes with major challenges when building and aligning an FTIR instrument: the tilt of both interferometer mirrors with respect to the optical axis and to each other. A different tilt of the mirrors with respect to each other causes a different tilt of the light exiting the interferometer for each interferometer arm, respectively. These different angles then result in a relative positional shift in the image plane on the detector for each interferometer arm. This shift needs to be significantly smaller than the diffraction limited image of a point source (Airy disk) at the detector, otherwise light originating from the same point would not interfere anymore. For reference, the Airy disk of an optic with a diameter $D = 7.5\text{ cm}$ at a wavenumber $\tilde{\nu} = 6600\text{ cm}^{-1}$ has an opening angle of $\theta \approx 1.22/(D\tilde{\nu}) \approx 2.5 \times 10^{-5}\text{ rad} \approx 5''$. The respective tilt of both interferometer mirrors to each other needs to be significantly smaller than that. Further, this must be true for the whole path of the movable mirror, a significant challenge, especially in high resolution applications with interferometer arms on the scale of meters.

A common technical solution to this problem is the use of cube corners instead of plane mirrors in the interferometer arms. A cube corner is formed by three reflective surfaces aligned orthogonally to each other. Such a system reflects an incoming beam of light back in the direction it came from (while also adding an

offset to the ray's position) and is sometimes called retro-reflector. This means, that tilt of the cube corners does not introduce tilt in the reflected beams of light, completely negating the effect described above. The FTIR spectrometer in this work uses aluminum cube corners in the interferometer arms.

3.5.2 Rapid-Scan Interferometers

As mentioned before, the IFG needs to be measured and digitized at discrete points, preferably equidistant in OPD. First of all, this means that the OPD range of interest must be scanned, meaning that the movable mirror is moved through the respective range. One way of implementing this scanning of the IFG is the so-called rapid-scan interferometer. In a rapid-scan interferometer, the movable mirror is kept at a constant velocity, typically between 0.1 cm s^{-1} and 10 cm s^{-1} . It scans through the whole used range of the interferometer. Once it reaches the end, the mirror can either be quickly returned to the starting position to start the next scan or it can scan the IFG in the other direction now starting from the endpoint. The later concept improves the duty cycle of the instrument, meaning that a larger fraction of the time is actually used to acquire data. This scanning in both directions is sometimes called forward-backward scan and is the typical mode of operation within this work.

To identify the equidistant points where we actually want to sample the IFG it is common to use a laser for reference. The idea is to pass the laser through the interferometer and use the resulting cosine IFG (assuming the laser is a perfectly sharp peak) as a measure for OPD. For example the zero crossings should occur at OPD of multiples of half the wavelength of the laser. The zero crossings can now be used to trigger an analog to digital converter (ADC) to record the signal of the actual spectrometer detector. This of course means, that the laser needs to be passed parallelly to the light path through the interferometer and detected separately.

Many precision spectrometers use a frequency stabilized HeNe laser for reference. At typical mirror speeds of rapid-scan interferometers, the HeNe laser signal oscillates at several kHz. This is an easily accessible way to monitor how constant the mirror velocity is. It is common to quote the mirror speed in terms of this oscillation of the reference laser, for example saying that an IFG was recorded at a speed of 5 kHz. With an approximate laser wavenumber of $15\,800 \text{ cm}^{-1}$, this would correspond to a physical mirror velocity of 0.16 cm s^{-1} or an optical velocity of 0.32 cm s^{-1} . This comes with the advantage, that it resolves the ambiguity of optical velocity and physical velocity of the mirror.

Using the separately detected reference laser signal to constrain the points where the IFG is sampled introduces a minor problem to the signal chain: The laser signal and the infrared signal are typically not in phase. Electronic filters and amplifiers within the circuitry add a phase error between the two signals, which then depends on the direction of mirror travel. Hence, the forward and backward scans of the IFG must be stored and processed separately and only the final spectra can be averaged. This process is described in more detail in Subsection 3.6.2.

In many modern instruments, such as the one used in this work, the reference laser signal is strictly speaking not really used to trigger an ADC to record the IFG, since these instruments use so-called *sigma-delta* ADCs. These ADCs were developed for audio signals and can not be triggered, but operate at a fixed frequency. This problem was solved by Brault (1996), who developed an adaptive digital filter, which basically interpolates the values of the IFG at spatially equidistant points.

3.5.3 Detectors and Detector Readout Electronics

The concept of FTIR is in principle applicable to all wavelength ranges, as long as there are mirrors and beam splitters (BSs) available to build an interferometer. In the final step, a detector needs to quantify the radiation and this detector element is often a limiting factor for the spectral bandwidth and performance. There are thermal detectors (for instance bolometers or thermistors), which detect radiation by the total power transmitted to them. They allow to access a broad spectral bandwidth, but usually do not allow for high scanning speeds due to their comparatively low response times (order of several milliseconds). Detectors, which rely on the photoelectric effect and the quantum nature of light, are more common today. Typical examples are mercury cadmium telluride (MCT) detectors for the MIR and indium gallium arsenide (InGaAs) detectors for the NIR. Within this work, I utilized two different InGaAs photodiodes. I now give an overview over the design principles of an FTIR detector based on photodiodes. For an in-depth discussion, please consult again Griffiths and De Haseth (2007) for anything FTIR specific or Hobbs (2009) for electro-optical design in general.

When designing a detector for an instrument with a rapid-scan interferometer, the spectral bandwidth of the detector needs to comfortably contain the alias frequency of our largest wavenumber of interest. So if our highest appearing wavenumber with the selected scanning speed has an alias frequency of 15 kHz, a factor of 2 is a good margin of safety. But it is also important to choose the

spectral bandwidth not too large. A spectral bandwidth beyond the Nyquist frequency of our ADC results in the noise (or worse, signal) beyond the Nyquist frequency appearing folded back below the Nyquist frequency. This results in an increase in noise, or even fake spectral features. Most ADCs probably come with their own filter to make sure of this, but limiting the spectral bandwidth below 100 kHz should safeguard against any of these problems when using typical rapid scan interferometers with *sigma-delta* ADCs, since their Nyquist frequencies are typically above that.

To achieve a meaningful resolution with an FTIR instrument, we are interested in the variations of the IFG far out from the center burst, where the variations are small compared to those around the center burst. To be able to resolve those, while not clipping the center burst, we need an ADC with a large dynamic range. A typical target is 24 bit. Thankfully, this is often provided within the interface to the FTIR instrument and in this thesis not part of the considerations. However, to make use of this dynamic range it is important to bring the output signal to the expected input level of the ADC without clipping it. The amplification and transformation of the photocurrent to an output voltage has to generate an appropriate signal level (typically 1 V to 10 V).

A front end, consisting of a transimpedance amplifier, typically performs all of these tasks (amplification, transformation, spectral bandwidth). To provide an ideal noise performance is the final, but important, requirement to the front end electronics. An intensive discussion of bandwidth and noise of photodiode front ends is given in Hobbs (2001). Here, we limit ourselves to the following typical noise sources for a photo diode with transimpedance amplifier:

1. Photocurrent shot noise, with a noise current spectral density of $i_{\text{SN}} = \sqrt{2ei_{\text{S}}}$, where e is the elementary charge, and i_{S} the signal current. If there is any current due to background signal, than this increases the noise analogously.
2. Johnson noise or thermal noise of a resistance R at temperature T , with a noise current spectral density of $i_{\text{TN}} = \sqrt{4k_{\text{B}}T/R}$ where k_{B} is the Boltzmann constant.
3. Voltage or current noise of the utilized operational amplifier. Choosing an appropriate amplifier typically reduces this noise source to an insignificant level. Hobbs (2001) again provides more details on this.

In an ideal case, the dominant noise source is the signal current shot noise. This noise source is fundamentally unavoidable, since it results from the Poissonian

statistics of the photon flux on the detector. If this noise source dominates and the SNR is insufficient, the only direct solution is an increase in the signal current. While this increases the noise by the square root, it also increases the signal linearly, resulting in a SNR, which increases with the square root. An important corollary to this is, that the total photocurrent contributes to the shot noise. This does include the photocurrent generated by background photons, as well as photons from spectral regions which are not of interest. So the shot noise can also be reduced by narrowing the optical bandwidth of the system, if this is possible without reducing the signal of interest.

To achieve a shot noise limited system, the other noise sources need to be significantly smaller. While we will not deal with amplifier noise here, since this can typically be handled by appropriate choice of parts, a discussion of thermal noise is necessary for the understanding of typical trade-offs when comparing detectors/photodiodes. In a transimpedance amplifier front end there are typically two relevant resistances which are sources of thermal noise: the feedback resistance and the shunt resistance of the diode itself. Since the magnitude of the feedback resistance is chosen so that the signal current i_s results in an output voltage on the order of at least 1 V, a brief calculation yields, that the shot noise is around 20 times larger than the thermal noise of the feedback resistor at 300 K. However, if the shunt resistance of the diode is significantly smaller than the feedback resistance, its thermal noise can start to dominate the shot noise. The shunt resistance of photodiodes typically decreases for materials which are sensitive to lower energy photons, due to their smaller band gap. The typical way to address this is by cooling the diode. This accomplishes two things: First, by reducing the temperature the thermal noise of the diode is reduced, and second it increases the resistance of the diode and again reduces the thermal noise. Since this increase in resistance is typically exponential, the latter contribution is far more important and even a few 10 K temperature reduction can significantly reduce the thermal noise. Standard InGaAs photodiodes, which are sensitive to wavelengths up to 1.8 μm , do typically not need cooling, except for very small signal currents or large area detectors. For extended InGaAs photodiodes, which can access longer wavelengths than standard InGaAs photodiodes, it is typically sufficient to use thermoelectric (TE) cooling to operate them at temperatures of -10°C to -30°C .

3.6 From Interferogram to Spectrum

This section describes the way from a properly measured and sampled IFG to a finished spectrum. There are three main components to the evaluation chain: The apodization, to purposefully change the ILS, the FT to convert the IFG into a spectrum (typically performed with an FFT), and finally the phase correction, a way to correct for phase errors in the recording of the IFG caused by hardware imperfections. Again, Griffiths and De Haseth (2007) is a great reference with illustrative explanations. The following subsections describe apodization and phase correction.

3.6.1 Apodization

In Section 3.2, we discussed that multiplying a truncation function $D(\delta)$ to an IFG is the same as folding the spectrum with its FT $f(\tilde{\nu}) = \mathcal{F}[D(\delta)](\tilde{\nu})$. A direct corollary of this observation is that $f(\tilde{\nu} - \tilde{\nu}_0)$ is the measured shape of an infinitely sharp spectral line at wavenumber $\tilde{\nu}_0$. Further, we introduced this truncation function due to the limitations of an instrument. For these two reasons, we call $f(\tilde{\nu})$ instrument line shape. To describe the finite size of an instrument, we initially used a boxcar truncation function for $D(\delta)$, which does nothing else than limiting the IFG to a maximum extend. In theory, the truncation function could have any shape, and still its FT would give the ILS. We can also perform such a modification artificially by multiplying a function to the ILS. We call such a function $A'(\delta)$ an apodization function. Equation 3.7 then modifies to

$$B'(\tilde{\nu}) = \int_{-\infty}^{\infty} A'(\delta)D(\delta)S(\delta) \cos(2\pi\tilde{\nu}\delta)d\delta. \quad (3.32)$$

The ILS is then the FT of $A(\delta) = A'(\delta)D(\delta)$:

$$f(\tilde{\nu}) = \mathcal{F}[A'(\delta)D(\delta)](\tilde{\nu}) = \mathcal{F}[A(\delta)](\tilde{\nu}). \quad (3.33)$$

Since it is common to define apodization functions in relation to a maximum OPD, we absorb the truncation aspect into it and call it $A(\delta)$.

There are many choices for apodization functions. Basically all of them have in common, that they roll off to lower values for high OPD, before eventually reaching the point of truncation (from where on they are zero). This causes a relative reduction of the information content at higher OPD compared to lower OPD and has to result in a reduction of resolution. But since the transition at the trunca-

tion point is less sharp, the FT (meaning the ILS) experiences less “ringing”. This is very often desirable, since it decreases the interference between close spectral lines. The resulting spectra might be easier to interpret for humans and algorithms alike. During the development of FTIR spectrometry, many apodization functions were tested, to find an optimum between the desired reduction in ringing and the accompanying reduction in resolution. A widely used set of functions are the so-called Norton-Beer apodization functions (Norton and Beer, 1976, take note of the errata published 1977). They offer a near optimal trade-off between ringing and resolution reduction and come in three different strengths of apodization, which offers the user to tailor the apodization to their needs. They are called Norton-Beer weak (NBW), Norton-Beer medium (NBM), and Norton-Beer strong (NBS). Within this work, I exclusively use the NBM apodization function.

3.6.2 Phase Correction

When recording IFGs, there are different sources of so-called phase errors, as mentioned before. The most typical cases are a frequency neutral phase error, when the sampling of the IFG does not perfectly align with the center burst, and a chromatic phase error, for example due to frequency dependent delays in the electronics of a rapid-scan interferometer. As a result, all or some frequencies are not completely in phase at the point we identify as ZPD. To describe the resulting interferogram, we can modify Equation 3.4 by introducing a phase function $\theta(\tilde{\nu})$:

$$S(\delta) = \int_{-\infty}^{\infty} B(\tilde{\nu}) \cos(2\pi\tilde{\nu}\delta - \theta(\tilde{\nu}))d\tilde{\nu}. \quad (3.34)$$

We can immediately see, that the relationship between measured IFG and spectrum is no longer given by the cosine FT. Instead, we need to correct for the effects of the phase function $\theta(\tilde{\nu})$. This process is called phase correction and there are multiple ways to do this, either in IFG-space or spectral space. In the following, I derive a way to correct for these phase effects after Fourier transforming the IFG to a spectrum.

Looking at Equation 3.34 and using the basic trigonometric identity $\cos(\alpha - \beta) = \cos(\alpha)\cos(\beta) + \sin(\alpha)\sin(\beta)$, we can infer that this introduces sine terms, where we just had a cosine FT before. As a result, we now have to deal with cosine and sine FTs, where we before only encountered cosine FTs. To differentiate, I denote the cosine FT of a function $g(\tilde{\nu})$ as $\mathcal{F}_c[g(\tilde{\nu})](\delta)$ and its sine FT as

$\mathcal{F}_s[g(\tilde{\nu})](\delta)$. They are defined as

$$\mathcal{F}_c[g(\tilde{\nu})](\delta) = \int_{-\infty}^{\infty} g(\tilde{\nu}) \cos(2\pi\tilde{\nu}\delta) d\tilde{\nu} \quad \text{and} \quad (3.35)$$

$$\mathcal{F}_s[g(\tilde{\nu})](\delta) = \int_{-\infty}^{\infty} g(\tilde{\nu}) \sin(2\pi\tilde{\nu}\delta) d\tilde{\nu}. \quad (3.36)$$

We can now transform Equation 3.34, by applying the above trigonometric identity:

$$S(\delta) = \mathcal{F}_c[B(\tilde{\nu}) \cos(\theta(\tilde{\nu}))](\delta) + \mathcal{F}_s[B(\tilde{\nu}) \sin(\theta(\tilde{\nu}))](\delta). \quad (3.37)$$

To evaluate this expression, we remind ourselves, that applying a sine or cosine FT twice yields the initial function, and that the sine FT of a cosine FT (or vice versa) is zero. This also follows via a brief calculation from the definitions (Equation 3.35 and Equation 3.36) and the orthogonality of sine and cosine functions. A calculation of both FTs results in

$$B_c(\tilde{\nu}) = \mathcal{F}_c[S(\delta)](\tilde{\nu}) = B(\tilde{\nu}) \cos(\theta(\tilde{\nu})) \quad \text{and} \quad (3.38)$$

$$B_s(\tilde{\nu}) = \mathcal{F}_s[S(\delta)](\tilde{\nu}) = B(\tilde{\nu}) \sin(\theta(\tilde{\nu})), \quad (3.39)$$

where $B_c(\tilde{\nu})$ denotes the cosine spectrum of the IFG and $B_s(\tilde{\nu})$ denotes its sine spectrum. Neither quantity gives us direct access to $B(\tilde{\nu})$, the quantity which we are interested in, but we need information on the phase function $\theta(\tilde{\nu})$. $B(\tilde{\nu})$, the spectrum without any phase effects, is still the quantity we are interested in. To get access to it, we need the phase function $\theta(\tilde{\nu})$, which we can calculate:

$$\frac{B_s(\tilde{\nu})}{B_c(\tilde{\nu})} = \tan(\theta(\tilde{\nu})) \quad (3.40)$$

$$\Rightarrow \theta(\tilde{\nu}) = \arctan\left(\frac{B_s(\tilde{\nu})}{B_c(\tilde{\nu})}\right). \quad (3.41)$$

This does not only give us the phase function $\theta(\tilde{\nu})$, but also shows us that we can interpret $B_c(\tilde{\nu})$ and $B_s(\tilde{\nu})$ as values along two orthogonal coordinates and $\theta(\tilde{\nu})$ the angle between the x-axis and the vector $(B_c(\tilde{\nu}), B_s(\tilde{\nu}))^T$. We could now restore the spectrum $B(\tilde{\nu})$ multiple ways, for example by taking the absolute value of this vector. But this (and other methods) come with the downside that they actually restore the absolute value of $B(\tilde{\nu})$. This becomes a relevant difference once we incorporate measurement noise in our spectrum. In areas where the spectrum is zero, it is desirable to have gaussian noise centered around zero. Taking the absolute of such a spectrum returns noise which no longer follows a normal distribution, but a χ^2 -distribution with one degree of freedom. We can solve this

problem if we assume that we have sufficient knowledge over $\theta(\tilde{\nu})$ by just rotating the vector $(B_c(\tilde{\nu}), B_s(\tilde{\nu}))^T$ by $-\theta(\tilde{\nu})$. The result is the vector $(B(\tilde{\nu}), 0)^T$, without taking the absolute value. Applying a standard rotation matrix for a rotation angle $-\theta(\tilde{\nu})$ yields the equation for the phase corrected spectrum:

$$B(\tilde{\nu}) = B_c(\tilde{\nu}) \cos(\theta(\tilde{\nu})) + B_s(\tilde{\nu}) \sin(\theta(\tilde{\nu})). \quad (3.42)$$

To obtain the knowledge of $\theta(\tilde{\nu})$, we use the fact that all relevant phase effects in our optics and electronics vary slowly and smoothly with wavenumber. Because of this, we can just take the phase spectrum from a low resolution measurement and interpolate it for higher resolution, which solves two problems: A low resolution spectrum experiences less noise in general and thus can give a more precise estimation of a slowly varying phase angle. In case of saturated lines a higher resolution spectrum drops to zero and it is not possible to calculate a phase angle, while a spectrum of sufficiently low resolution still has enough available information to estimate the phase angle. This low resolution spectrum is typically taken from the same IFG, by just using it to a lower maximum OPD. This is especially true for single sided IFG, where only a short double sided part is available for phase correction. In these cases the phase function is again calculated from a low resolution double sided IFG and sometimes even further smoothed by fitting a polynomial to it. This estimation for the phase function is then sufficient to perform the phase correction on the high resolution spectrum obtained from the single sided IFG. This method of phase correction is often called Mertz method (Mertz, 1967).

Actual implementations of FT and phase correction usually differ in a few details. Instead of calculating the cosine and sine FT of the IFG, it is rather common to calculate a complex FT and taking the real and imaginary part of the resulting spectrum. This is of course equivalent, since the complex FT of the function $g(\delta)$ is $\mathcal{F}_c[g(\delta)](\tilde{\nu}) + i\mathcal{F}_s[g(\delta)](\tilde{\nu})$, where i is the imaginary unit. In this case, the identification of the cosine and sine FT as components of a vector along a phase angle $\theta(\tilde{\nu})$ is straight forward and does not require the identification via Equation 3.40.

3.7 Instrument Line Shape (ILS)

The term instrument line shape (ILS) describes the shape of an infinitely sharp line in a spectrum measured by the instrument in question. In an equivalent definition, the ILS is the function which convolved with the real spectrum yields the

measured spectrum (Equation 3.9). In FTIR spectroscopy, the maximum OPD, the apodization and the self-apodization of the IFG determine the shape of the ILS (Equation 3.33). But effects of imperfect instruments, for example due to misalignment, can further alter the ILS.

There are typically two relevant imperfections in this context and they both refer to imperfections in the interferometer. The first one is modulation efficiency. It is possible that the modulation strength of the interferometer does change with OPD. A typical example is vignetting or other imperfections which reduce the overall light throughput of the interferometer at a specific OPD. This is basically a physical implementation of an apodization function and modifies the ILS as such. The second one is phase error. Subsection 3.6.2 discussed multiple sources of phase error and how to correct for it. There we just assumed a constant phase error for each wavenumber. It is, however, possible that this phase error varies with OPD, for example due to variable mirror velocity along the interferometer arms. The phase correction then only removes the phase error for small OPD, since typically a low resolution spectrum (meaning small OPD) provides the phase information. Phase effects typically include sine components in the ILS, making it asymmetric.

To get an accurate description of the ILS, it is necessary to describe or parameterize modulation efficiency and phase error. Typically, they vary slowly along OPD, which allows parameterization at a few grid points or even with a single parameter each. Hase et al. (1999) introduced this together with two types of parameterization: a so called *simple model* and an *extended model*. While the extended model parameterizes modulation efficiency and phase error at multiple grid points along the OPD, in many applications it can be sufficient to use the simple model. It describes the modulation efficiency as a line from unity at ZPD to a parameterized modulation efficiency at maximum OPD. Further, it assumes a constant phase error along the full range of the interferometer. This latter assumption is unrealistic, since the phase correction removes this kind of error. A phase error curve, which starts at zero and shows deviations at higher OPD might be more realistic. But it turns out that a constant phase error can be a sufficient parameterization for the types of asymmetries that such more complex phase errors produce. I employ only the simple model in the context of this thesis.

To calculate an ILS for any parameterization, it is necessary to implement the above descriptions of modulation efficiency and phase error. There is a straight forward, but not computationally efficient way to do this: Simulate the IFG of a monochromatic line, apply a FT, and extract the ILS from the resulting spectrum.

Figure 3.2 shows this process step by step and illustrates again how modulation efficiency and phase error, but also self-apodization and apodization influence the spectrum/ILS. In a last step (not shown here), the resulting line spectrum is centered at zero, cut to specified size to both sides of the peak, and normalized. I implemented this, together with computationally more efficient methods, in a small python package called `ftslineshape`. This package only covers a subset of the functionality of the well established software package `linefit` (Hase et al., 1999), but provides this subset accessible for python scripts. With this, it also provides an easy, high-level access for visualization and educational purposes. I perform all ILS calculation with this package.

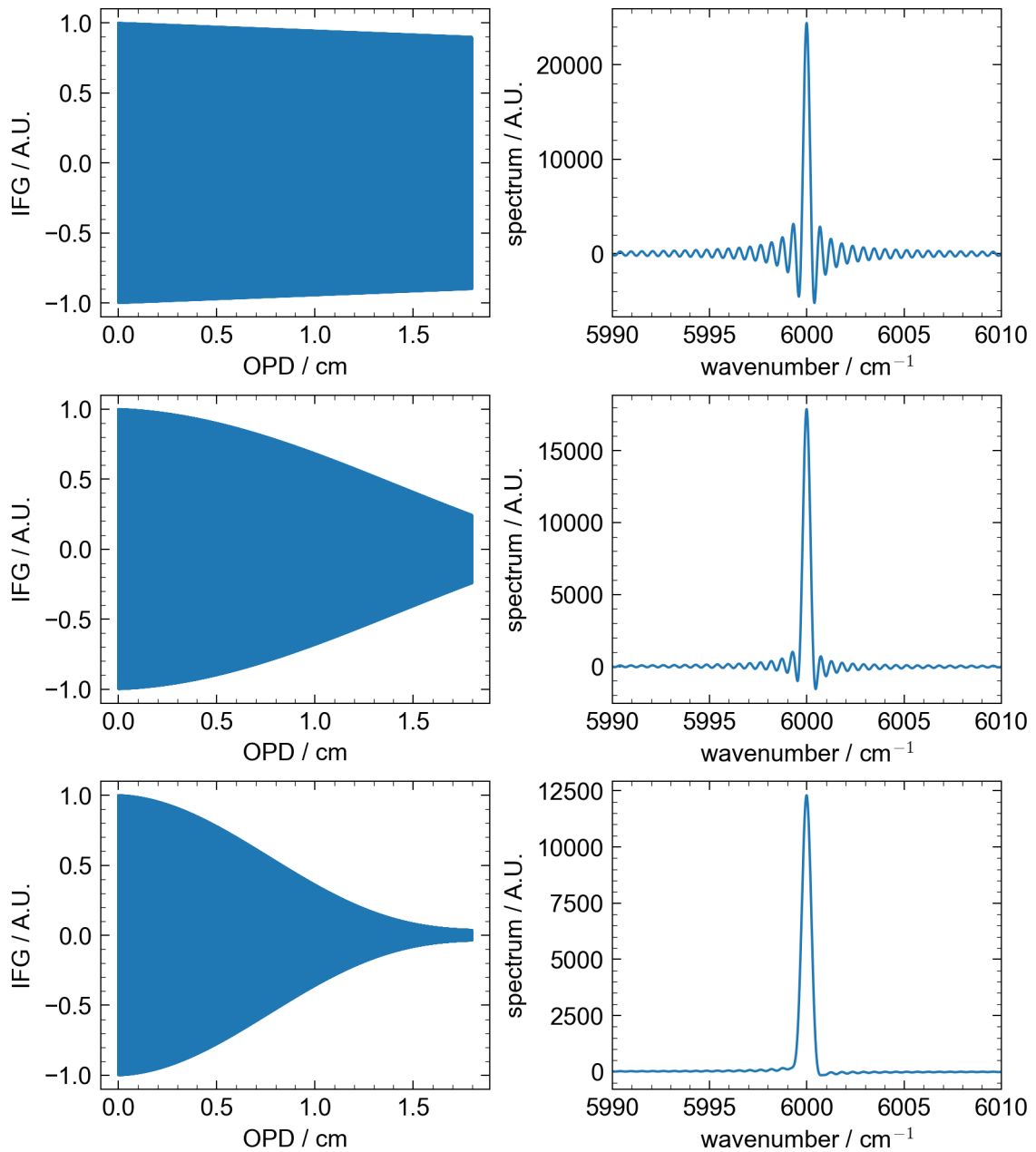


Figure 3.2: Calculation of an ILS according to the simple model. Plots in the left column show monochromatic IFGs for a line at 6000 cm^{-1} . Single oscillations in the IFG are not visible. Plots in the right column show the respective spectrum after FT. Top row: Monochromatic IFG and resulting spectrum with a modulation efficiency of 0.9 and a constant phase error of 0.05. Middle row: Now after accounting for self-apodization at 6000 cm^{-1} and for a beam divergence half angle of 12 mrad, according to Equation 3.28. Bottom row: Now after apodization with a Norton-Beer medium function.

4 Methods

In this chapter, I describe the methods used in experiments and analysis. I first describe the open-path setup in detail, including design choices and implementation. The chapter then continues with a description of the trace gas retrieval software, which extracts information on different gases from the spectra. Further, I describe the data post processing used to make the retrieved information comparable to different data sources and to analyze its precision. The chapter closes with a description of the bias correction method I employ when comparing the data of the open-path system to the data of the in-situ analyzer.

4.1 Open-Path Setup

4.1.1 Location

The open absorption path of the setup extends between the IUP and the old building of the physics institute (OPI). It has a one way length of (1553 ± 1) m, as determined with a laser rangefinder. Figure 4.1 depicts an aerial view of the city of Heidelberg and the location of the path within it. The path crosses mostly over residential area, but also a major road close to the IUP, which experiences a lot of commuter traffic. The spectrometer/interferometer, the telescope, the detector and nearly all of the optics are located in the roof-top observatory of the IUP (Figure 4.2, left), at the western end of the path. A retro-reflector array is located on the roof of the OPI (Figure 4.2, right), at the eastern end of the path.

The IUP roof top houses additional important instrumentation, most notably, the air inlet for an in-situ analyzer. The analyzer is a cavity ring-down spectroscopy (CRDS) system by the manufacturer Picarro (Inc., Santa Clara, CA) of the type G2201-i. In this work, the in-situ data is used for comparison and bias correction. The whole system, including the air drying and calibration setup and process, is described in detail by Hoheisel et al. (2019) and Hoheisel (2021). The second important piece of instrumentation is the weather station on the roof of the institute, which provides measurements of temperature, wind speed, wind

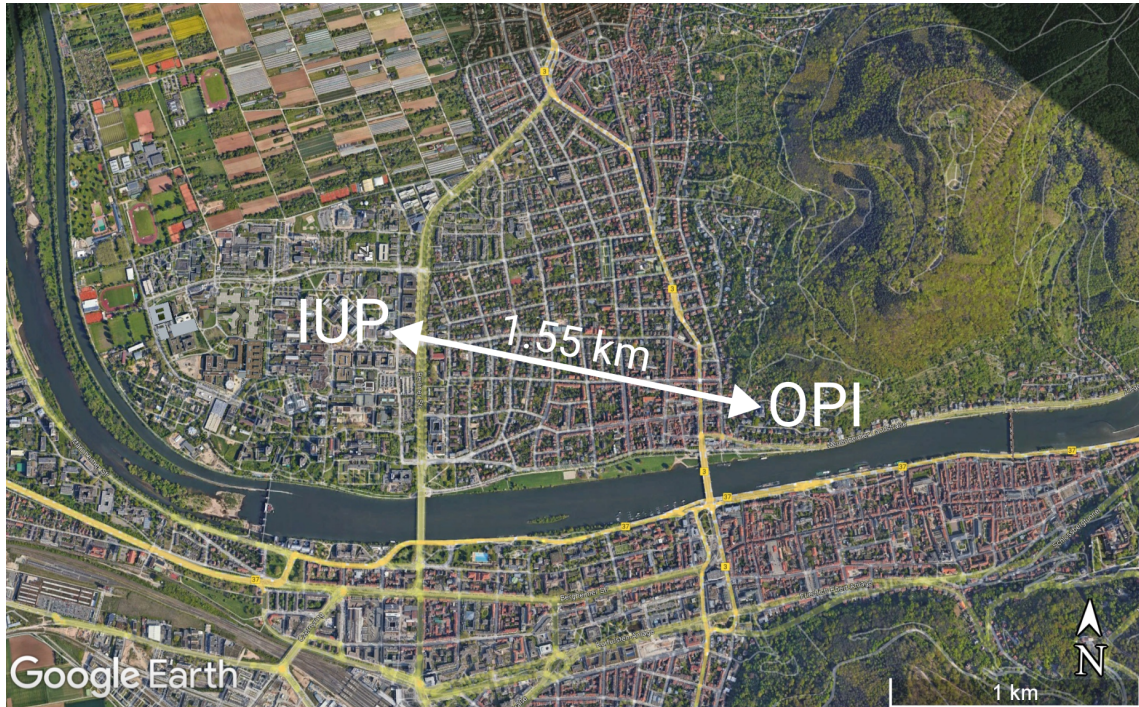


Figure 4.1: Location of the atmospheric absorption path in the city of Heidelberg, Germany. All active components are located at the western end of the path, on the roof of the IUP, about 30 m above ground. These components include the spectrometer, the telescope, the reference in-situ analyzer and a weather station. A retroreflector array forms the east end of the path and is located on the roof of the OPI. The absorption path has a total length of (1553 ± 1) m and the ground beneath it is mostly flat (slow variations within 5 m). During the last 200 m (in the east), the ground rises nearly linearly by about 20 m. The absorption path crosses mostly residential area, with the notable exception of a major road with heavy commuter traffic at the west end, just 120 m from the IUP.



Figure 4.2: Left: The roof top observatory of the IUP, containing the spectrometer and telescope. Right: View of the reflector array at night, co-aligned with the telescope. The array is visible as a bright spot in the center of the image on the dark roof of the OPI.

direction, humidity and pressure in intervals of 1 min.

4.1.2 Open-path optics

The design of the open-path optics follows two central specifications:

1. The light should first pass through the interferometer and then along the absorption path.
2. The open-path telescope design should be fiber based.

The first specification ensures that light scattered into the light path (usually sun light) is not modulated by the interferometer and so does not create a modulated signal on the detector. It only creates a constant offset in the detector signal instead. Hence, it does not produce a spectral signal after the FT. This is a common principle in modern FTIR analyzers and is a well known technique to reduce the impact of scattered light or even the own thermal emission of the analyzed gas, if the analysis is performed in the long wavelength infra red (e.g. Yokelson et al., 1997). The second specification allows for easier pointing of the telescope and in general for a mechanical decoupling of telescope and spectrometer. A fiber additionally homogenizes the illumination of the detector. Griffith et al. (2018) also employed a fiber coupled telescope, even though subsequent works abandoned the fiber coupling to achieve greater light throughput (Deutscher et al., 2021).

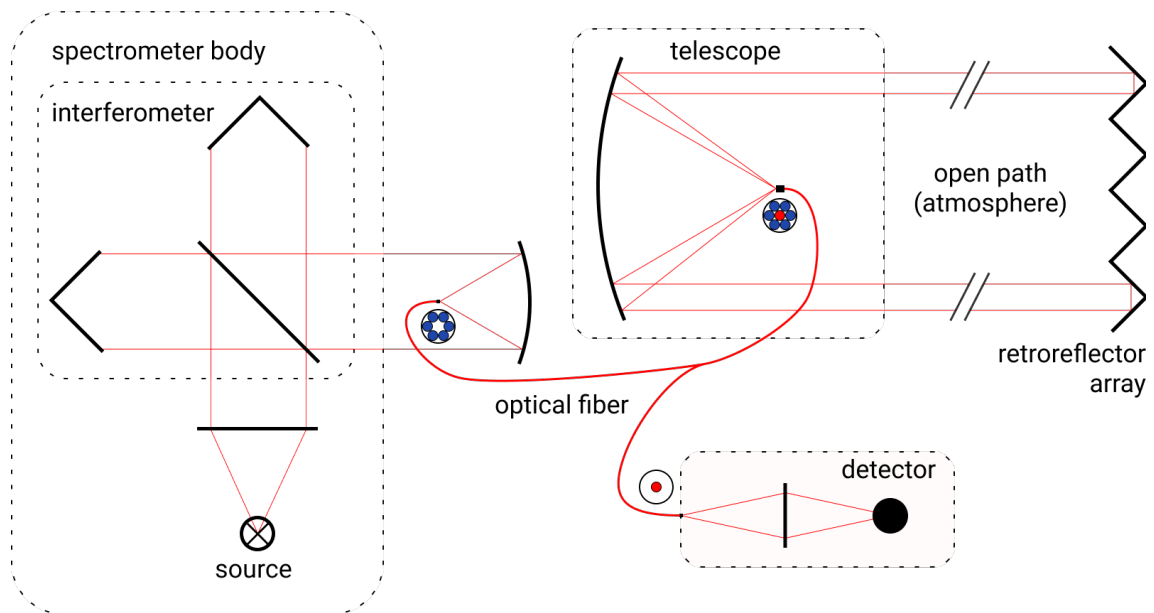


Figure 4.3: Schematic of the open-path optics. The light travels from the source through the interferometer, and then couples into a fiber bundle (depicted in blue). The open-path telescope then collimates the light and sends it to the retro-reflector array, where it is returned. Along this path, absorption and attenuation occurs, according to the atmospheric composition and physical state (e.g. pressure and temperature). The telescope focuses the light into a single receiving fiber (depicted in red). In a last step, an optic images the light onto the photo diode of an external detector module.

However, this was achieved by a rigid coupling between the telescope and the spectrometer and then pointing with the integrated unit, which is only feasible with compact low resolution spectrometers.

Following these specifications, I settled for the design outlined in Figure 4.3. The light path is as follows:

1. Emission by the source, the internal halogen lamp of the spectrometer.
2. Collimation with an off-axis parabolic mirror (30°, effective focal length 418 mm, diameter 75 mm) and an entrance aperture (diameter 2 mm).
3. Transmission and modulation through the interferometer.
4. Coupling into a fiber bundle ($6 \times 200 \mu\text{m}$, length 5 m, VIS-IR silica), via a spherical mirror (focal length 150 mm, diameter 75 mm).

5. Collimation by the spherical telescope mirror (focal length 813 mm, diameter 406 mm).
6. Transmission through the atmosphere and absorption (length 1553 m).
7. Reflection at an array of retro-reflectors (41 solid ultraviolet (UV) quartz cube corners, diameter of 53 mm each, Figure 4.4).
8. Again transmission through the atmosphere and absorption.
9. Coupling in a central receiving fiber (200 μm , length 5 m, VIS-IR silica) in the center of the fiber bundle by the telescope mirror.
10. Focusing on the photo diode of the detector. The detector fore-optics are detector specific.

For coupling the light from the interferometer to the fiber bundle, I chose a spherical mirror over an off-axis parabolic mirror to allow for easier adjustment. Consequently, the fiber bundle has to be placed on the optical axis in front of the spherical mirror, blocking a portion of the light. I determined the one way path length of (1553 ± 1) m with a laser rangefinder and it accounts for the travel distance within the tube of the telescope. It does neither account for any traversed air before coupling into the sending fiber bundle (e.g. within the spectrometer or in front of it), nor for after leaving the receiving fiber (e.g. within the detector fore-optics). The detector fore-optics differ for the two different detectors and will be discussed in Subsection 4.1.4. The principle design of the telescope is based on Merten et al. (2011), who originally developed it for UV differential optical absorption spectroscopy and which was utilized since then to great success (Nasse et al., 2019; Kuhn et al., 2023). It is important to note that the fiber bundle is not directly placed in the focus of the telescope mirror, but slightly detuned. The concept relies on imperfect imaging of the telescope mirror in combination with the lateral displacement of a ray of light when being reflected by a cube-corner retro-reflector to wash out the returned image of the sending fibers and optimize the amount of light coupled into the central fiber. As a result, a calculation of the possible transmission of such a telescope system requires raytracing simulations. To get a very rough upper limit of the achievable transmission we can calculate the geometrical loss of the light spot at the reflector array. With a focal length of 813 mm and (including cladding and packaging) a rough fiber bundle radius of 0.4 mm, the resulting collimated beam has a divergence of approximately 0.5 mrad. After a traveling distance of 1550 m and an initial beam



Figure 4.4: Picture of the reflector array with its 41 solid UV quartz cube corners. The diameter of each cube corner about 53 mm, with the exact shapes and sizes varying.

diameter of 0.4 m, the beam has a diameter of 1.9 m at the reflector array. The 41 retro-reflectors cover only about 3% of the beam area. Other effects further reduce this transmission. Such effects include the (imperfect) imaging on the receiving fiber, blocking of light by structural elements of the telescope (mainly fiber mount), extinction due to scattering along the path, diffraction in the atmosphere, and a loss of about 8% at every air-glas interface (when coupling into the fiber or at the reflectors)

4.1.3 Spectrometer

The spectrometer is an IFS 125HR, manufactured by the company Bruker Optics GmbH & Co. KG, Ettlingen, Germany. It is a high resolution FTIR spectrometer for scientific applications, allowing for flexible configurations and modifications. The available resolution depends on the length of the interferometer arm: The instrument at the IUP allows for a maximum optical path difference of 135 cm,

which corresponds to a nominal resolution of 0.0074 cm^{-1} . The spectral range of the instrument is constrained by the photosensitivity of the available detector diodes and the reflectance and transmittance of the optical elements like mirrors, windows and BS. The IFS 125HR at the IUP is equipped with aluminum mirrors, enabling good performance from the NIR to the near UV. It is further equipped with a CaF_2 BS, which allows operation from NIR to near UV, and the same holds for the installed CaF_2 windows. The spectrometer is further equipped with several different detectors (InGaAs, Si, GaP, SiC) to accordingly span the wide spectral range from NIR via the visible to the UV. However, these pre-installed detectors are not a good choice for the open-path measurements within this thesis, mostly because they are not sensitive enough for this purpose or at least have too high of a noise floor. Subsection 4.1.4 provides more details on this topic.

The field of view (FOV) of the interferometer is limited by the selectable entrance aperture diameter (within this work always 2 mm) and the fixed focal length of the main collimating mirror (418 mm). The interferometer is a cube corner design, with the moving reflector on a sledge carriage, using 75 mm optics, of which approximately 65 mm are used.

4.1.4 Detectors and Detector Optics

The internal detectors of the IFS 125HR spectrometer are not well suited for an open-path application. This is due to the following two reasons, with the second being the more constraining one:

1. We based the open-path telescope design on optical fibers, with the return light transmitted from a single fiber. A point to point image of this fiber onto a photodiode of an external detector is the easiest and most efficient way of measuring the returning light.
2. Bruker designed the detectors within the instrument to handle the irradiance span from the internal halogen source and up to direct sun light. This already spans up to two orders of magnitude, especially when combined with limited light throughput to allow for high resolution measurements (Section 3.3). With the utilized telescope optics and other losses the transmission drops by at least two orders of magnitude or more. The internal detectors are either too noisy or completely unable to measure these small signals.

Hence, I use two external detectors, which I optimized for low light conditions. First, I built a custom detector, based on a room temperature (RT) InGaAs pho-

todiode (Hamamatsu G12181-003K). Later, I carried out a long deployment period using a detector module built by Bruker, containing a TE cooled extended InGaAs photodiode (Hamamatsu G12183-210KA-03). For an uncooled RT photodiode it was necessary to settle for a lower spectral bandwidth, to avoid the thermal noise that a lower cut-on frequency comes with. Thus, the custom RT diode is not sensitive to the 2 μm absorption bands of CO_2 , as well as to bands of CH_4 and CO at even lower frequencies. Due to this limitation, the RT initially served two purposes: first, serve as an engineering model while setting up the open-path optics and demonstrating the concept with an external detector, and, second, to gather experience for a later specification and procurement of a TE cooled detector. From here on, I refer to the detector modules as RT detector and TE detector respectively. In the following, I describe both detectors with their respective coupling optics. In the case of the custom RT detector, I walk through the considerations behind the design.

RT detector

The photoactive element of the RT detector is an InGaAs photodiode with a high wavelength cutoff at around 1.85 μm . This gives only access to the 1.6 μm band of CO_2 and CH_4 . However, these photodiodes come with fairly high shunt resistances ($\text{M}\Omega$ and above) and hence with good noise performances, rendering cooling of the photodiode unnecessary.

To design a detector module, specifically the front end electronics, we need an estimation of the photocurrent. For this, we need to know the total optical power transmitted to the photo diode in our spectral region of interest (6000 cm^{-1} to 8000 cm^{-1}). Starting at the source, a thermal radiator at 3000 K emits about $10^2\text{ W m}^{-2}\text{ sr}^{-1}\text{ cm}$ in this spectral region, according to Planck's radiation law. The étendue of the optical system is approximately limited to $10^{-8}\text{ m}^2\text{ sr}$. The optical bandwidth spans a range on the order of 10^3 cm^{-1} . Finally, we need to assume at least a loss factor of 10^{-3} , mostly due to the open-path telescope transmission (Merten et al., 2011), but also accounting for the loss due to optical surfaces, the BS, the emission coefficient of the light bulb, and so on. With a photosensitivity of about 1 A W^{-1} , we arrive at an estimation of $1\text{ }\mu\text{A}$ photocurrent. To convert this to the dynamic range of our ADC of 10 V, we need a front end with a transimpedance gain of $10\text{ V}/1\text{ }\mu\text{A} = 10\text{ M}\Omega$. Since we operate the FTIR instrument at a scanning speed of 20 kHz equivalent, which translates to a rough upper limit of 15 kHz modulation for our optical signals, we apply a factor of 2 and limit the bandwidth of our amplifier electronics at around the cutoff fre-

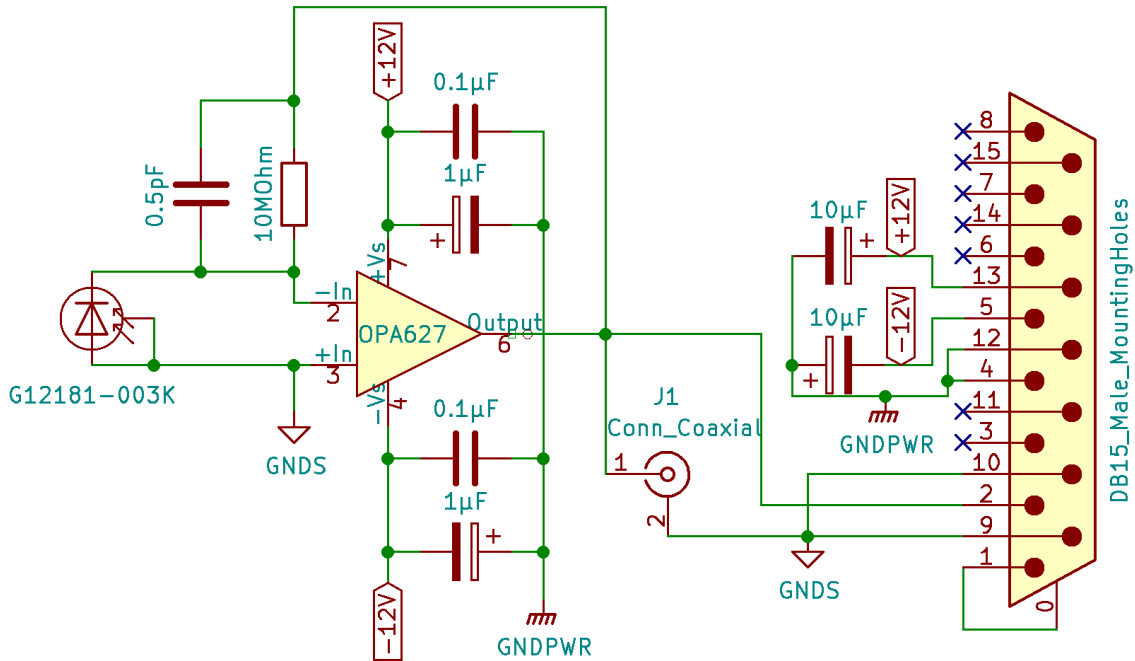


Figure 4.5: Schematic of the custom built RT detector. I limited the amplifier electronics to a high gain transimpedance amplifier. The photodiode is unbiased and directly connects to both input terminals of the operational amplifier. The amplifier is a low noise amplifier with high input impedance.

quency $f_c = 30$ kHz. The implementation of this limit is a simple RC-element in the feedback loop of the transimpedance amplifier, where a capacitance in parallel to the amplifier resistance reduces the amplification for high frequencies. The cutoff frequency of such an RC-element is $f_c = (2\pi RC)^{-1}$ and we can solve this for the necessary feedback capacitor C for our calculated feedback resistor $R = 10$ MΩ:

$$C = \frac{1}{2\pi R f_c} \approx 0.5 \text{ pF.} \quad (4.1)$$

Figure 4.5 shows the schematic of the RT detector and amplifier as used within this work. Since we deal with a low photocurrent, the photodiode (Hamamatsu G12181-003K) is unbiased, since the resulting leakage current might contribute substantially to the shot noise of the diode. I designed the front end around an OPA627, a high end operational amplifier by Texas Instruments, which exhibits exceptional low noise performance and high input impedance. The feedback loop of the transimpedance amplifier is closed by the aforementioned RC-element of a 10 MΩ resistor and a 0.5 pF capacitor. The power supply is a ± 12 V bus provided by the spectrometer, with a separate ground (GNDPWR in schematic). There are several filter capacitors to safeguard against noise on the power bus, ranging

from 0.1 μF to 10 μF . The polar capacitors are tantalum capacitors, while the unpolar capacitors are ceramic. The signal is referenced to a separate signal ground (GNDS in schematic). A coaxial connector for testing purposes allows for easy access to the signal line with an oscilloscope. The layout of the connector follows the pin-out specification of the spectrometer interface.

The detector optics consist of a single spherical, gold coated mirror (diameter 75 mm, focal length 75 mm), which couples the light from the receiving fiber to the detector. The fiber end is mounted next to the photodiode (about 1 cm apart) and projected onto the photodiode. The small lateral distance between fiber and photodiode is necessary to reduce spherical aberrations. This optic has two advantages: it minimizes optical surfaces (and with that losses) and is free of chromatic aberrations by using a mirror. The major drawback of this optic, which was originally conceived as a quick prototype solution, is the difficulty of shielding the diode and amplifier against electromagnetic interference (EMI). The close proximity of fiber and the electronics make it difficult to enclose the electronics while not interfering with the light path. Hence, from time to time, it experiences issues with induced noise.

TE detector

The photoactive element of the TE detector is an extended InGaAs photodiode with a high wavelength cutoff at around 2.55 μm . This gives access to the bands of CO_2 at 2 μm , as well as to CH_4 and CO at 2.3 μm . But, the low shunt resistances ($\text{k}\Omega$ and above) of these photodiodes necessitate cooling to improve noise performance.

The detector module from Bruker contains a TE cooled extended InGaAs photodiode (Hamamatsu G12183-210KA-03). The TE cooler is a two stage design, bringing the operating temperature of the diode down to about -30°C . This is necessary, since extended InGaAs diodes have a substantially lower resistance, up to three orders of magnitude, than their not extended counterparts. This results in a more than an order of magnitude worse noise performance. Reducing the temperature of the diode reduces the thermal noise and increases the resistance of the diode. I modified the detector module by replacing one of the feedback RC-elements it shipped with to increase the transimpedance gain. The detector currently operates with a 10 $\text{M}\Omega$ resistor and no feedback capacitor.

The detector optics for the TE detector are a bit more complex than for the RT detector. This is due to the standardized detector housing by Bruker, which does not allow to mount the fiber close to the photodiode. This is an acceptable draw-

Table 4.1: Settings for the FTIR instrument.

ID mode name	1 benchmark	2 one minute	3 high resolution
OPD _{max}	1.8 cm	1.8 cm	9 cm
nominal resolution	0.55 cm ⁻¹	0.55 cm ⁻¹	0.11 cm ⁻¹
coadded scans	34	6	16
measurement duration	306.7 s	52.7 s	285.6 s
repetition period	311.4 s	57.4 s	295.3 s
IFG type	double sided	double sided	single sided
typical SNR	690	240	130

back, since the housing provides excellent shielding for the photodiode and the amplifier against EMI. On paper, an optic consisting of two off-axis parabolic mirrors would be a perfect, non-chromatic solution. In practice, such an optic is difficult to set up and adjust accurately. The alternative solution, which is currently in use, consists of two achromatic doublets (diameter 25.4 mm, focal length 50 mm, Thorlabs AC254-050-C-ML), imaging the fiber onto the detector area. Choosing a lens system over mirrors comes with the drawback of chromatic aberrations. The achromatic doublets reduce, but do not negate this. However, this is acceptable in this case, since the utilized photodiode has an active area with a diameter of 1 mm and the fiber a diameter of 0.2 mm. This means, that even for wavelengths where the photodiode is not exactly in the focal plane, the full image will fit on the photodiode and no light is lost. Finally, a long pass filter (Thorlabs FELH1100) behind the achromatic doublets filters wavelengths below 1.1 μm to reduce the number of photons on the detector and, with that, reduce shot noise.

4.1.5 Instrument Settings

I operated the open-path setup in three main modes to probe the parameter space of such measurements, while still ensuring long, not too fractured, and comparable measurement time series. The three modes of operation are identical in the optical setup but differ in the settings for the spectrometer. Table 4.1 provides an overview of the different modes. The number of coadded scans is the sum of forward and backward scans. The measurement duration gives the total time of a measurement, and the repetition period additionally includes the time between two measurements, where the instrument is preoccupied with data processing and setup for the next measurement.

The first mode, called “benchmark mode”, uses the same resolution of 0.55 cm⁻¹

and overall measurement time of about 5 min as Griffith et al. (2018) to allow for easy comparison. The second mode, called “one minute mode”, increases the temporal resolution to about 1 min, while keeping other parameters the same as the “benchmark mode”. The third and final mode, called “high resolution mode”, increases the spectral resolution to 0.11 cm^{-1} but keeps the measurement time of 5 min of “benchmark mode”. The “high resolution mode” measures single sided IFGs, since the interferometer of the spectrometer is not capable of measuring symmetric double sided IFGs for a maximum OPD of 9 cm.

4.1.6 Resulting Spectrum

A typical measurement with the TE detector in the “benchmark mode” (see Table 4.1) with a maximum OPD of about 1.8 cm and 17 scans in each direction produces an IFG similar to the example shown in Figure 4.6.

The operation software “OPUS” of the manufacturer Bruker performs the transformation to a spectrum. It applies a Norton-Beer Medium apodization function, performs the FT, and the phase correction (for more details see Section 3.6). The result is the spectrum in Figure 4.7.

4.2 Trace Gas Retrieval

To retrieve information on the path-integrated CDs of the target gases, I perform fits to the measured spectra. A forward model simulates the spectra based on several input parameters as following:

1. Calculation/Look up of target gas spectral absorption cross-sections, based on temperature and pressure.
2. Calculation of the transmission spectrum based on target gas CDs and spectral absorption cross-sections according to Beer-Lambert’s law (Equation 2.30).
3. Convolution of the transmission spectrum with the ILS of the spectrometer.
4. Multiplication with a polynomial to represent the continuum.

A fit of the forward model to the measured spectra, using a Levenberg-Marquardt implementation for least-squares optimization, retrieves some of these parameters. The retrieval takes a noise estimation from the off-band (3000 cm^{-1} to 4000 cm^{-1}) to weigh the differences between simulated and measured spectrum.

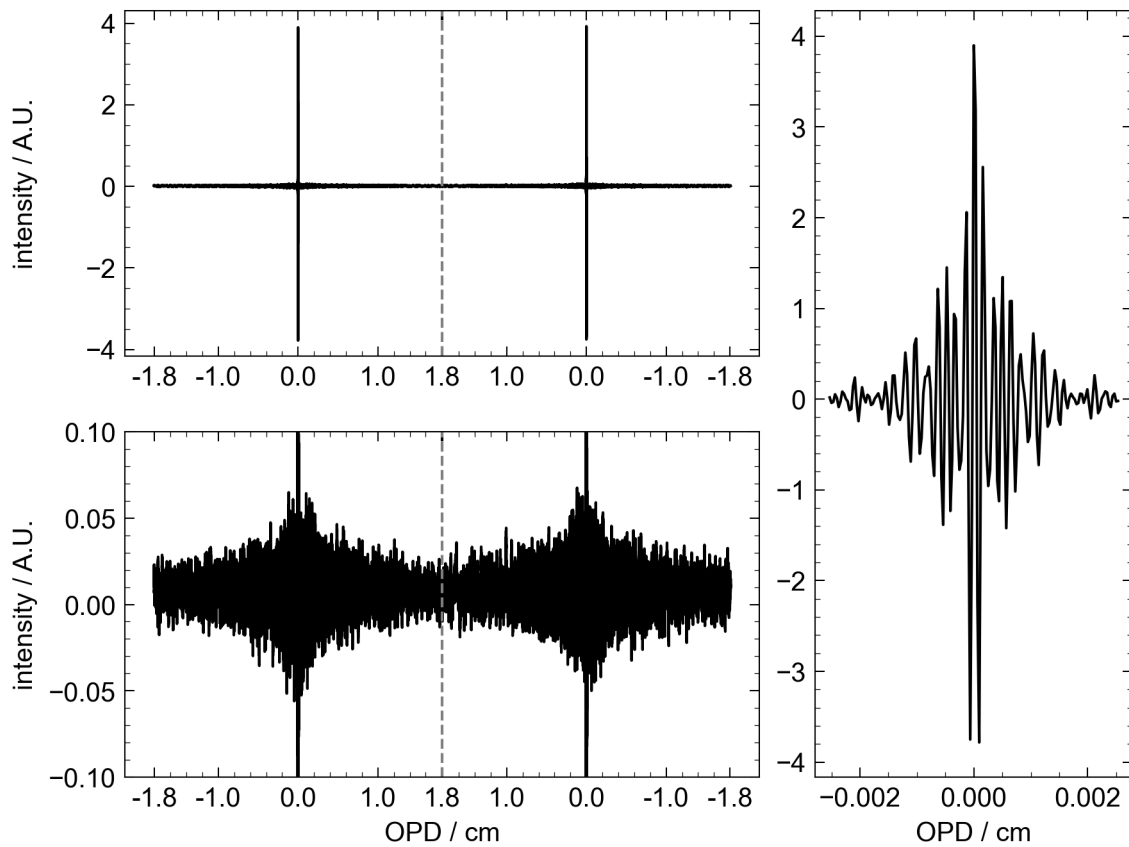


Figure 4.6: Typical IFG recorded with the TE detector, using a nominal resolution of 0.55 cm^{-1} and averaged over 17 scans in each direction over a time of approximately 307 s. The top left panel shows the full IFG, with the grey dashed line separating the forward scan on the left and the backward scan on the right. The bottom left panel shows a zoom on the base line of the IFG. The right panel shows a zoom on the (left) center burst.

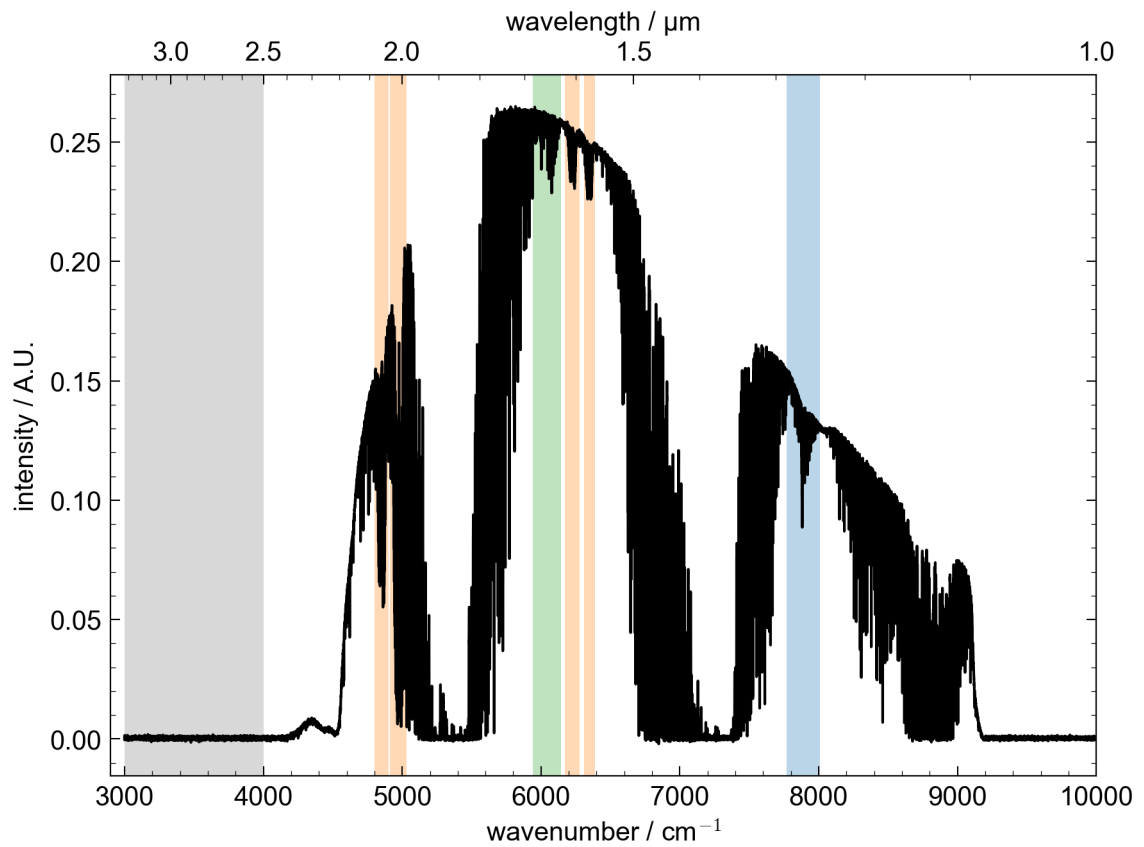


Figure 4.7: Typical spectrum recorded with the TE detector, using a nominal resolution of 0.55 cm^{-1} and integrating over approximately 307 s. The highlighted spectral regions are the main fit windows for CO_2 (orange), CH_4 (green), and O_2 (blue). The grey band marks the area where information on the spectral noise is retrieved. Section 4.2 gives details on the fit windows and information retrieval from the spectrum.

4.2.1 Absorption Cross-Sections

I calculate absorption cross-sections of lines with the Voigt implementation of HAPI (Kochanov et al., 2016), a python interface for the high-resolution transmission molecular absorption database (HITRAN). I use line-by-line data from the 2020 iteration of HITRAN (Gordon et al., 2022). For the CO₂ bands around 5000 cm⁻¹, I augment these absorption cross-sections with additional line mixing corrections (Hartmann et al., 2009; ?). Finally, in the O₂ band at 7900 cm⁻¹, I take into account CIA by fitting a pseudo absorber. To calculate the absorption cross-sections for this pseudo absorber, I use the CIA data currently provided by HITRAN (Karman et al., 2019) for O₂-Air interaction and a temperature and pressure dependent air mass (using the ideal gas law, assuming dry air). I use this composition of absorption cross-sections in all retrievals within this thesis, unless explicitly stated otherwise.

4.2.2 Retrieval Configurations

The retrieval allows for configuration of the following major parameters: Fixed or fitted pressure and temperature, configuration of absorption windows, coupling of absorbers between windows, choice of ILS, and the degree of background polynomial. In general, I use the following global settings:

- Temperature is fitted. *A priori* from the weather station.
- Pressure is fixed. *A priori* from the weather station.
- ILS is calculated for each window, but with global parameters for modulation efficiency and phase error.

Table 4.2 lists all spectral fit windows with the respective fitted species. All windows use a background polynomial of degree 2, except window 6, which uses a polynomial of degree 5. This is necessary, most likely due to the large uncertainty of the broad band CIA structure. HDO and ¹³CO₂ are coupled between windows 2 and 3. CO₂, H₂O, and HDO are coupled between windows 4 to 6. *A priori* values for all gas CDs are at a fixed value. Those are a rough estimation (for each gas) assuming average conditions. The fit is sufficiently well constrained that this does not pose any problems throughout the time series. I use this retrieval configuration in all retrievals within this thesis, unless explicitly stated otherwise, for example in the context of sensitive studies.

Table 4.2: Spectral windows and corresponding fitted trace gases. The main absorbers of interest are highlighted in bold for each window.

window ID	spectral range / cm^{-1}	fitted species
1	4800 – 4900	CO₂ , H ₂ O, HDO, ¹³ CO ₂
2	4910 – 5030	CO₂ , H ₂ O, HDO, ¹³ CO ₂
3	5940 – 6145	CH₄ , CO ₂ , H ₂ O, HDO
4	6173 – 6276	CO₂ , H ₂ O, HDO
5	6308 – 6390	CO₂ , H ₂ O, HDO
6	7770 – 8010	O₂ , O ₂ (CIA), H ₂ O

4.2.3 ILS

Within the retrieval, the ILS is parameterized according to the *simple model* described in Hase et al. (1999) and Section 3.7. The input parameters are the FOV, variable modulation efficiency, and phase error. The retrieval then calculates the ILS for each window separately with these parameters (using the center wavenumber for self-apodization).

A modification of the retrieval does further allow to retrieve the ILS parameters. Within this work, I retrieve the ILS of the full open-path system with this modification by keeping a fixed FOV and fitting modulation efficiency and phase error for a sample size of spectra. This sample typically involves 100 to 300 spectra during stable signal conditions. The ILS retrieval operates in the O₂ window at 7820 cm^{-1} to 8000 cm^{-1} . The final ILS parameters are the mean of all individual retrieved parameter sets. This is only used to retrieve ILS parameters in a statistical approach and explicitly not during evaluation of time series. This is important, since modulation efficiency of the ILS and target gas CDs are typically correlated, especially for low resolution applications. A fixed ILS, as described above, is used for time series evaluations.

4.3 Dry Air Mole Fractions

For many applications, such as comparison to models or other measurements, it is convenient to translate path-integrated CDs into path-averaged dry air mole fractions. There are two approaches to do this. The first is to divide the target gas CD by the measured CD of a dry air mass tracer with known dry air mole fraction. Alternatively the dry air mass can be calculated from information on temperature, pressure, humidity and path length.

A perfect tracer for the first method is O₂, with a known dry air mole fraction

of about 0.20946. One can easily calculate the dry air mole fraction x_Q of a target gas Q :

$$x_Q = \frac{CD_Q}{CD_{O_2}} \cdot 0.20946, \quad (4.2)$$

where CD_Q and CD_{O_2} are the measured CDs of the target gas Q and O_2 , respectively.

The second method relies on available and representative information on the temperature T , the pressure p , and the path length l to calculate a total (wet) air column using the ideal gas law. With further information on humidity, we can subtract CD_{H_2O} , the total water vapor CD, from the wet air column to calculate the total dry air column CD_{dry} :

$$\hat{x}_Q = \frac{CD_Q}{CD_{dry}}, \quad CD_{dry} = \frac{p}{k_B T} l - CD_{H_2O}, \quad (4.3)$$

where k_B is the Boltzmann constant. I denote the dry air mole fraction calculated this way with \hat{x}_Q to avoid ambiguity.

It is possible to measure pressure and path length to high accuracy with readily available equipment. Temperature is easy to measure with high precision, but has higher spatial gradients than pressure and might be unrepresentative for the whole path when measured at a single point (Subsection 5.5.1). Humidity is sometimes more difficult to measure and might show spatial gradients in the vicinity of a water body like the Neckar. But since the water column typically contributes a few percent at maximum to the total air column, a relative error of a few percent on the humidity propagates to an error on the mixing ratio on the level of permille or below. In principle, the calculated dry air mass should be about an order of magnitude more precise than the inference over O_2 as a proxy. As a result, the precision of the calculated dry air mole fractions should then be dominated by the precision of the target gas CD. Because of this, studies like Griffiths and De Haseth (2007) employed this method. However, I calculate most dry air mixing ratios within this work using Equation 4.2, since I find this to actually provide results with higher precision. The details of this finding are discussed in Subsection 5.5.2.

4.4 Precision of Time Series

To estimate the precision of the retrieved values such as gas CDs from the measured time series, I use a statistical estimation called Allan deviations. I calculate

the difference of consecutive measurements and then the standard deviation of their distribution σ_{diff} . If two consecutive measurements are independent measurements of the same quantity, the single measurement uncertainty σ_{single} can be calculated as follows:

$$\sigma_{single} = \frac{\sigma_{diff}}{\sqrt{2}}. \quad (4.4)$$

However, if the measurement uncertainty is on the same order as the changes of the real value between two consecutive measurements, the latter starts to dominate the distribution of the differences and the resulting estimation of the single measurement uncertainty is biased high. As I will show later, 5 min averaging intervals are just short enough to ensure that the single measurement uncertainty due to noise dominates (at least for the TE detector operated in “benchmark mode”). This can be estimated by calculating Allan deviations σ_T for different averaging intervals of length T . If the resulting uncertainties were purely governed by statistics, they would decrease with the square root of the increase of the averaging time:

$$\sigma_T = \frac{\sigma_{T_0}}{\sqrt{T/T_0}}, \quad (4.5)$$

where T_0 is the initial averaging time, with a corresponding Allan deviation of σ_{T_0} . However, once real variability and not the single measurement uncertainty dominates the differences on larger times scales, the corresponding Allan deviations start to deviate from this purely statistical expectation to larger values.

4.5 Bias Correction to in-situ Data

It is necessary to bias correct the measured open-path dry mole fractions to compare them to other data such as the in-situ measurements. This results mostly from errors in the tabulated spectroscopic line parameters, such as line strengths and broadening coefficients. Errors in these values propagate to the calculated absorption cross-section and from there to the estimation of total gas CDs. For HITRAN, the inconsistencies between absorption bands can easily lead to offsets on the order of a few percent (Birk et al., 2021). Different parameterizations of the same band can easily lead to the same level of difference (Malarich et al., 2023). This is a general challenge of remote sensing experiments, which rely on the quality of spectroscopic databases like HITRAN to deliver accurate measurements.

In-situ analyzers do not suffer from these errors in the spectroscopic databases, since they are typically calibrated to well known standard gas mixtures and are highly accurate (Hall et al., 2021). Hence, it is common to bias correct remote

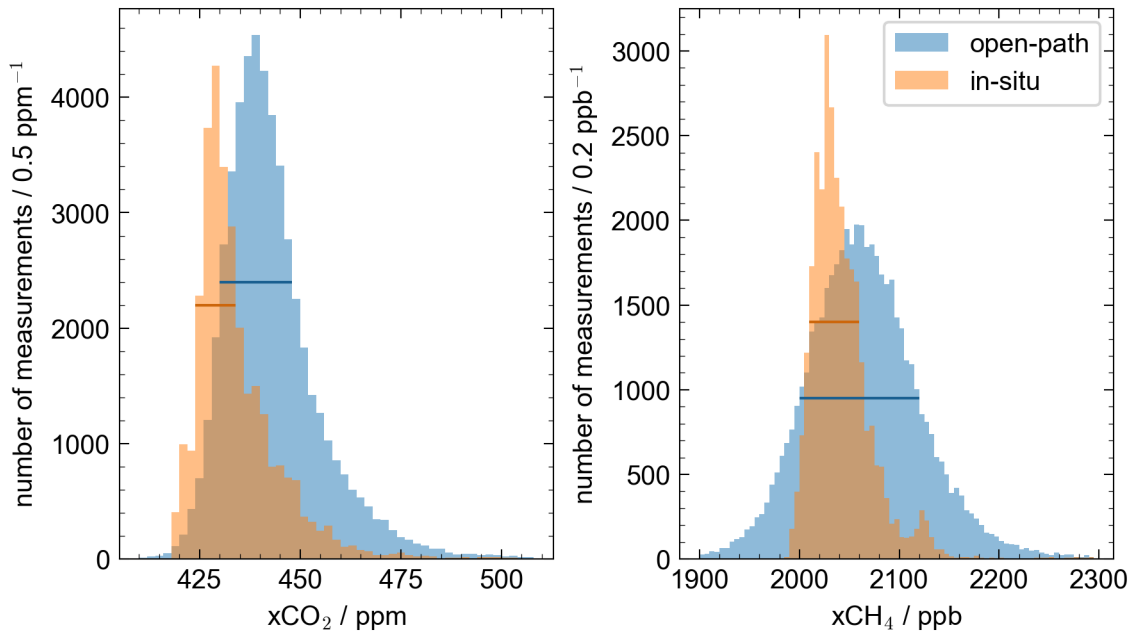


Figure 4.8: Histogram of the measured $x\text{CO}_2$ (left) and $x\text{CH}_4$ (right), each for the open-path instrument (blue) and the in-situ analyzer (orange). Measurements are from the calibration period from Mar. 23 to May 10. A peak at low concentrations, when measuring mostly background air, is visible for both instruments (blue and orange bar respectively). For $x\text{CO}_2$ ($x\text{CH}_4$), there are 33426 (37633) in the selected peak area for the open-path instrument and 17064 (22127) measurements for the in-situ analyzer. Of those, 13633 (16525) are coincident in time. The mean correction factors calculated for all these coincident measurements are 0.9784 (0.9887).

sensing measurements with in-situ measurements (Messerschmidt et al., 2011). I perform this bias correction of the open-path data with the in-situ analyzer as reference. The two instruments measure different bodies of air, by nature and intention. Thus, it would be ideal to perform the bias correction only under conditions where there are no significant spatial gradients within the measurement area and the local concentrations at the IUP are representative for the full absorption path. However, such conditions are hard to identify and would only occur if there are no relevant effects from local emissions compared to the bulk concentration in the boundary layer.

To identify suitable conditions, where local emissions do not play a significant role for the measured concentrations, I examine the histograms of $x\text{CO}_2$ and $x\text{CH}_4$ in Figure 4.8. The histograms exhibit a notable peak at low concentrations and a tail towards higher values. The peaks at lower values correspond to unenhanced measurements, where local emissions are less relevant and presumably the spa-

Table 4.3: Bias correction factors for open-path $x\text{CO}_2$ and $x\text{CH}_4$ measurements, depending on their spectral resolution. I estimated the correction factors from the measurements in the given time period. The given uncertainties on the correction factors are estimates from sensitivity studies.

spectral resolution	correction factor for		time period
	$x\text{CO}_2$	$x\text{CH}_4$	
0.55 cm^{-1}	0.9784(20)	0.9887(50)	2023-03-23 – 2023-05-10
0.11 cm^{-1}	0.9864(20)	0.9726(50)	2023-07-12 – 2023-09-09

tial gradients are small. To calculate a correction factor, I visually identify these peaks and filter for observations which are coincident in both peaks. I determine the final correction factor as the mean of all individual ratios between these selected open-path and in-situ measurements. It is necessary to perform this bias correction separately for measurements with different resolutions, since they differ in their sensitivity to the errors in the spectroscopic data.

Table 4.3 lists the resulting correction factors for $x\text{CO}_2$ and $x\text{CH}_4$ and for both utilized spectral resolutions. It also indicates the measurement period used to calculate the correction factors. To roughly estimate their uncertainties, I perform this bias correction for different subsets of the low resolution measurements, where more data is available. From the resulting spread, I estimate an uncertainty of 0.002 for the $x\text{CO}_2$ correction factor and of 0.005 for the $x\text{CH}_4$ correction factor. Translating this to the accuracy of the bias corrected mixing ratios yields better than 1 ppm for $x\text{CO}_2$ and about 10 ppb for $x\text{CH}_4$. From here on, these factors are applied to all discussed open-path mole fractions.

5 Results

5.1 Overview of the 2023 Campaign

The data presented in this chapter is the result of the ongoing deployment and operation (since 2023-02-08) of the open-path setup presented in Section 4.1. The main purpose of the deployment is to investigate the sensitivity of the open-path setup to local emissions and a variability of meteorological conditions and compare this performance to established measurement techniques such as in-situ sensors. From this overall scientific goal, four technical objectives can be derived: First, to build a dataset which can inform on the performance of open-path setups in comparison to in-situ data. Second, to demonstrate continuous operation of the setup, ideally requiring low effort and maintenance. Third, to test out the parameter space of open-path measurements, compare different modes of operation, and use this to draw conclusions for further deployment configurations. And finally, and more a target of opportunity, to extend this search in the parameter space to the detector hardware and test the validity of a custom build detector module using a RT InGaAs diode, which has lower noise level, but no access to the strong CO₂ bands in the 2 μm windows. Due to the latter two goals, I changed the instrument settings, and in one case even the utilized detector during the ongoing campaign. Table 5.1 gives an overview over the deployment period and the respective experiment configuration. Some results from 2023-02-08 until 2023-07-11 are already published (Schmitt et al., 2023).

In the following, I present the results from this timeseries including the data until 2023-10-09. In Section 5.2, I compare the performance of the two detectors. Following that, I focus on the data obtained with the TE detector and Section 5.3 goes on to compare the different modes of operation. In Section 5.5, I show some key results on how to obtain high quality results from such open-path measurements. Finally, in Section 5.6, I analyze the full timeseries of the TE detector data, independent of the modes of operation, and compare the performance of the open-path instrument to an established in-situ measurement station.

Table 5.1: Overview of the employed instrument settings. Settings in reference to Table 4.1. All times in UTC, rounded to 5 min. The local time switched from UTC+1 to UTC+2 on 2023-03-26.

From	Until	Instrument Settings	Detector
2023-02-08, 14:35	2023-02-15, 17:55	1 (benchmark mode)	TE
2023-02-15, 18:00	2023-02-20, 10:20	1 (benchmark mode)	RT
2023-02-20, 10:25	2023-02-23, 15:15	1 (benchmark mode)	TE
2023-02-23, 15:15	2023-02-24, 12:55	— different experiment	—
2023-02-24, 12:55	2023-03-08, 09:30	1 (benchmark mode)	TE
2023-03-10, 09:30	2023-03-10, 15:35	— different experiment	—
2023-03-10, 15:35	2023-03-22, 10:50	1 (benchmark mode)	TE
2023-03-22, 10:50	2023-03-23, 16:25	— different experiment	—
2023-03-23, 16:25	2023-05-10, 11:25	2 (one minute mode)	TE
2023-05-10, 11:35	2023-05-25, 13:25	3 (high resolution mode)	TE
2023-05-25, 13:50	2023-07-11, 23:10	1 (benchmark mode)	TE
2023-07-12, 11:40	2023-10-09, 08:50	3 (high resolution mode)	TE

5.2 Detector Performances

In this section, I compare the performance of the two detectors, namely a standard InGaAs detector operating at room temperature (RT detector) and an extended InGaAs detector, which is sensitive for the 2 μm band of CO_2 , but which requires cooling (TE detector). Subsection 4.1.4 gives details to both detectors. I first compare the spectra measured by the two detectors and discuss their noise performance. Subsequently, I discuss the resulting performance on retrieved target gases.

5.2.1 Spectra and Noise Performance

As discussed before, Figure 4.7 shows a typical spectrum recorded with the TE detector at nominal resolution of 0.55 cm^{-1} and integration time of 5 min (benchmark mode). Figure 5.1 shows a spectrum recorded with the same settings, but with the RT detector. The first apparent, but expected, difference, is in the low frequency cutoff of the two spectra: The atmospheric transmission window below $1.9 \mu\text{m}$ is not visible in the RT detector spectrum, since the detector material is insensitive to this spectral region. The second large difference is in the high frequency cutoff: The spectrum of the TE detector is cut off at $1.1 \mu\text{m}$, due to an optical filter. The spectrum of the RT detector, simply rolls off to higher frequencies due to a combination of reduced photosensitivity of the detector and the source spectrum. But it does not show a clear cutoff, since there is no according

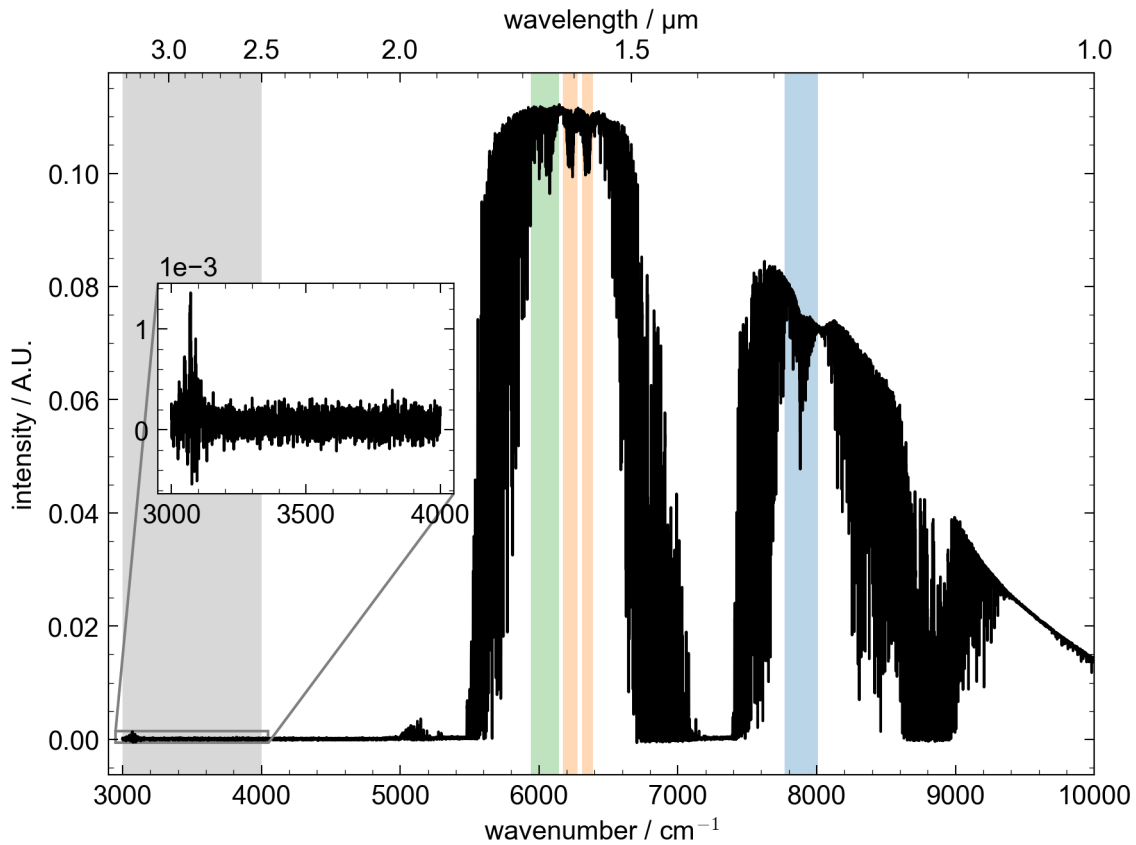


Figure 5.1: Example Spectrum measured with the RT detector. Colored bands as in (Figure 4.7). In comparison with the TE detector, the low frequency cutoff at higher wavenumber is clearly visible. There is no high frequency cutoff at 9200 cm^{-1} , since this detector setup is not equipped with a respective long pass filter. The inset shows a zoom in the noise band. A significant structure at around 3100 cm^{-1} protrudes from the otherwise flat (white) noise. This is most likely caused by electromagnetic interference due to insufficient shielding of the detector and its electronics. The noise structure results in an overestimation of the noise level, making it an high noise outlier in Figure 5.2.

Table 5.2: Theoretical noise contributions for RT and TE detector.

	RT detector	TE detector
SNR	1500	500
estimated photocurrent i_S	0.25 μA	0.34 μA
detector temperature T	300 K	240 K
noisy resistance R	380 k Ω	10 M Ω
shot noise $i_{\text{SN}} = \sqrt{2ei_S}$	$2.8 \times 10^{-13} \text{ A}/\sqrt{\text{Hz}}$	$3.3 \times 10^{-13} \text{ A}/\sqrt{\text{Hz}}$
thermal noise $i_{\text{TN}} = \sqrt{4k_B T/R}$	$4.0 \times 10^{-14} \text{ A}/\sqrt{\text{Hz}}$	$1.8 \times 10^{-13} \text{ A}/\sqrt{\text{Hz}}$
$i_{\text{SN}}^2/i_{\text{TN}}^2$	49	3.4

filter in place. The final difference, which is difficult to judge by eye, is the lower noise level of the RT detector.

To compare the noise level quantitatively, I define the SNR as the ratio of signal and noise according to the following two measures: The signal is the spectrum intensity at 6300 cm^{-1} , between the two CO_2 bands. This spectral region is close to the maximum for both detectors and in a spectral region of interest. The noise is the gaussian noise estimated from the off-band (3000 cm^{-1} to 4000 cm^{-1}). Using this definition of spectral SNR, the RT detector shows a SNR of 1400 to 1500, and the TE detector shows an SNR of 450 to 500 in the adjacent time frames. So at a first glance, the RT detector shows better noise performance by a factor of three.

We further look at the relationship between signal and noise for each detector, beyond a simple typical SNR. Figure 5.2 shows noise plotted over signal for each detector in a log-log plot. It further shows a fit of a function $a\sqrt{s} + c$ for both datasets, where s is the signal, c an offset, and a a proportionality constant. This functions is a simple, but effective noise model, which separates signal dependent shot noise from signal independent noise sources. For the RT detector, the fit is basically a straight line with a slope of $1/2$, which shows us that it is dominated by the shot noise term $a\sqrt{s}$, and is visibly shot noise limited. However, this is not the case for the TE detector. For the TE detector, we see just a minor dependance on the signal (increase in noise of at maximum 20 % when doubling the signal), which shows that other noise contributions than the shot noise still play a major role.

We also estimate the contribution of thermal noise and shot noise using the description in Subsection 3.5.3. I performed such an estimation for a spectrum of average to high SNR for each detector in Table 5.2. I estimated the photocurrent from the respective IFGs, the known transimpedance amplification and the ADC input specification of $\pm 8.5 \text{ V}$. I estimated the detector temperature in the

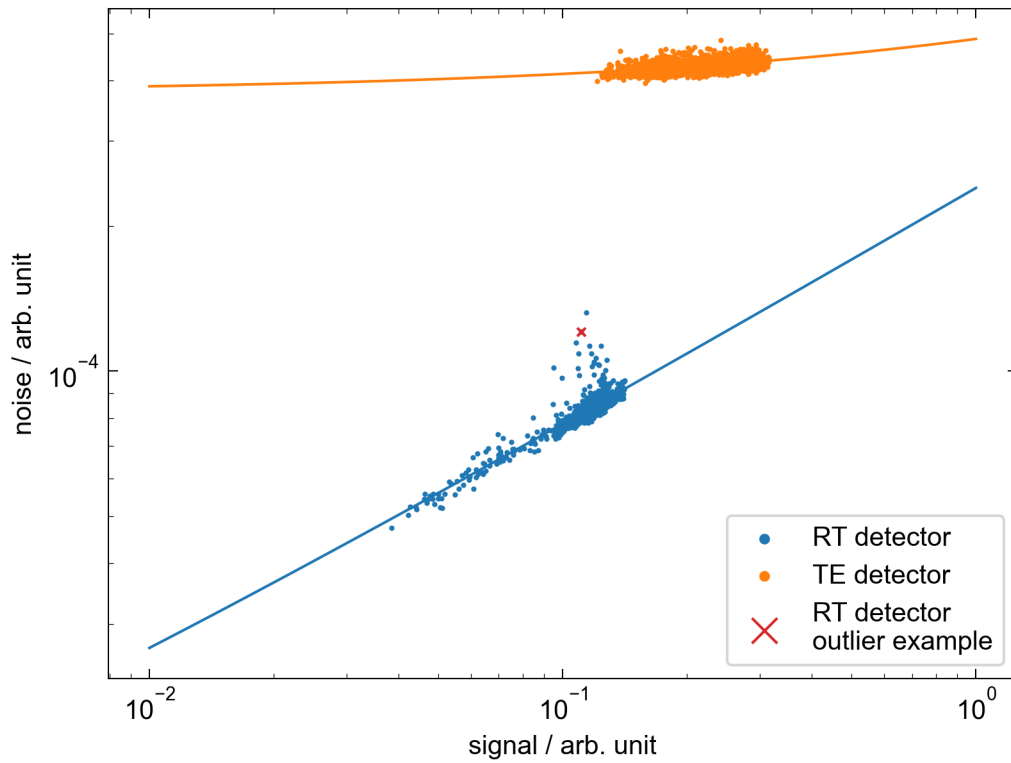


Figure 5.2: Noise performance comparison for RT and TE detector. A noise model, consisting of a constant offset for signal independent noise and a term proportional to the square root of the signal for shot noise, is fitted to both datasets. For the RT detector, the square root term visibly dominates, showing that the detector is shot noise limited, as is ideal. The high noise outliers for the RT detector are a result of inflated noise estimations due to insufficient shielding of the detector electronics. Figure 5.1 shows the spectrum of the marked outlier example, where this is clearly visible. The TE detector on the other hand is far from shot noise limited and operates in a regime where the noise is mostly dominated by constant components, like the thermal noise of the detector diode itself.

typical operating range of the photodiode, since I do not have knowledge on the exact settings of the TE-cooling. The noisy resistance is the total resistance of the photodiode shunt resistance and the transimpedance resistance in parallel. I took the shunt resistance estimation from the photodiode data sheet, according to the estimated detector temperature. It is sensible to compare the quadratic ratio of both noise contributions, since the spectral noise densities add quadratically. We arrive at a quadratic shot noise to thermal noise ratio of 49 for the RT detector and of 3.4 for the TE detector. This shows again, that even for high SNR spectra taken with the TE detector, thermal noise is still a relevant contribution, while the contribution is negligible for the RT detector. We find this result from theoretical estimations, as well as directly from the spectra.

Finally, I have to mention the outliers showing high noise for the RT detector in Figure 5.2, like the specific example marked with a red x. Figure 5.2 shows the spectrum of this specific example. We see a structure at roughly 3100 cm^{-1} in the otherwise gaussian noise band for this spectrum. This results in a gross overestimation of the actual white noise. The noise structure is most likely a result from improper shielding against EMI and can occur also at different places in the spectrum. While it seems to affect only a small fraction of the recorded spectra, an improved shielding is advisable when considering this detector for a long term deployment. This would avoid potential interference of noise structures with target absorption features, if the noise structure ends up in spectral windows used for evaluation.

5.2.2 Timeseries and Target Gas Performance

A side by side deployment would be ideal to compare the performance of the two detectors in actual atmospheric measurements. But since they both rely on the same spectrometer and telescope setup, and the switch between the two detectors requires manual labor, this is not possible. Instead, I performed a short deployment of the RT detector within the larger measurement campaign with the TE detector. The RT detector deployment lasted about 110 h from 2023-02-15 to 2023-02-20. For evaluation of the detector performances with respect to each other, I choose the comparison period from 2023-02-08 to 2023-03-09.

Figure 5.3 shows the timeseries for $x\text{CO}_2$ and $x\text{CH}_4$ in the comparison period. To retrieve information from the RT detector spectra, I ran the retrieval on all spectral windows, which are accessible with the spectral bandwidth (windows 3 to 6 in Table 4.2). To allow for a more informed comparison, the spectra from the TE detector are retrieved twice: once using the same retrieval windows as

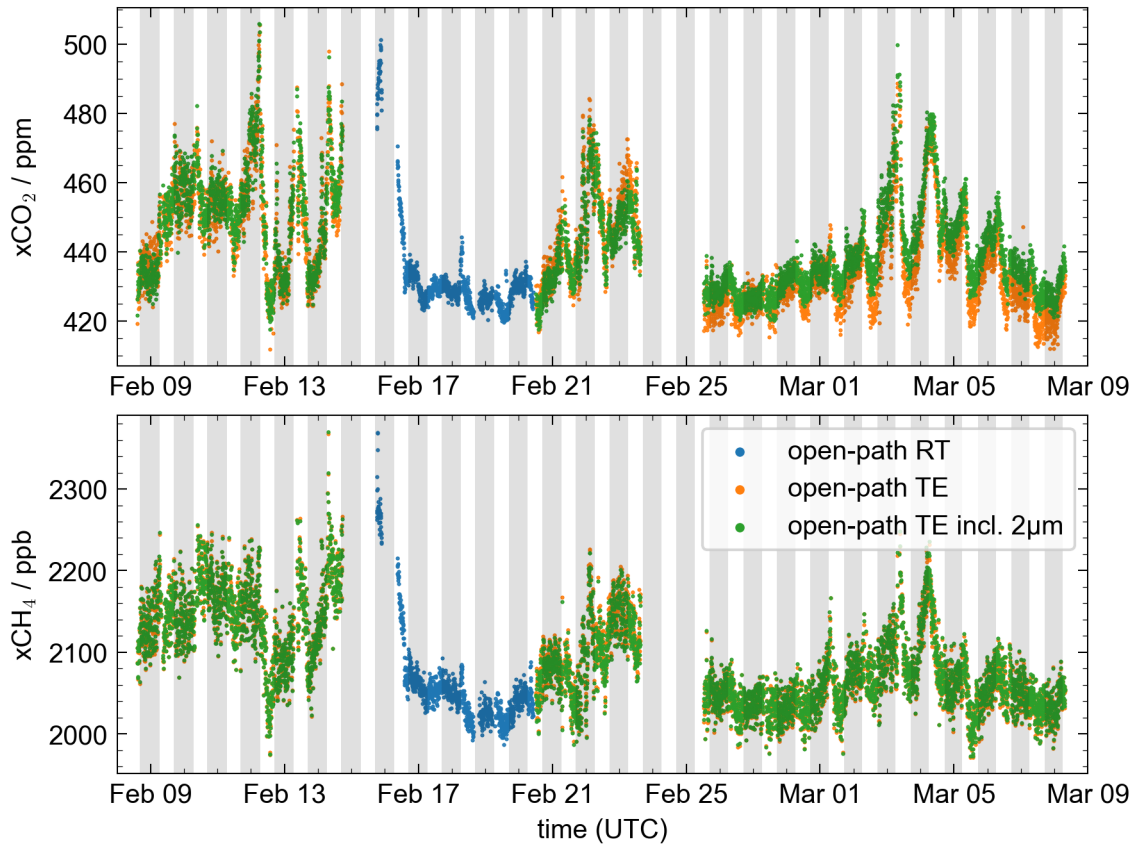


Figure 5.3: $x\text{CO}_2$ and $x\text{CH}_4$ as measured with the RT and the TE detector for the comparison period. The TE detector is once evaluated using the same retrieval settings as the RT detector (orange, omission of the $2\ \mu\text{m}$ windows), and once evaluated using its full spectral band width (green, including the $2\ \mu\text{m}$ windows). The lower scatter of the values measured with the RT detector is clearly visible for both gases. The two evaluations for the TE detector do not differ significantly for $x\text{CH}_4$, since there is no additional information on $x\text{CH}_4$ in the $2\ \mu\text{m}$ windows. This is different for $x\text{CO}_2$, where the inclusion of the $2\ \mu\text{m}$ windows reduces the scatter significantly. In the second half of the period, the two TE detector $x\text{CO}_2$ timeseries drift away from each other. This is caused by a drift between the CO_2 retrieved from the $2\ \mu\text{m}$ windows and the $1.6\ \mu\text{m}$ windows. Figure 5.4 shows a zoom in on the transition region around Feb. 20.

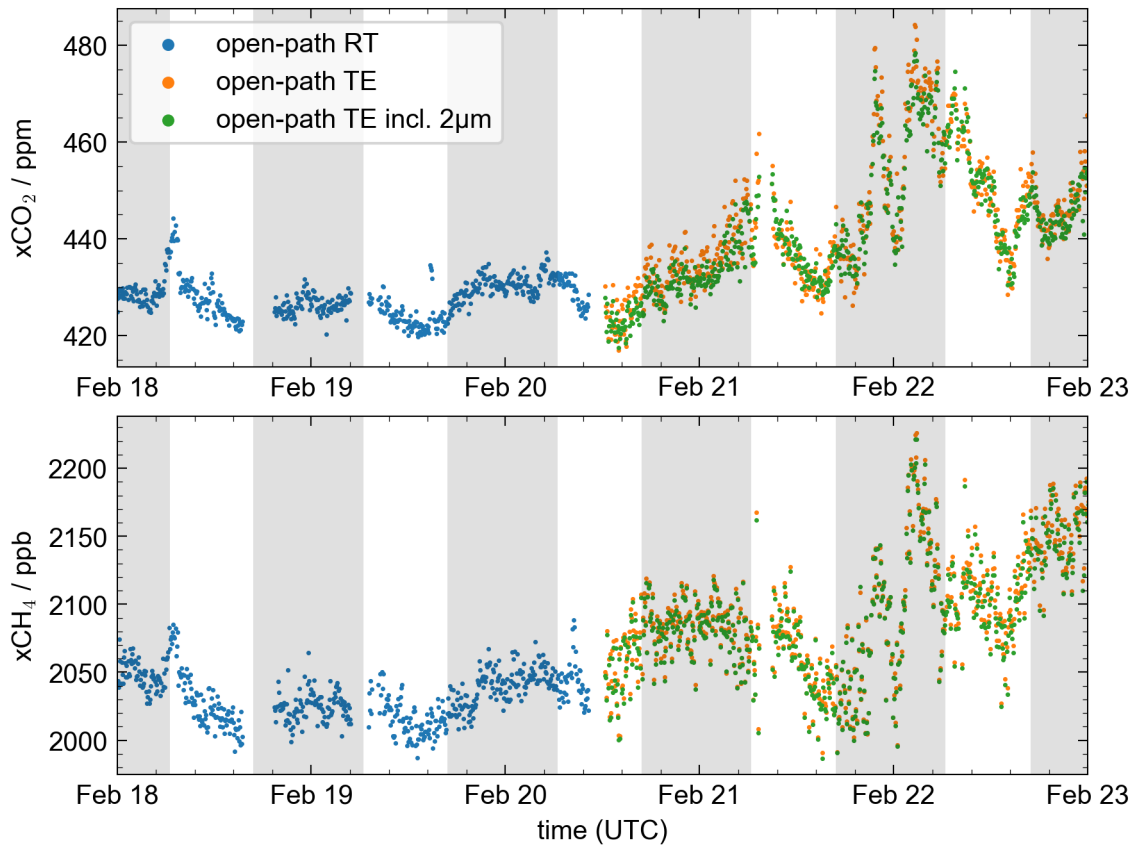


Figure 5.4: As Figure 5.3, but a zoom in on the transition period from the RT to the TE detector. It is clearly visible, that for $x\text{CO}_2$ the scatter for the RT detector is lowest, and the scatter for the TE detector using the $2\ \mu\text{m}$ windows is better than not using it. For $x\text{CH}_4$, the RT detector again shows the best performance, while the TE detector results just show a minor offset between the two evaluations.

for the RT detector, and once using all spectral windows. Looking at Figure 5.3 reveals the following: For the TE detector, the scatter for $x\text{CO}_2$ is significantly lower when including the windows 1 to 2 to take advantage of the strong CO_2 absorption bands around $2\ \mu\text{m}$. Since these windows do not include information on CH_4 , there is negligible difference for $x\text{CH}_4$ between the two retrievals. When further taking a detailed look into the transition region on 2023-02-20 (Figure 5.4), it becomes apparent, that the scatter for both gases is lower for the measurements with the RT detector.

A quantitative analysis of the precision for the full comparison period, yields the results in Table 5.3. They confirm the initial visual assessment from the time-series, with better precision for the RT detector compared to the TE detector, and better precision for $x\text{CO}_2$ when including the $2\ \mu\text{m}$ windows for the TE detector compared to omitting them. In general, the RT detector shows roughly a factor of

Table 5.3: Precision of 5 min gas measurements for RT and TE detector.

	RT detector	TE detector (only 1.6 μm band)	TE detector (incl. 2 μm band)
xCO ₂	1.4 ppm (0.32 %)	3.5 ppm (0.80 %)	2.9 ppm (0.65 %)
xCH ₄	8.3 ppb (0.40 %)	19.2 ppb (0.92 %)	19.2 ppb (0.92 %)
O ₂	0.36 %	0.80 %	0.80 %
H ₂ O	0.57 %	1.5 %	0.86 %

2.5 better performance in comparison to the TE detector with the same retrieval. For xCO₂, the accessibility of the 2 μm windows for the TE detector reduces this advantage to a factor of 2. Including the 2 μm windows also brings an improvement for the retrieved H₂O CD, but this is hardly relevant. If more precise information on H₂O is required, it is always easy to fine tune retrieval windows to include more water vapor absorption lines. While this result shows, that the RT detector is the superior choice when the interest lies solely on xCO₂ and xCH₄, the majority of the timeseries uses the TE detector. This enables the evaluation of additional species, which are only available in the extended spectral range, in the future and allows to analyze the quality of spectral databases in the 2 μm band of CO₂.

5.3 Comparison of Different Modes of Operation

All measurements presented from here on are recorded with the TE detector. In this section I analyze the performance of the different modes of operation (Table 4.1) with respect to quality of spectra and fit, averaging times and retrieved target gas information.

5.3.1 Spectrum and Fit Quality

We recall that Figure 4.7 shows a typical spectrum measured in benchmark mode. For a lower temporal resolution (one minute mode), the spectra look similar, just with increased noise. Because of that I will omit their discussion in the context of spectrum and fit quality. For a higher spectral resolution and similar measuring time (high resolution mode), the spectrum shows higher noise, but notably deeper absorption structures (Figure 5.5). This is particularly visible in the O₂ band at 1.3 μm and the CO₂ bands at 1.6 μm . Further, the saturation of the absorption lines in both 2 μm CO₂ bands is somewhat visible.

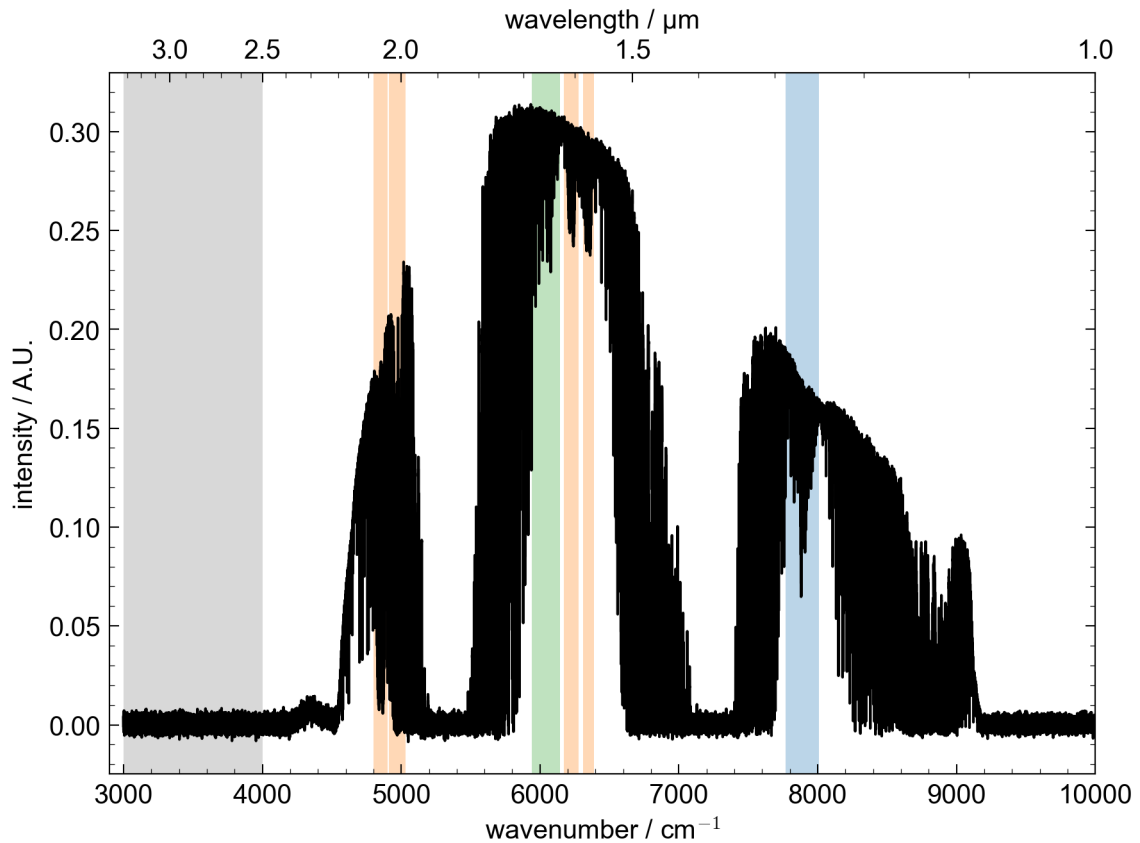


Figure 5.5: Typical example of a spectrum measured in high resolution mode (resolution of 0.11 cm^{-1}). Colored bands as in example spectrum for benchmark mode (Figure 4.7). In comparison to benchmark mode, the deeper absorption lines are clearly visible, especially in the CO_2 bands at $1.6 \text{ }\mu\text{m}$ and the O_2 band at $1.3 \text{ }\mu\text{m}$. The spectrum also shows higher noise.

For a more detailed analysis it is helpful to look at the spectrum and fit residuals in the absorption windows. Figure 5.6 shows these for measurements in benchmark mode and Figure 5.7 shows these for measurements in high resolution mode. The plots include a residual for a single measurement and one which is averaged over a large number of measurements and basically free of noise. The latter provides an approximation for the systematic residual. The following observations are the same for both types of measurements: The CO_2 bands in window 1 and 2 show a significant systematic residual, especially when compared to the absorption bands in the other windows. In windows where the systematic residual does not contribute significantly, the residual is dominated by noise and a brief analysis reveals the noise to be gaussian/white and matching the estimation from the noise band. In windows where the systematic residual does contribute significantly, a similar analysis is possible by subtracting the averaged

residual from a single one and performing the same analysis. This shows that also for these windows the noise beyond the systematic residual is well described by the noise estimation and that the averaged residual is a reasonable description of the systematic contribution, even for single spectra. Where the systematic residual does contribute significantly, it is typically aligned with spectral structures like absorption lines. Window 2 shows a underlying broad band structure aligned with the CO₂ P and R branch, which hints at an insufficient description of the continuum absorption.

When looking for the cause of the residuals, it becomes clear that the high resolution measurements provide a significant improvement over the benchmark mode. With a resolution of 0.11 cm⁻¹, the ILS is significantly narrower than a typical absorption line at a pressure of 10⁵ Pa, which is around 0.2 cm⁻¹ to 0.3 cm⁻¹. Especially in regions, where multiple absorption bands and lines of different species overlap (multiple lines within 1 cm⁻¹), the higher spectral resolution is necessary to attribute the spectral errors. Based on Figure 5.7, we can judge the quality of the spectral model (meaning forward model and cross-sections) for the different windows. It is apparent that windows 3 to 6 are described well, with only a few single lines showing systematic errors. Those lines usually correspond to H₂O. A notable exception of this is the CH₄ Q branch at 6000 cm⁻¹ in window 3, which also experiences systematic deviations between fit and measurement. Window 1 shows some systematics in the CO₂ lines, with a couple of strongly deviating H₂O lines. Window 2 shows the worst spectral description, with many strongly deviating H₂O lines and systematic errors in the CO₂ description, including a broad band continuum structure.

5.3.2 Time Resolution

In general, measuring in higher temporal resolution is obviously desirable when looking at time dependent signals and especially if this variability is of interest. But if not enough information on the signal is gathered in a short amount of time, the measurement is dominated by noise, and the actual signal variability is not visible. A common tool in the geoscience community to estimate how much signal averaging is beneficial to decrease the measurement noise, but not to average real signal variability, are Allan deviations, as described in Section 4.4.

I applied this to the measurements in one-minute mode, which have the highest temporal resolution and thus can inform also on averaging times below 5 min. Figure 5.8 shows the Allan deviations for the retrieved open-path values of xCO₂ and xCH₄, as well as for the in-situ data. The open-path data initially follows

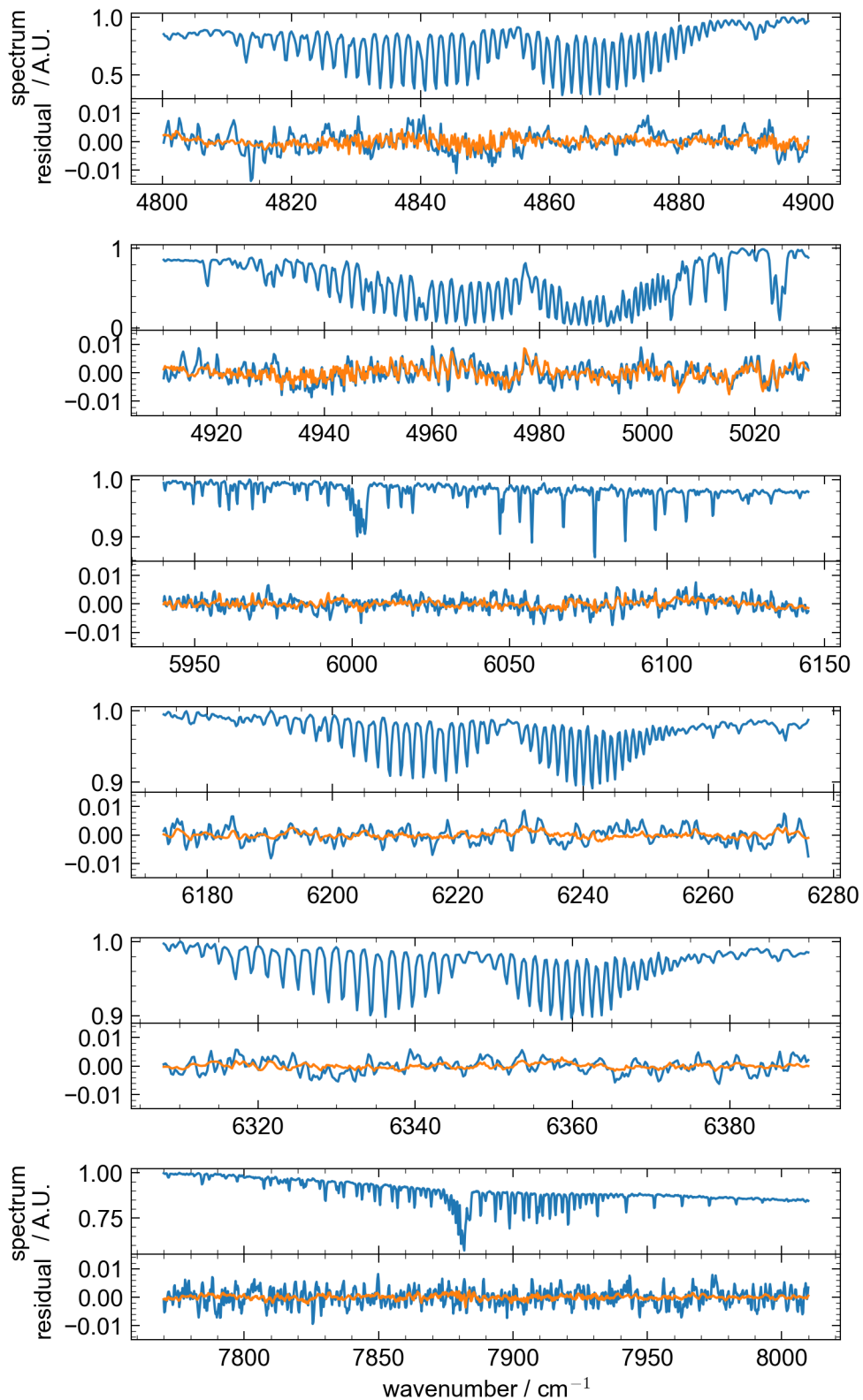


Figure 5.6: Spectrum and fit residual for single measurement (blue) and averaged (orange), for each fit window. Recorded in benchmark mode (resolution of 0.55 cm^{-1}).

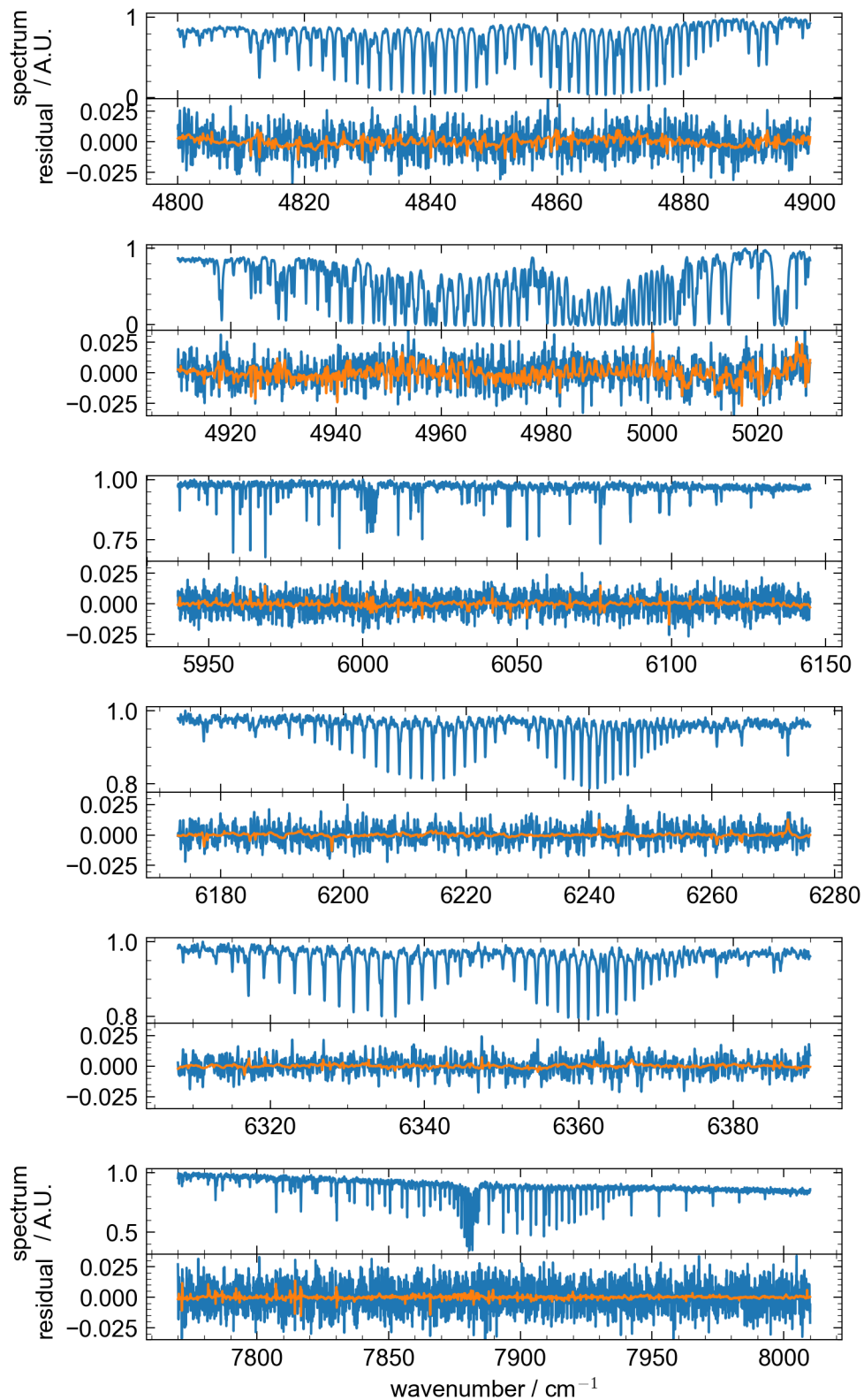


Figure 5.7: Spectrum and fit residual for single measurement (blue) and averaged (orange), for each fit window. Recorded in high resolution mode (resolution of 0.11 cm^{-1}).

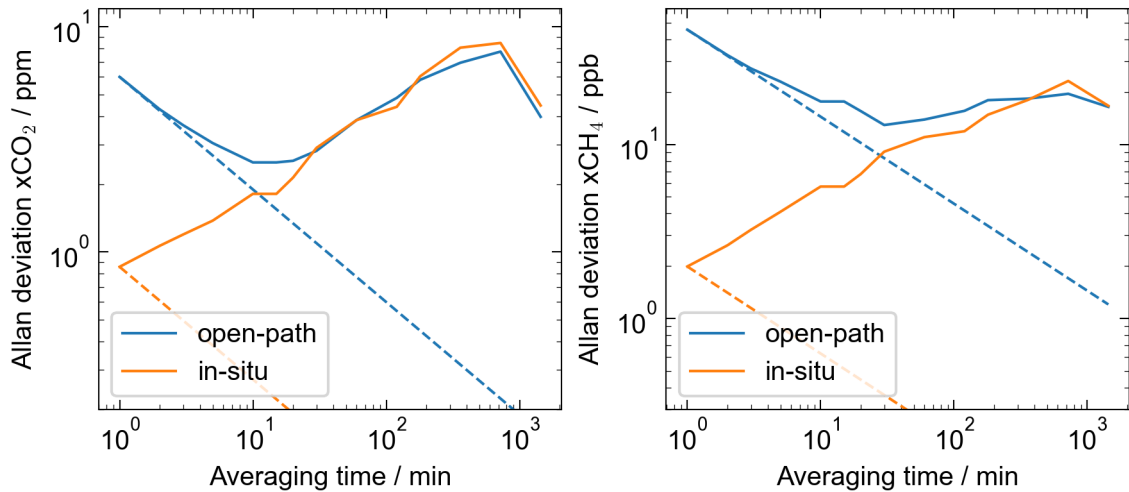


Figure 5.8: Allan deviations for $x\text{CO}_2$ (left) and $x\text{CH}_4$ (right), each for open-path in one minute mode (blue) and in-situ measurements (orange). Dashed lines show the statistical extrapolation (decreasing with the square root of time) starting from the first value.

the statistical extrapolation, showing that noise dominates in this region and averaging just increases the measurement precision. Around an averaging time of 5 min, the open-path measurements start to deviate from this statistical extrapolation. This shows, that real world variability and measurement precision are of the same magnitude there. A comparison with the in-situ instrument yield three important observations: First, the in-situ instruments has in general a significantly higher 1 min precision then the open-path system and is generally limited by real variability. Secondly, for long averaging times of 30 min to 100 min, the Allan deviations of in-situ and open-path measurement are nearly identical. And finally, for averaging times of 24 h, the variability decreases again. This shows, that the sensitivities to fluctuations on the scale of hours and above is similar for both measurement systems. Further, the drop at an averaging time of 24 h shows, that a large part of the variability is driven by the diurnal cycle and is smoothed out when averaging over a full day. Judging from Figure 5.8, an averaging time of 5 min is a good compromise between averaging out noise and the unwanted side effect of smoothing out real signal. If any relevant improvement to the SNR is achieved, reducing the averaging time to somewhere from 1 min to 3 min is advisable.

5.3.3 Direct Comparison of Target Gas Performance

While both high spectral and high temporal resolution are desirable, they usually come with trade-offs. Measuring at higher spectral resolution decreases SNR for basically any spectroscopic method. For FTIR, assuming constant light throughput, the SNR is directly proportional to the resolution, meaning that an improvement in spectral resolution by a factor of 5 leads to 5 times more noise. If however the spectral features under investigation are weak lines, which are significantly more narrow than the ILS, the feature strength (i.e. the line depth) increases also by the same factor. In these cases the SNR might be worse, but the information retrieved from the spectrum would not be more noisy. However, many target gas absorption lines can not be considered weak, as is apparent from Figure 5.7, especially not the CO₂ lines in the 2 μm windows. Also most relevant absorption lines are 0.2 cm⁻¹ to 0.3 cm⁻¹ wide at a pressure of 10⁵ Pa. This means that their feature strength does not increase linearly once the spectral resolution is of comparable magnitude. In both of these cases, a measurement of high spectral resolution yields more noisy information on the target gases, than its lesser resolved counterpart. The only exception to this are cases, where the low resolution is insufficient to disentangle information, for example if two close absorption lines of different species can not be resolved. If the spectral features are oversampled, an increase in resolution increases the noise linearly, while only adding linearly more datapoints to an otherwise unmodified spectral feature. Since averaging over n more datapoints only reduces the noise of the retrieved information by $1/\sqrt{n}$, the resulting information is more noisy by a factor of \sqrt{n} . For measurements of high temporal resolution the trade-offs are less obvious, since it is simply possible to average the higher resolved results in post processing. So if data storage or processing power is not a primary concern, it seems always beneficial to measure in higher temporal resolution. But a typical FTIR spectrometer experiences a certain fixed measurement overhead, reducing the duty cycle efficiency for many short measurements in comparison to fewer but longer measurements. This is also visible in Table 4.1, where the number of scans in one repetition period is slightly worse for the one minute mode.

I estimated the 5 min target gas precisions for all three measurement modes from the following timespans: from 2023-05-25 to 2023-07-12 for the benchmark mode, from 2023-04-01 to 2023-05-01 for the one minute mode, and from 2023-07-13 to 2023-09-15 for the high resolution mode. The results are listed in Table 5.4. The benchmark mode shows overall the best performance. The high resolution mode shows the worst performance, with a roughly 60 % worse performance for

Table 5.4: Precision of gas measurements for the different operation modes, after resampling on a 5 min grid.

	benchmark mode	one minute mode	high resolution mode
xCO ₂	2.1 ppm (0.49 %)	2.7 ppm (0.61 %)	3.3 ppm (0.78 %)
xCH ₄	15 ppb (0.73 %)	20 ppb (0.97 %)	25 ppb (1.2 %)
O ₂	0.67 %	0.77 %	1.1 %
H ₂ O	1.1 %	1.1 %	1.1 %

xCO₂ and xCH₄ compared to the benchmark mode. This is expected from reasoning above, since in this mode the lines are oversampled by a factor of 2 to 3, which corresponds to 30 % to 70 % more target gas noise. The one minute mode shows a roughly 30 % worse performance for xCO₂ and xCH₄ compared to the benchmark mode. This is worse than expected from the less than 10 % worse duty cycle. A possible explanation for this is a higher actual variability of xCO₂ and xCH₄ during the respective evaluation period, since we just saw that 5 min measurements already show influence from real variability (Figure 5.8). Indeed, the precision of the 5 min averaged in-situ values show a xCO₂ (xCH₄) variability of 1.0 ppm (3.3 ppb) and 1.4 ppm (5.1 ppb) in the respective timeframes for the benchmark mode and one minute mode. This comparison assumes that the measured in-situ values are a good approximation for the real variability measured by the open-path system. The Allan deviations discussed earlier are an indicator for this. Assuming this for now, it at least partially explains the worse than expected performance of the one minute mode. A notable exception to all of this are the retrieved values for H₂O, which show the same precision for all three modes. While the exact cause of this is unclear, it might be a mixture of the high variability of water vapor and the poor quality of the available spectral information.

5.4 Optimal Operation Configurations

The observatory's performances in the different modes of operations and with the different detectors allows to draw conclusions on optimal configurations depending on the goal of the measurements.

First, the measurements using the TE detector with a resolution of 0.55 cm⁻¹ and an averaging time of 5 min provide a stable and flexible baseline. They provide good precisions of 2.1 ppm (0.49 %) for xCO₂ and of 15 ppb (0.73 %) for xCH₄. They also offer a wide spectral range and thus more possibilities to later enhance

the scope of an analysis to other target gases. An example of such a species is CO, which is only accessible at wavelengths longer than 1.7 μm .

Second, if just the $x\text{CO}_2$ and $x\text{CH}_4$ are the primary measurement targets, the RT detector provides a better performance: 1.4 ppm (0.32 %) for $x\text{CO}_2$ and 8.3 ppb (0.40 %) for $x\text{CH}_4$. A spectral resolution around 0.55 cm^{-1} should be a good choice, since the measurements with the TE detector showed the best target gas precisions at these settings. This behavior of the TE detector at different spectral and temporal resolutions should be transferable to the RT detector. The optimal averaging time should be smaller than the 5 min of the setup with the TE detector. A proper estimation requires an analysis like the one in Figure 5.8, but it is possible to estimate a good averaging time for the setup with the RT detector from the precisions for $x\text{CO}_2$ and $x\text{CH}_4$. Since the RT detector shows a better precision by a factor of 1.5 to 1.8, the measurement time can be reduced by the square of that in a first approximation. Since the real variability also reduces for a shorter averaging time, an averaging time of 2 min to 3 min should be a good approximation for an open-path setup based on the RT detector and focused on the $x\text{CO}_2$ and $x\text{CH}_4$ performance. Such a deployment of the RT detector should include two minor modifications to the setup: an improved shielding against EMI and the inclusion of a long pass filter at around 1.1 μm like in the TE detector optics.

Third, if the main purpose of the measurements is the test of spectroscopic parameters, a spectral resolution in the range of 0.11 cm^{-1} is advisable. This provides fully resolved spectral residuals with only a marginal influence of the ILS, while still providing acceptable target gas performance (3.3 ppm (0.78 %) for $x\text{CO}_2$ and 25 ppb (1.2 %) for $x\text{CH}_4$, using the TE detector). Using the RT detector over the TE detector is in theory preferred, but since I consider the CO_2 absorption bands at 2 μm the most interesting target for such an analysis, the TE detector might be required. The current dataset provides already several weeks of measurements in this configuration.

There are a few possibilities for general improvements of the setup, which apply more or less to all modes of operations and which can alter their ideal parameters, especially the averaging time. All of these possibilities are related to an improvement of the spectral SNR performance. The first and most obvious one is an enhanced light throughput. The geometrically most limiting optical element is currently the receiving fiber. Any changes there necessarily need to include a full analysis of the telescope system, similar to Merten et al. (2011). Possible improvements are difficult to estimate and would most likely require a substantial overhaul of and investment in the telescope system. Nonetheless, there are a few

other points where it is possible to enhance the light throughput anyways: First are the fiber mounts, where the light is coupled from the spectrometer to the fiber and where the fiber is coupled to the telescope. Both of these mounts necessarily obstruct the light path, but there is room for optimization on the order of tens of percent each, using custom machined mounts. The second possibility is an increase of the reflector area. This could provide a SNR improvement of a couple percent. Last is a fine tuned optimization of the spectral resolution. As mentioned before, for weak spectral lines measured at low resolution, the information content is theoretically independent of the exact resolution they are measured at. But in reality many relevant absorption lines are not weak and the choice of resolution can also alter the duty cycle of the instrument. Any improvements rely heavily on the details of the spectrometer at hand and the spectral features under investigation. Hence, it is advisable to apply an empirical approach for these cases.

5.5 Open-Path Measurements of Carbon Dioxide and Methane

In this section, I discuss technical results and details of the long term deployment of the TE detector. This covers retrieval settings, the calculation of dry mole fractions, and how ILS fluctuations caused by varying light throughput contributes to noise on the retrieved quantities. Some of the results presented here are already published in Schmitt et al. (2023).

5.5.1 Path Average Temperature and Line Mixing

Already Griffith et al. (2018) found that fitting a path averaged temperature yields better results than fixing the temperature to the values measured by the weather station at the IUP. They also found substantial differences between their fitted temperature and the weather station data, with the fitted temperature being low biased by 2 K to 6 K. I performed a similar experiment with my data by once fixing the temperature to the weather station results and once fitting it in the retrieval. Additionally, I included an evaluation where the temperature is fitted and the cross-sections for CO₂ in the 2 μm band include line-mixing (as described in Subsection 4.2.1). Figure 5.9 shows the results in a short comparison timeframe.

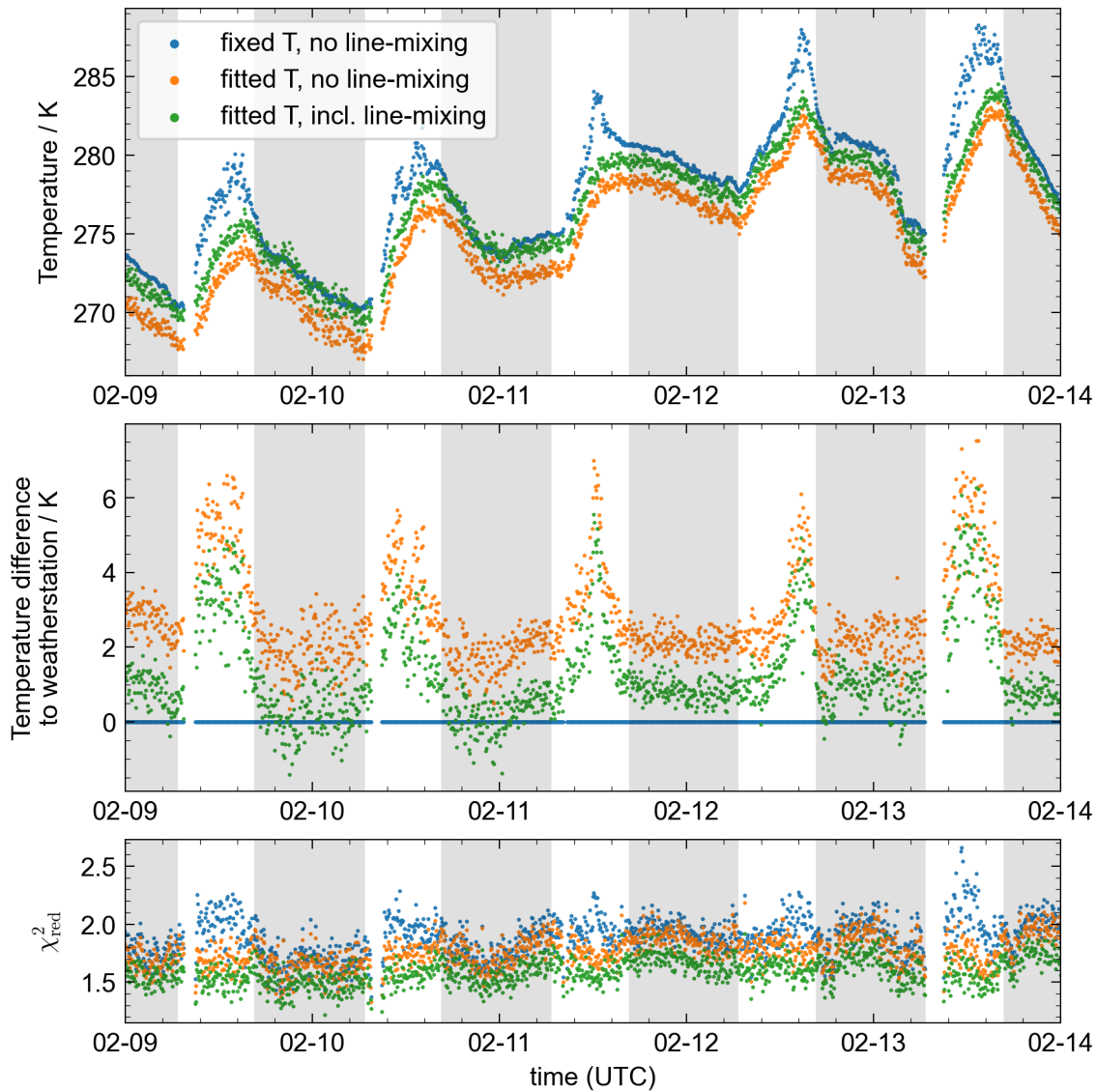


Figure 5.9: Comparison of fixed temperature and fitted temperature for a short comparison timeseries. The fixed temperature is the temperature measured by the weather station. The fixed temperature shows large deviations from the other two curves and spikes in the afternoon. The χ_{red}^2 values of the forward model fit show, that these temperature spikes are most likely not a good description for the path average temperature. But the fitted temperature matches the measured temperature at night within 1 K, if line-mixing is included. Without line-mixing, this difference is at about 3 K. χ_{red}^2 is minimal for a fitted temperature including line-mixing.

The most notable difference is the one between the weather station temperature and the fitted path average temperature during daytime. During daytime, the weather station temperature mostly shows significantly higher results and sometimes rather abrupt structures (for example on 2023-02-11, around midday). This is likely not a realistic description of the air column temperature and the smoother timeline of the retrieved temperatures seem more realistic in this regard. The spikes in χ_{red}^2 , when the weather station temperature deviates most, are a further indication for this. A possible explanation for this behavior of the weather station temperature sensor would be insufficient shielding against radiation or an other effect of local heating close to the weather station due to solar radiation, als also Griffith et al. (2018) concluded.

The second important observations are the rather constant differences during night times. Here, all three temperature curves follow mostly the same trend, but show different offsets: The measured temperature is typically 2 K to 3 K above the fitted temperature without line-mixing and 1 K above the fitted temperature with line-mixing. In absence of a strong local heating source like solar radiation, a temperature difference of 2 K to 3 K seems unlikely and the 1 K far more realistic. Also, the overall quality of the fit (using χ_{red}^2 as a criterion), improves significantly when fitting the temperature, while including line-mixing effects.

Figure 5.10 shows the spectroscopic effects behind this. It shows the spectrum and the fit residuals for the respective retrieval configurations for the $2\ \mu\text{m}$ CO_2 band. The effects are clearest in the stronger of the two absorption bands at $4930\ \text{cm}^{-1}$ to $5020\ \text{cm}^{-1}$. For lower temperatures, the states with lower rotational quantum number j in the center of the window are higher populated, while the states with high j at the wings of the band are less populated. If the fit overestimates the temperature, we get a residual like for the fixed temperature case (Figure 5.10, blue curve): The fit overestimates the line strengths in the wings ($4940\ \text{cm}^{-1}$ and $5000\ \text{cm}^{-1}$) and underestimates the line strengths in the center ($4965\ \text{cm}^{-1}$ and $4985\ \text{cm}^{-1}$). But also the residual for a fitted temperature (orange curve) still shows significant systematic structures concerning the intensity distribution within the band. Including line-mixing in the cross sections (green curve) yields a substantial additional improvement here and removes a substantial part of the broad band structure in the residuum. So both the resulting temperature curves and the quality of the spectral fit indicate, that a fitted temperature, is the best description for the actual temperature along the absorption path, as long as line-mixing is included in the cross-sections.

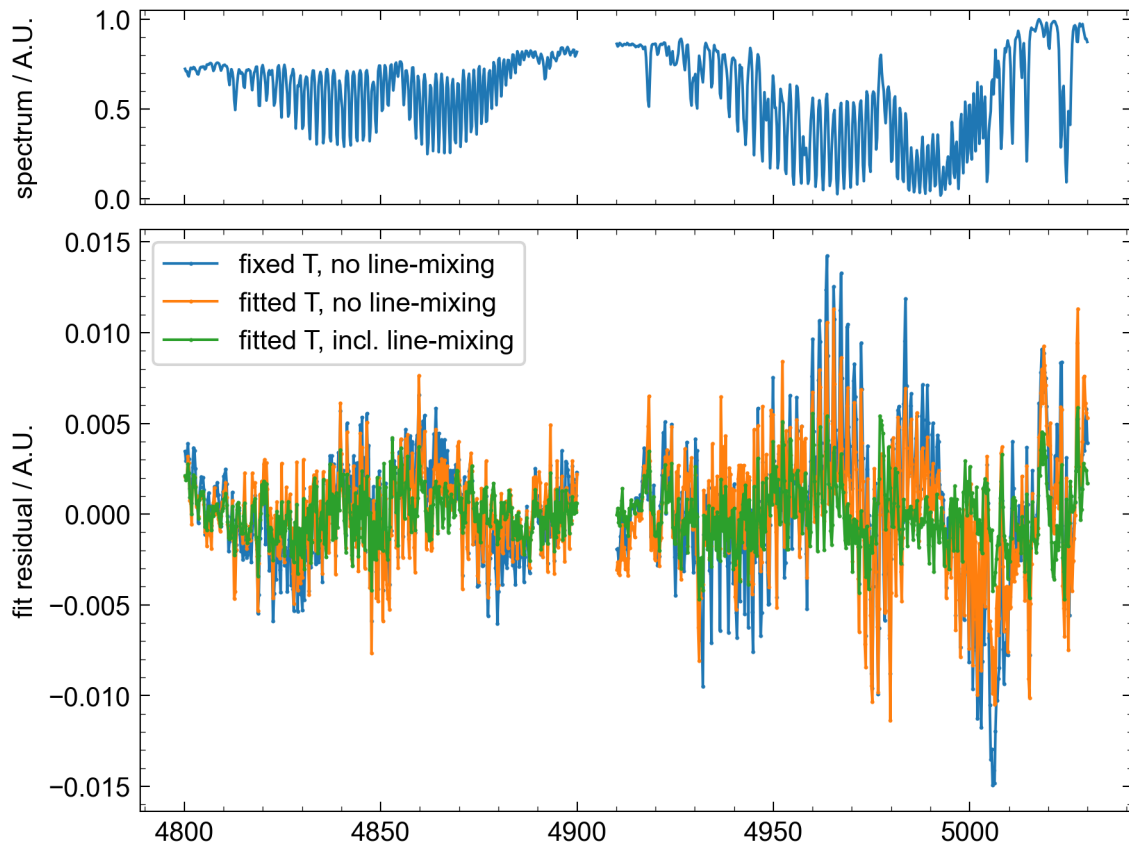


Figure 5.10: Fit residuals for fixed and fitted temperature, with and without line-mixing. Plotted are the averaged measured spectrum and the averaged residuals for the three retrieval configurations. They are averaged over the comparison time frame from Figure 5.9. The fitted temperature is an improvement over the fixed temperature retrievals. But including line-mixing achieves the most obvious improvements and greatly reduces the systematic structures especially in the range of 4930 cm^{-1} to 5020 cm^{-1} .

Table 5.5: Relative precisions of measured total CDs and dry air mole fractions for retrieved species. xQ is the dry air mole fraction obtained by dividing through the measured O_2 column (Equation 4.2). $\hat{x}Q$ is the dry air mole fraction obtained by calculating the dry total air column from temperature, pressure and the measured water content (Equation 4.3). O_2 (calc.) is the O_2 amount calculated this way.

species	CDs / %	dry mixing ratios / %	
		xQ	$\hat{x}Q$
CO_2	0.78	0.64	0.82
CH_4	1.04	0.99	1.07
O_2	0.77	—	—
O_2 (calc.)	0.10	—	—

5.5.2 Mole Fractions

In Section 4.3, I discussed two possible ways to calculate dry air mole fractions from the open-path data: Either using the measured O_2 CD as a proxy for the dry air column (denoted as xQ) or calculating the dry air column from meteorological data and the retrieved water amount (denoted as $\hat{x}Q$). Table 5.5 shows a comparison of the achieved mixing ratio precisions for these two methods. A first glance already tells us, that mixing ratios calculated with the measured O_2 CD perform better. A further look reveals a couple of interesting details: First, dry mixing ratios calculated with the measured O_2 CD show a better precision than the target gas CD used to calculate them, and, in case of CO_2 , than the O_2 CD. Second, the precision of calculated dry air CD (or for better comparison of a calculated O_2 CD) is nearly an order of magnitude better than the measured O_2 CD. This is expected, since pressure and temperature are measured to a high precision. Finally, the dry mixing ratios calculated from this calculated air mass show the expected precision, which closely follows the precision of the respective target gas CD, but slightly worse.

It is obvious that dividing a target gas CD by the measured O_2 CD should not lead to better precisions than those of the two CDs; at least if both of them are uncorrelated. This indicates, that the noise on spectrum retrieved CDs includes a component, which is correlated between them. In the following chapter, I discuss a possible mechanism behind this correlation.

5.5.3 ILS Fluctuations

The ILS is the one obvious influence which correlates all CDs retrieved from one spectrum. If the ILS is more narrow and peaked, a smaller amount of trace gas results in sufficiently deep absorption lines to fit the measured spectrum. Contrary, if the ILS is broader and less peaked, a larger amount of trace gas is necessary to produce sufficiently deep absorption lines. Assuming such a correlation, a more narrow ILS would result in smaller amounts of measured CO₂, CH₄, and O₂, but the quotients of CO₂ and CH₄ with O₂ respectively would vary less. Thus, the mixing ratios calculated by taking the ratio with the O₂ CD could vary less than the mixing ratios calculated from meteorological parameters.

To test this hypothesis, I retrieve a set of spectra with a reference ILS and a slightly modified ILS. More precisely, I add a minor variation to the modulation efficiency, the parameter which governs how narrow the ILS is. I then calculate the sensitivities of different retrieved quantities. To check the influence of the resolution, I perform this analysis for spectra measured in benchmark mode and for spectra measured in high resolution mode. Table 5.6 shows the results of this sensitivity analysis. I compare the sensitivities between the two modes once with a fixed variation for both resolutions, to get a direct indication of the effect of higher resolution on that matter. Additionally, I estimate a typical ILS variation from the standard deviation of the ILS retrieval results (Subsection 4.2.3), which is larger for the high resolution mode. I use these estimations for typical modulation efficiency variations to scale the sensitivities for each measurement mode and get a more realistic “in field” comparison of the sensitivity.

The results in Table 5.6 support the hypothesis, that a variation in the ILS generates correlated deviations in the retrieved trace gases, which the partially cancel out when taking ratios. Using the low resolution measurements at a fixed modulation efficiency variation as an example we see this clearly: An assumed sharper ILS leads to lower retrieved values of CO₂ and O₂. Their measured CDs change by -0.30% and -0.22% respectively. The ratio of the two changes only by -0.08% . The analysis also supports the assumption, that the use of a sharper ILS in the retrieval leads in general to lower retrieved CDs. But since the sensitivities of the different gas CDs to the ILS variation differ, their ratios still show some sensitivity and vary in both directions. We further see, that calculating the dry air CD from meteorological parameters is nearly insensitive to ILS variations (0.03% for a calculated O₂ CD). This then results in a high sensitivity of mixing ratios calculated with this dry air mass (-0.33% for $\hat{x}\text{CO}_2$). These general observations are true for low resolution and high resolution measurements.

Table 5.6: Sensitivity of retrieved trace gas results on ILS modulation efficiency. Relative changes in the retrieved trace gas quantities as a result of a changed ILS in the retrieval. I varied the modulation efficiency of the ILS, either by a fixed value ($\Delta = 0.01$) or by a measurement mode typical variation. “Low resolution” refers to the benchmark mode and “high resolution” refers to the high resolution mode.

quantity	fixed variation ($\Delta = 0.01$)		respective typical variation	
	low resolution	high resolution	low resolution ($\Delta = 0.0175$)	high resolution ($\Delta = 0.034$)
CO ₂	-0.30 %	-0.07 %	-0.52 %	-0.24 %
xCO ₂	-0.08 %	0.05 %	-0.14 %	0.17 %
\hat{x} CO ₂	-0.33 %	-0.09 %	-0.58 %	-0.32 %
CH ₄	-0.17 %	-0.09 %	-0.30 %	-0.29 %
xCH ₄	0.04 %	0.04 %	0.08 %	0.12 %
\hat{x} CH ₄	-0.21 %	-0.11 %	-0.36 %	-0.37 %
O ₂	-0.22 %	-0.12 %	-0.38 %	-0.41 %
O ₂ (calc.)	0.03 %	0.02 %	0.06 %	0.08 %

Comparing the two resolution modes for a fixed variation shows a smaller influence of the ILS variation on the retrieved gas CDs for a higher resolution. This also fits our understanding, since for a higher resolution the measured shape of a transition line is less dominated by the ILS and more of its actual own shape. However, when retrieving the ILS from a set of consecutive spectra, the typical ILS variation is larger for high resolution measurements. Taking this into account, the performance of both resolution modes becomes comparable in magnitude.

All of this shows, that a variation of the modulation efficiency of the ILS indeed does generate a correlated variation in retrieved gas CDs. If the modulation efficiency is subject to some kind of noise, this results in a corresponding noise on the retrieved CDs, but this noise partially cancels for their quotients and thus for the calculated mixing ratios. But this still leaves the question open, what the mechanism behind such a noise on the modulation efficiency could be.

We can converge to an explanation of the mechanism behind these ILS fluctuations by looking again at the concept of the modulation efficiency. The modulation efficiency describes the variation of modulation strength of the interferometer as a function of OPD, as explained in Section 3.7. A reason for this variation can be a variation in light throughput through the interferometer. In the context of characterizing the ILS of a laboratory instrument, we typically think of this modulation variation as a instrument specific function depending on the OPD, which is then of course constant in time. But when now looking at a faint light

source through 3 km turbulent atmosphere, refraction¹ add a noise on the light throughput over time and thus on the IFG, which is also measured over time. This then results in a variable light throughput along the OPD for a measured IFG. The instrument thus records all spectra with a somewhat different effective ILS. Later, the spectra are processed using a constant ILS for all of them, so each spectrum is analyzed with a slightly wrong ILS. This is similar, to the above sensitivity analysis. Averaging the IFG over multiple scans of course reduces this effect of randomly varying light throughput, since it is not coherent between the scans. This also corresponds to the larger ILS variation for the high resolution measurements, because those measurements average the IFG over fewer scans, since each scan takes more time.

These fluctuations of total light intensity reaching the detector are similar to those encountered in sun-viewing measurements. There, the typical solution is a so-called DC corrections, which uses the low frequency components of the detector signal as a proxy for these fluctuations. However, this is not necessarily applicable to open-path measurements, since contrary to sun-viewing measurements, in-beam scattering can contribute significantly to the overall light intensity on the detector. Even though this scattered light does not contribute spectral information (since it is not modulated in the interferometer, as explained in Subsection 4.1.2), it contributes a constant or low frequency offset. As a result, this offset can no longer serve as a direct proxy for the amount of light transmitted along the light path. How a similar technique can be applied to open-path measurements and how much it improves measured target gas quantities requires further investigation.

5.6 Comparison of Open-Path and In-Situ Measurements

In this section, I present the timeseries for $x\text{CO}_2$ and $x\text{CH}_4$ from the long term deployment of the TE detector and the results from the side-by-side comparison with the in-situ analyzer. The timeseries up to 2023-07-11 and some of the corresponding results are published in Schmitt et al. (2023).

Figure 5.11 shows the measurements of $x\text{CO}_2$ and $x\text{CH}_4$ from 2023-02-08 until 2023-10-09, each for the open-path and the in-situ instrument. The measurements are averaged on a grid of 5 min. The plotted open-path measurements

¹similar to astronomical seeing

exclude low signal measurements (for example due to fog or dense rain). The open-path instrument achieves a coverage of more than 75 % on the 5 min grid over the full period. In months where the spectrometer was fully dedicated to the open-path measurements, the coverage is up to 90 %. A first look at the timeseries reveals a good agreement between open-path and in-situ data. For example, both records show a decrease of the background $x\text{CO}_2$ from mid April onwards. This is expected and results from seasonal enhanced biosphere activity in the northern hemisphere. On top of this trend, the diurnal cycle dominates the signal and is also present in both records. Figure 5.12 provides a closer look on the diurnal cycle for ten consecutive days. The diurnal cycle typically shows a steadily increasing nighttime enhancement, followed by a drop in the morning, a few hours after sunrise. The predominant driver for this is the height of the planetary boundary layer, which is typically low during the nights and the emitted CO_2 accumulates. The boundary layer height increases with the onset of solar heating, leading to more efficient mixing and a resulting drop in $x\text{CO}_2$. The onset of solar heating is typically a few hours after sunrise due to the hills in the east of Heidelberg. Both records also agree well for $x\text{CH}_4$, but the timeseries shows a less clear structure and diurnal cycle than for $x\text{CO}_2$. The timeseries show visually more scatter in the open-path data for both gases, which matches earlier results in this chapter, especially in Figure 5.8 for an averaging time of 5 min. The average open-path measurement precisions for the full dataset gridded to 5 min are 2.8 ppm (0.64 %) for $x\text{CO}_2$ and 20 ppb (0.99 %) for $x\text{CH}_4$.

5.6.1 Diurnal Cycle

The choice of time zone for an analysis of the diurnal cycle is not straight forward, since there is a switch to daylight savings time (from UTC+1 to UTC+2) on 2023-03-26. Because of this, the difference between local time and UTC is no constant offset. Anthropogenically driven signals like rush hour should follow local time. However, for meteorological signals, like the build up and dispersion of the boundary layer enhancement, the actual sunrise and sunset are relevant. Since those significantly shift throughout half a year, this information is washed out anyways. Because of this, and because we are interested in anthropogenic signals, I decided to look at the diurnal cycle in reference to the local time. Figure 5.13 shows the diurnal cycle of $x\text{CO}_2$ averaged for weekends and weekdays and for both instruments. It further shows the differences between weekends and weekdays, as well as between the instruments. The general shape of the diurnal cycle follows the observations from the examples in Figure 5.12 as expected: A

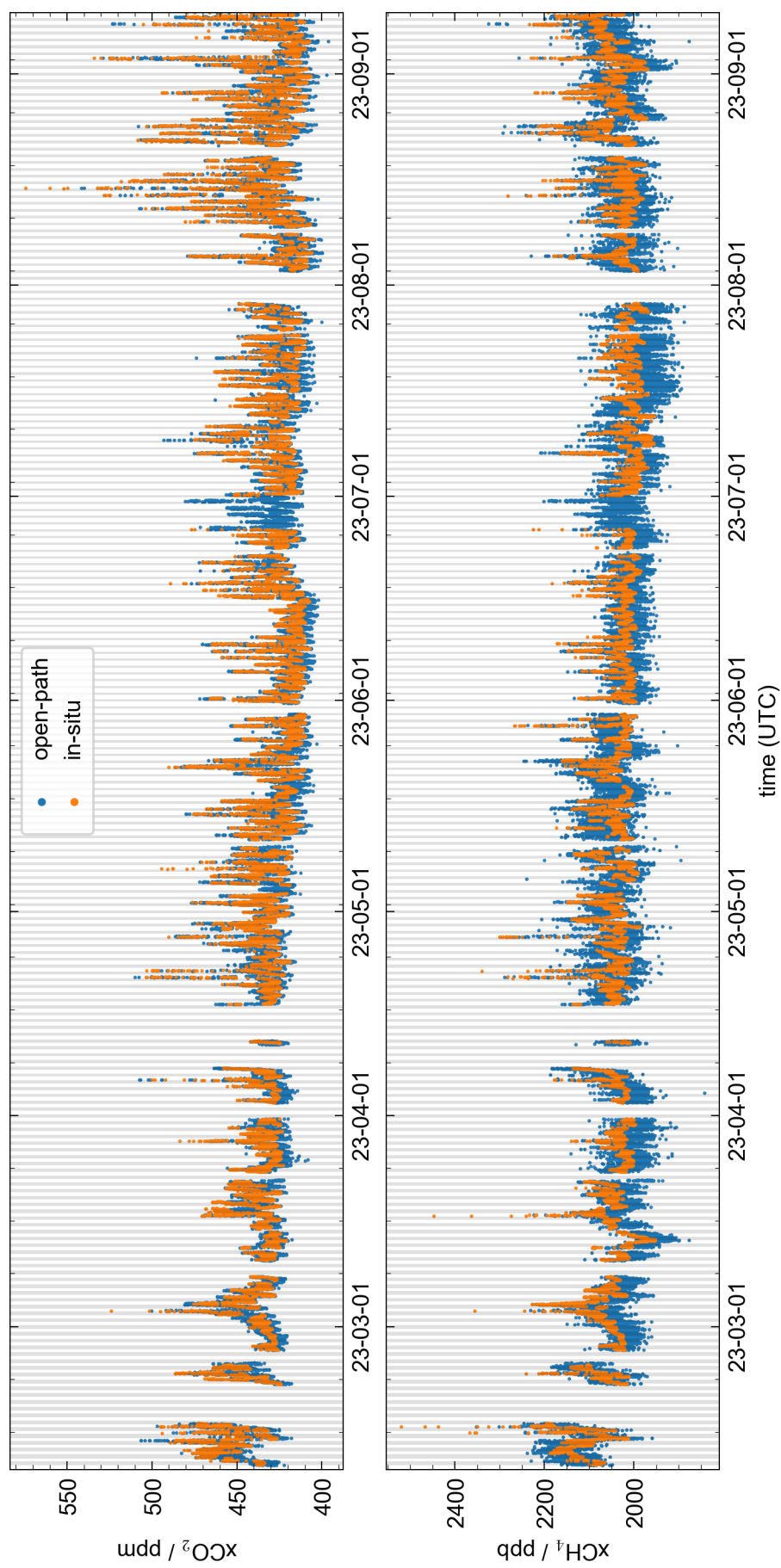


Figure 5.11: Full timeseries of $x\text{CO}_2$ and $x\text{CH}_4$ for open-path and in-situ measurements. All measurements are gridded in intervals of 5 min. The grey shadings mark the time between local sunset and sunrise.

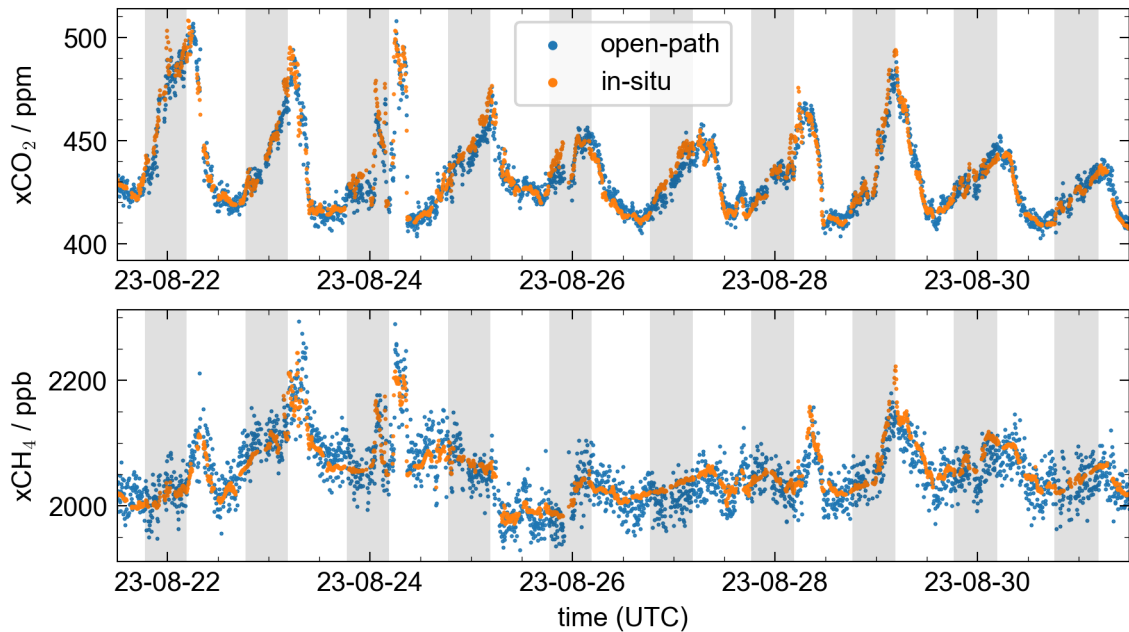


Figure 5.12: Ten days of $x\text{CO}_2$ and $x\text{CH}_4$ open-path and in-situ measurements. The grey shadings mark the time between local sunset and sunrise.

night time build up of $x\text{CO}_2$, followed by a morning drop, with the whole process spanning a range of 30 ppm on average. While this general shape matches the expectations, there are some differences between open-path and in-situ measurements, and between weekdays or weekends. First, the in-situ instrument seems to measure higher values on weekday afternoons and early evenings than the open-path instrument. This is visible in the larger weekday weekend difference for the in-situ instrument than for the open-path. Further, the difference between the instruments differ between weekdays and weekends during this time of the day. Second, during the night time buildup the in-situ instrument measures on average higher values for both weekend and weekdays. But these differences are of a comparable magnitude as the differences between weekend and weekdays during the night for both instruments, showing that sampling effects play most likely a comparable role.

Especially the significantly higher values for the in-situ instrument in the late afternoon could be a result of rush hour traffic. But, there is no comparable signal in the early morning. The absence of a clear rush hour signal (at least in the morning) is unexpected, since the in-situ instrument is located close to a major road with heavy commuter traffic. This should result in a stronger signal in the in-situ analyzer than the open-path measurements, since for the latter, the signal is diluted over the measurement path. While this might be the cause of the differences on weekdays around 14:00 to 17:00, the signal is maybe too weak to be visible

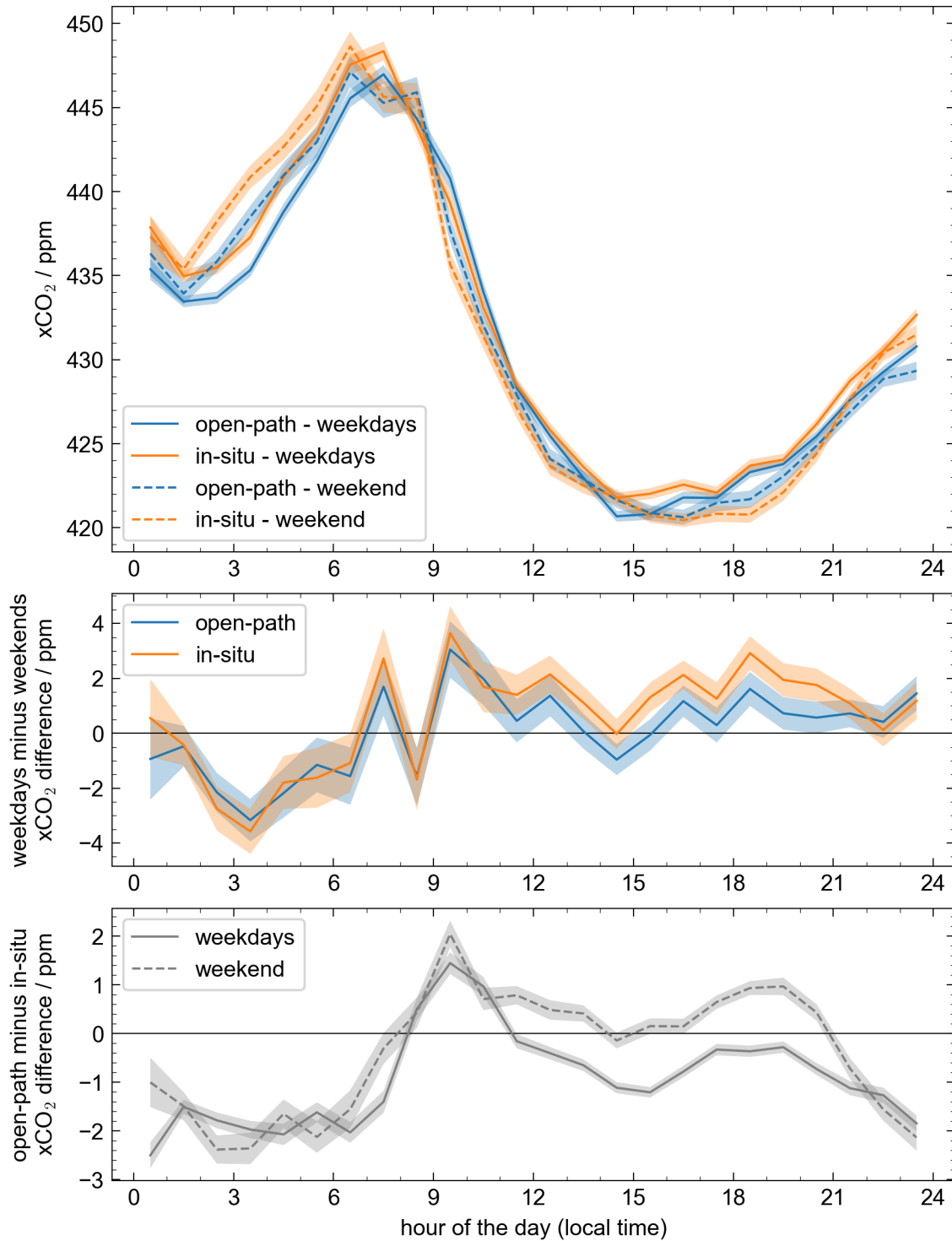


Figure 5.13: Top panel: Diurnal cycle of $x\text{CO}_2$ for weekdays and weekends. Middle panel: Differences between weekdays and weekends for each instrument. Bottom panel: Differences between the two instruments, separated for weekdays and weekends. Translucent bands give the standard error of the means. Please note, that the time axis is in local time.

in the mornings. There, the total signal is dominated by the mixing of the night time boundary layer enhancement with sharp temporal and maybe also spatial gradients. These large gradients also reinforce the problem of sampling bias, especially on the weekends. Still, it should be possible to extract signals on the differences between the two instruments and/or between weekends and weekdays. But this might require a larger dataset to reduce sampling error or more sophisticated evaluation routines to compensate for it. In the following, I take a closer look at the second potential signal in the diurnal cycle: the on average 1 ppm to 2 ppm smaller night time enhancements for the open-path measurements.

5.6.2 Statistical Analysis

Figure 5.14 shows histograms of the differences between the two instruments for both target gases for the full timeseries. Both distributions are centered around zero. The precision of the open-path instrument is the dominating factor in this comparison. We further ignore the systematic difference that the two instruments measure different bodies of air. Then, we calculate an expected FWHM for the distribution purely from the averaged precisions of the open-path timeseries (The FWHM of a gaussian is roughly 2.35 times its standard deviation). The resulting FWHMs are 6.6 ppm for $x\text{CO}_2$ and 47 ppb for $x\text{CH}_4$. This matches the observation in the histogram in the case of $x\text{CO}_2$. However, the distribution of the $x\text{CO}_2$ differences has a significant tail towards lower values, where the open-path instrument measures lower concentrations than the in-situ analyzer. This indicates a substantial number of measurements where the $x\text{CO}_2$ is substantially larger at the institute in comparison to the averaged concentration along the light path.

For $x\text{CH}_4$, the observed FWHM is around 60 ppb, which is wider than expected. Overall, the differences for $x\text{CH}_4$ follow a mostly symmetric distribution with no significant tails or biases. The reason for the larger than expected FWHM remains unclear, but might be a result of the different emission characteristics of CH_4 compared to CO_2 . Leakages from the natural gas distribution system and in some cases from the sewer system are the dominant emission sources in Heidelberg (Wietzel and Schmidt, 2023). Figure 5.15 gives an overview of such leakages in Heidelberg, which are highly variable in time and space. The residential area below the open-path (just north of the river Neckar) shows several such leakages. This could result in some measurements where the emission plumes pass the in-situ analyzer, resulting in higher values than for the open-path system, where the signal is diluted through the averaging nature of the measurement. If no or strongly diluted emission plumes pass the analyzer, this would turn around and

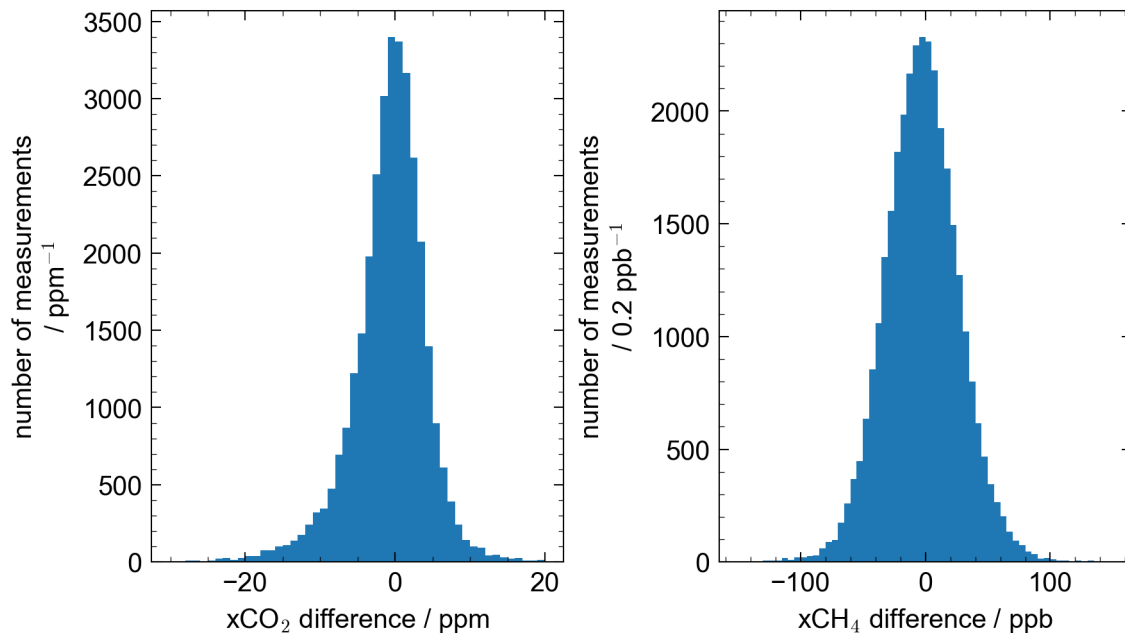


Figure 5.14: Value-by-value differences between the two instruments (open-path minus in-situ) for $x\text{CO}_2$ (left) and $x\text{CH}_4$ (right). Both distributions are centered around zero. We expect FWHMs of 6.6 ppm for $x\text{CO}_2$ and 47 ppb for $x\text{CH}_4$, assuming the open-path precisions of 2.8 ppm and 20 ppb respectively and neglecting the precision of the in-situ measurements, as well as neglecting any systematic differences. This does fit well for $x\text{CO}_2$, but less so for $x\text{CH}_4$, where the FWHM is more around 65 ppb. There are significant tails for $x\text{CO}_2$, with a clear bias towards lower values, so lower concentrations measured by the open-path instrument and higher concentrations measured by the in-situ analyzer.

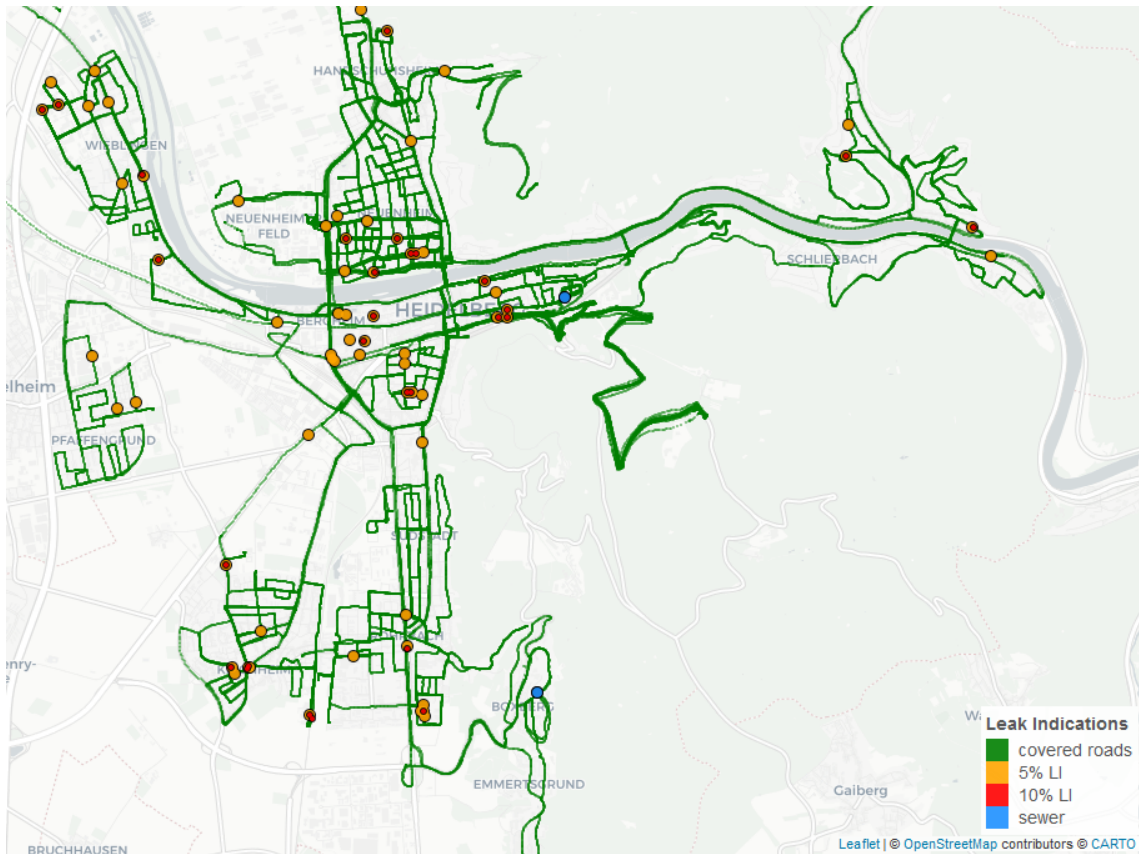


Figure 5.15: Overview of methane emissions in Heidelberg. LI stands for Leak Indication. A 5 % (10 %) LI refers to a 5 % (10 %) enhancement of the measured concentration over the background concentration in accordance with Weller et al. (2019). Figure taken with kind permission from Wietzel and Schmidt (2023).

result in larger values for the open-path instrument, since it is sensitive to a larger footprint and would measure a signal on a more regular basis. This matches the observation from Figure 5.12, where $x\text{CH}_4$ shows far more irregular patterns, dominated by hour long peaks and not by a diurnal cycle like $x\text{CO}_2$. But a detailed analysis of such a theory requires local air transport modelling, which is beyond the scope of this work.

5.6.3 Wind Direction Dependency

It turns out that most of these $x\text{CO}_2$ measurements, for which the open-path instrument measures significant lower values than the in-situ analyzer, occur in around a dozen events in February and March. Figure 5.16 showcases two such event in subsequent nights. The short four day time series starts with a night, which does not show a typical night time buildup, most likely due to the high

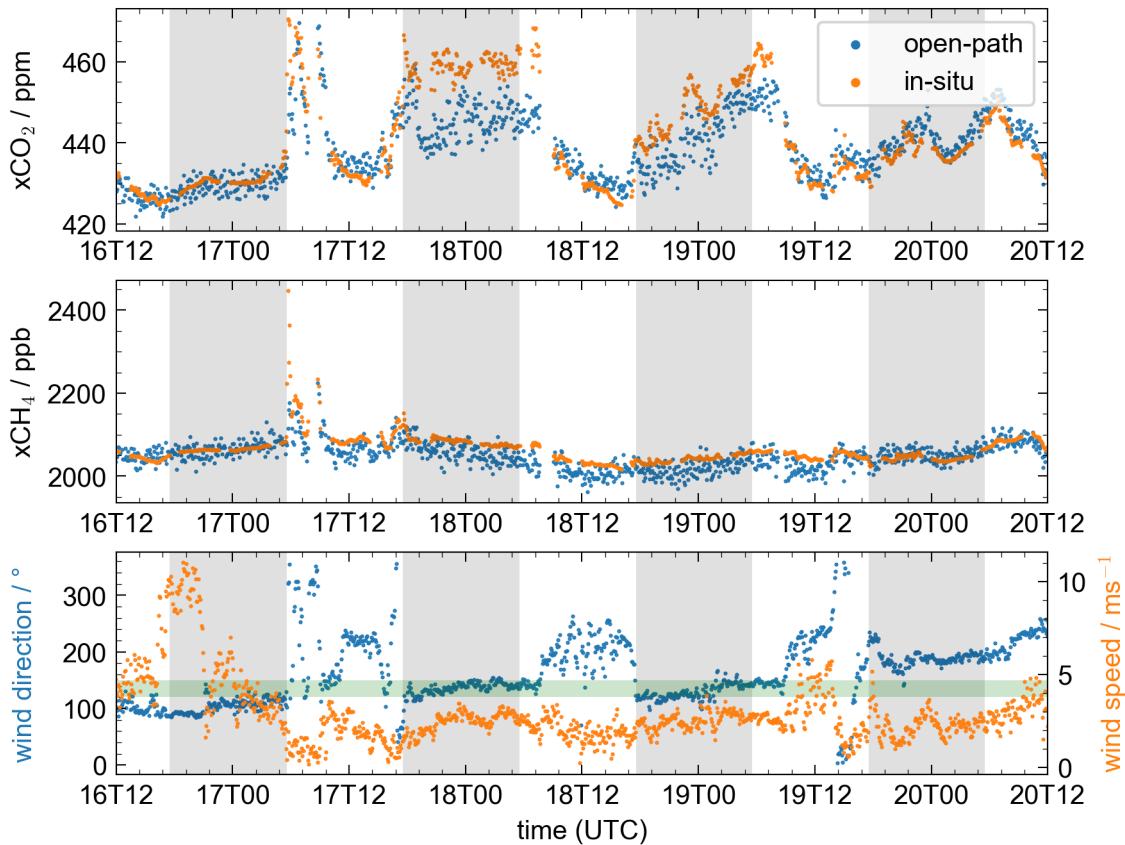


Figure 5.16: Example for night time $x\text{CO}_2$ enhancement of in-situ measurements compared to open-path results. During the two nights (grey shadings) from 2023-03-17 to 2023-03-19, the in-situ instrument measures significantly higher $x\text{CO}_2$ than the open-path instrument. For both nights, the wind is steadily blowing from $(135 \pm 15)^\circ$ (lower panel, green horizontal band). $x\text{CH}_4$ does not show any comparable signal within these nights.

wind speeds. In the following two nights we see a significant night time buildup for $x\text{CO}_2$, but a much stronger signal in the in-situ data than in the open-path measurements. The $x\text{CH}_4$ signal does not show any remarkable features in the respective night. The wind blows steadily with moderate intensity from south east. In the final night, the two instrument records on $x\text{CO}_2$ match again. The only difference during this last night is a shift in wind direction to southern winds. A manual analysis of the time series reveals, that all similar events which show these strong night time differences take place during steady wind situations with the wind blowing from about 135° . The correlation is also robust in reverse direction: all steady wind situations from this direction take place during night times in February and March and all but one indeed show this enhancement of the in-situ signal over the open-path values.

Moving away from manual analysis of events, we take a look at the differences for the two instruments depending on the wind direction. Figure 5.17 shows these for $x\text{CO}_2$ and $x\text{CH}_4$. We see clear difference in $x\text{CO}_2$ for wind directions from south east, while the difference is around zero for all other directions. Again and as expected, the in-situ instrument measures higher values than the open-path setup. We can also see that this is the result from a substantial number of measurements and these wind directions are in fact rather prominent. For $x\text{CH}_4$ the differences are around zero and do not show such a clear feature.

There are several potential explanations for this wind direction dependent $x\text{CO}_2$ bias between the two instruments. The most obvious one is a strong point source in the respective wind direction. If the plume of such a source directly passes the in-situ instruments, it measures a high enhancement, while the signal is diluted for the open-path instrument, which averages across 1.55 km path. However, there are two problems with this theory: Firstly, this should give rise to a wind vector where the plume is only passing through the measurement path of the open-path instrument but not the in-situ instrument. Thus, there should be a wind vector, where the open-path instruments measures significantly larger values, but there is no respective observation. Secondly, there are no matching point sources in this direction, as the map in Figure 5.18 of the inventories of the Netherlands Organisation for Applied Scientific Research (TNO, Super et al., 2020) shows. The only strong source which would match the wind direction is a road junction close to the in-situ analyzer. Together with the surrounding buildings, this could explain a strong CO_2 signal at the in-situ analyzer from a south eastern arc, but again this would not solve the problem of the missing reverse bias for a different wind direction. Also, there is no particularly strong traffic during night times, when these differences occur. Thus, it is unlikely that the wind direction dependent $x\text{CO}_2$ bias between the two instruments is caused by a strong and localized source.

Another possible reason for these wind direction dependent $x\text{CO}_2$ differences between the instruments is the different air mass transport for the two measurement setups. Up to now, we assumed a uniform wind direction across the surrounding region in our arguments. To estimate how valid this assumption is, we can consult simulated wind fields: Figure 5.19 shows a wind field 10 m above ground level, which was simulated with a combination of the Graz Mesoscale Model (GRAMM, Oettl, 2019a) and the Graz Lagrangian Model (GRAL, Oettl, 2019b). The plotted wind field is an average over all night time wind situations

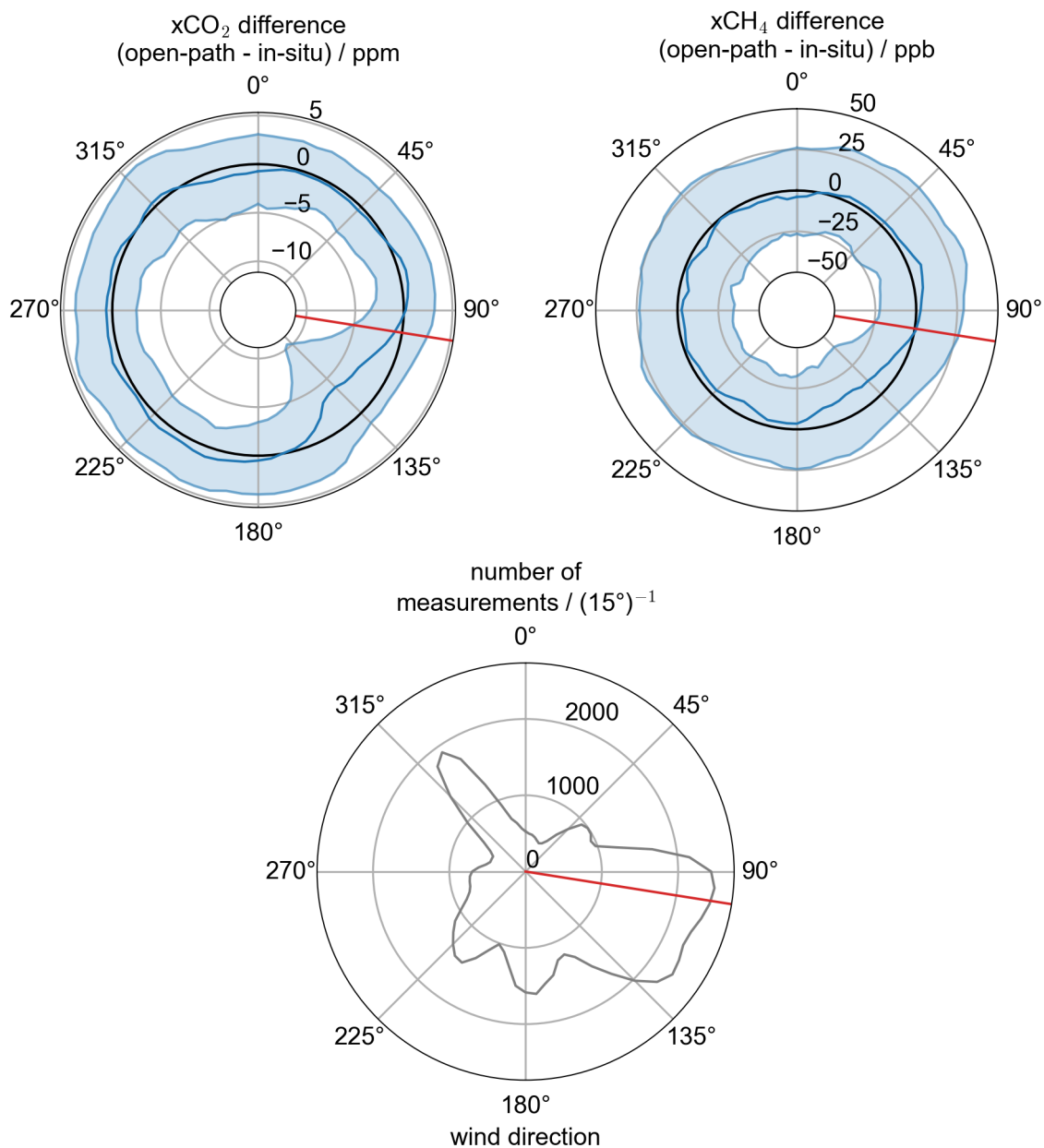


Figure 5.17: Differences between the two instruments (open-path minus in-situ) for xCO₂ and xCH₄ depending on wind direction. The solid blue line gives the average over all measurements, where the wind direction is within a $\pm 15^\circ$ interval centered at the respective direction. The surrounding band marks the area which contains the central 68.2% (one sigma for a gaussian distribution). The red line marks the viewing direction of the open-path instrument. The lower plot gives the number of measurements falling in each interval.

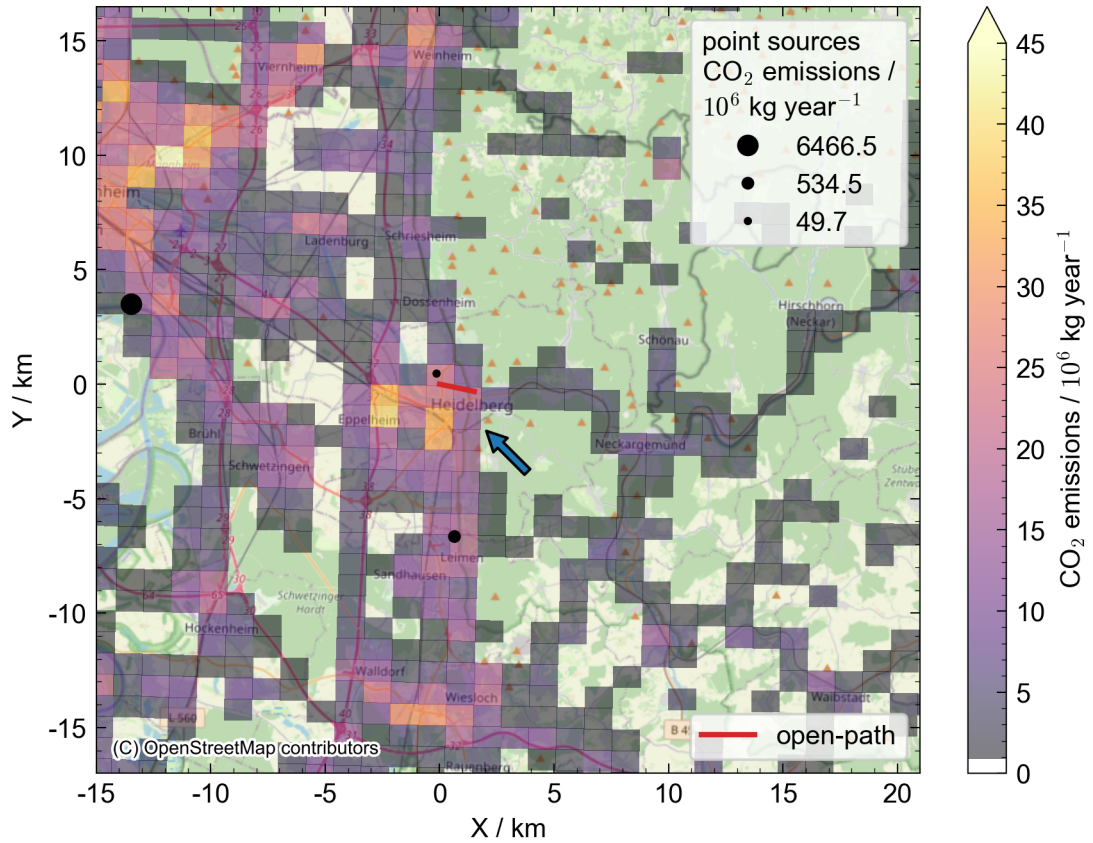


Figure 5.18: Emission map of anthropogenic CO₂ in the region around Heidelberg. All values taken from the inventories of the Netherlands Organisation for Applied Scientific Research (TNO, Super et al., 2020). Values below 1×10^6 kg year are not displayed. The coordinate system is centered on the IUP. The red line indicates the measurement path of the open-path system. The blue arrow indicates the 135° wind direction. The two relevant point sources in the direct area are a cement plant in the south and a close but small gas power plant north to north west of the institute. Further to the west is a large coal fired power plant in Mannheim. There are little emissions to the east of Heidelberg in the low mountain ranges of the Odenwald, but the most CO₂ emissions happen in the Rhine valley.

which experience wind from $(135 \pm 15)^\circ$ at the IUP from a catalogue² of simulated wind fields. The plotted wind field reveals that the wind direction and speed can vary significantly, especially in areas with high gradients in the topography. These gradients can result from the hills of the low mountain ranges in the east and the river valley cutting through them, or they can result from a high density of buildings and tall structures. Such transport differences could cause the two instruments to effectively measure quite different air masses. For example a wind of 135° at the west end of the path (at the IUP) might bring air from the densely populated areas south of the river (“Weststadt”, “Südstadt” areas), while the eastern parts of the open-path is exposed to CO₂-poor air from the river valley. This would again fit the observation from Figure 5.18, which shows that little emission takes place in the area east of Heidelberg. But while this concept can maybe explain the observed differences, it is clear that a robust argument needs accurate, high resolution information on air transport, which is currently only available through respective models. The combination of such high-resolution meteorological models with sufficiently resolved emission data is still a topic of ongoing research (Berchet et al., 2017b; Vardag and Maiwald, 2023). While it is unclear if they can sufficiently represent such effects, they are a promising candidate to inform on the representativeness of path averaged and point like measurements respectively.

5.6.4 Implication of the Instrument Differences for Emission Estimations.

By comparing the two instrument setups, we found two major points of inconsistency between them:

1. The xCH₄ differences show a larger variance than expected, symmetric in both directions.
2. The xCO₂ differences show a wind direction dependent high bias of the in-situ values for specific night time wind situations.

As discussed before, the exact identification of the origin of these differences requires further investigation, but the currently best explanations are, respectively, as follows:

²The catalogue contains wind fields for a variety of parameters, like the boundary conditions for wind speed and direction, as well as atmospheric stability.

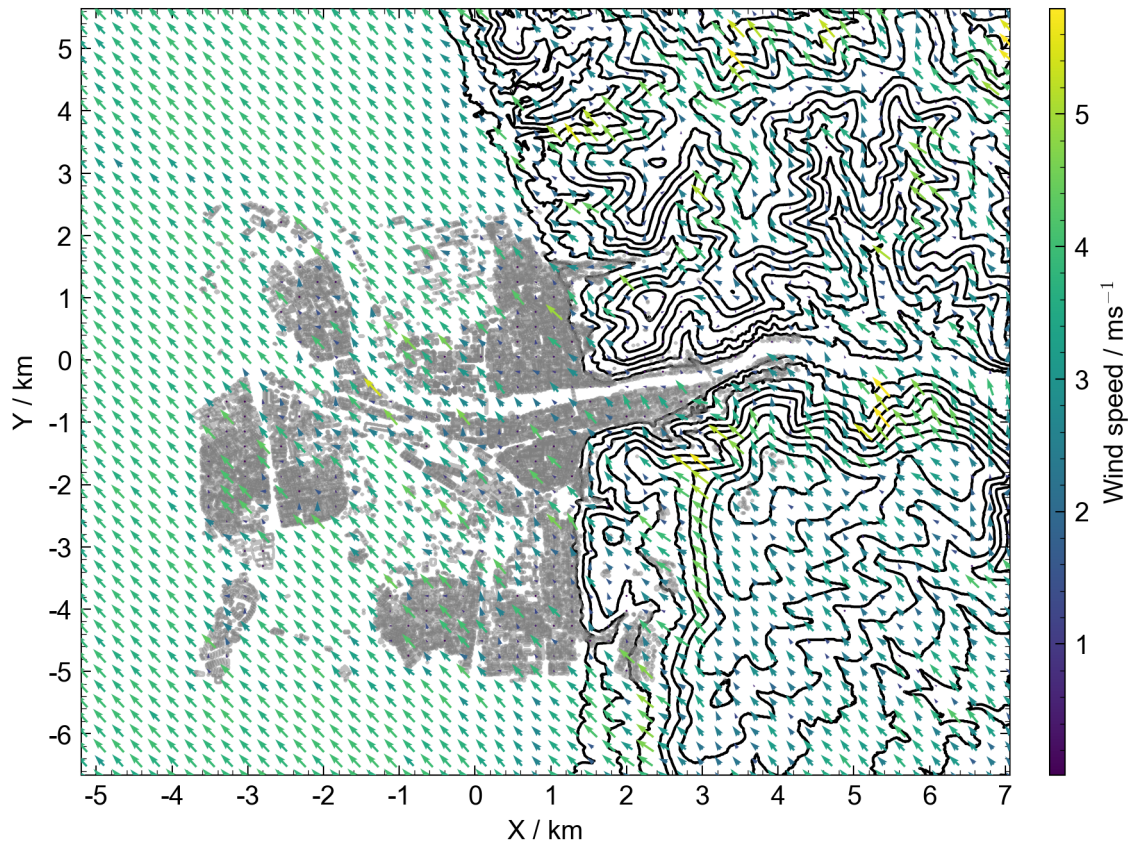


Figure 5.19: Simulated night time wind field in the city of Heidelberg. The coordinate system is centered on the IUP. Plotted is the wind at 10 m above ground level. The plotted wind field is an average over all simulated wind situations during night, which experience wind from $(135 \pm 15)^\circ$ at the IUP. The grey contours outline buildings, while the black contour lines show height in intervals of 50 m. The wind fields were simulated with the combined models GRAM/GRAL. Maximilian May carried out the simulation and kindly provided the data for this plot.

1. The larger $x\text{CH}_4$ differences are a result of the spatially and temporally irregular local emissions, caused mostly by leaks in the natural gas distribution system, and the different sensitivity/footprint of the two instruments to these emissions.
2. The wind direction dependent $x\text{CO}_2$ differences result from high sensitivities to the wind direction of the in-situ measured $x\text{CO}_2$ values. This is most likely caused by a local atmospheric transport phenomenon, where a slight change in wind direction changes the origin of the sampled air mass significantly.

We can now infer requirements for an atmospheric inversion setup to resolve the underlying processes. This resolving of the processes would be necessary for the inversion to arrive at the same flux results independently of which of the two measurements we would provide as input. As outlined in Chapter 1, an emission estimation based on an atmospheric inversion relies always on some prior assumption concerning the spatial and/or temporal structure of the emissions (Kaminski et al., 2001). Typically, a combination of (gridded) emission inventories, other spatially and temporally gridded data (e.g., population density, volume of traffic, or meteorological information), and models provide this structure (e.g., Stagakis et al., 2023). One example would be the gridding of emissions related to residential heating according to population density information, and modeling the emission strength as a function of temperature. Such an approach allows to account for the higher resolved structures of emissions, while limiting the degrees of freedom for example to a single scaling factor and avoid overfitting of the available measurement data. However, this relies on assumptions, generalizations, and simplified models, and uncertainties for example in the temporal profiles contribute significantly to the uncertainty of emission estimates (Super et al., 2020).

Against this background, we can conclude that resolving the effect of the larger $x\text{CH}_4$ differences due to the spatially and temporally irregular emissions by leakages would require some prior knowledge on their distribution. It is unlikely, that an inventory or other data could provide the knowledge of the spatial distribution of these leaks and model their emission strength with time. Thus, such an effect can likely not be captured, independently of the quality of the underlying atmospheric transport model. Spatially average measurements, like open-path measurements, could provide some advantage in this context, since they average over larger areas and are thus less sensitive to individual events than in-situ measurements.

However, resolving the effect of the wind direction dependent $x\text{CO}_2$ measurements caused by a local atmospheric transport phenomenon might be possible with sufficiently high spatial resolution of the atmospheric transport. We can conclude from Figure 4.1, Figure 5.18, Figure 5.19, and our prior analysis, that the relevant transport effects take place on the scale of at maximum one or two kilometers. It is unlikely that such transport phenomenon can be sufficiently represented on grid scales of kilometers and it is likely that a resolution on the scale of at least a hundred meter is required. This could include mesoscale models run on the scale of hundreds of meters (Zhao et al., 2023) or RANS models like GRAMM/GRAL (Berchet et al., 2017b; Vardag and Maiwald, 2023). In this case, the open-path measurements showed a less strong dependency on the wind direction, again indicating that spatially averaged measurements might provide an advantage by being less sensitive to processes unresolvable by the grid scale.

6 Summary and Conclusion

In this thesis, I set out the design, setup, and successful implementation of an open-path GHG observatory, which is based on a high resolution FTIR spectrometer. I evaluated the performance of the observatory based on the first eight months of measurements of the long term deployment in the city of Heidelberg, Germany. The main purpose of this observatory is to inform on the representativeness of point like measurements when compared to values averaged on a scale of kilometers, which is the typical grid spacing for mesoscale atmospheric transport models when used to estimate emissions from concentration measurements. To provide the database for such analysis, the setup aimed for continuous, low maintenance operation over months and possibly years. Finally, the setup was intended to serve as a flexible development tool for open-path measurements and their possible applications in general.

The open-path observatory is designed around the IFS 125HR high resolution FTIR spectrometer. The radiation from a halogen lamp is first modulated in the interferometer before transmitted along the open-path to make the measurement insensitive to light scattered into the beam. The open-path optics are based on fiber telescope technique, which is well established for differential optical absorption measurements with grating spectrometers and in the visible and ultraviolet spectral range. The detectors are a custom designed and built low noise room temperature (RT) InGaAs detector and a modified thermoelectric (TE) cooled InGaAs detector with wider spectral range, but worse noise performance. The custom retrieval software calculates column densities (CDs) of target gases. To do so, it models a spectrum based on tabulated absorption cross-sections and fits it to the measurements, using a Levenberg-Marquardt implementation. To correct for biases in the tabulated absorption band strengths, the resulting dry mixing ratios are bias corrected against in-situ data.

The setup showed an overall temporal coverage of more than 75 % in the period from 2023-02-08 until 2023-10-09, with up to 90 % in months where the instrument was fully dedicated to these measurements. This exceeds even the temporal coverage of the in-situ analyzer (70 %) within this time frame. The open-path

observatory can operate around the clock for months and requires only little to no maintenance within this time. Weather only partially affects the operation of the setup: Only weather conditions which significantly reduce the visibility along the 1.55 km path (like fog or heavy precipitation) constitute unsuitable conditions. With that, the current setup demonstrated its capability of continuous, unattended operation.

The open-path instrument demonstrated easy and flexible configuration of spectral and temporal resolution. Measurements at a resolution of 0.55 cm^{-1} and averaging times of 5 min currently provide the best performance for target gases like CO_2 and CH_4 . An analysis of Allan deviations on the basis of the 1 min measurements showed that an averaging time of 5 min is a good choice for the setup up in its current form and noise performance to avoid averaging out real signal variability, while still minimizing measurement uncertainty. Measurements at higher spectral resolution (0.11 cm^{-1}) provide informative spectral residuals due to the nearly negligible width of the ILS, though at the cost of worse precision of the retrieved target gas mixing ratios. Three months of such measurements are already available and could provide a useful dataset for future testing and validation of cross-section databases. The tests of the custom built RT detector demonstrated the capability to swap out the utilized detectors, which provides further possibilities to adapt and optimize the setup for different target gases and research interests in the future. Due to its good noise characteristics, the RT detector provides better performances whenever the higher spectral bandwidth of the TE detector is not required. With that, the open-path observatory proved to be a versatile research instrument and a capable vehicle for methodology development.

Evaluation of the open-path spectra lead to technical findings, which concern (FTIR) open-path measurements in general. First, I found that inclusion of line-mixing effects in the cross-sections for the $2\text{ }\mu\text{m}$ CO_2 window is necessary to obtain accurate temperature information on the gas column and to improve the spectral fit. This is an improvement with respect to the pilot study performed by Griffith et al. (2018) and subsequent works based on their achievements. Moreover, this applies to open-path measurements independent of the spectroscopic technique, especially if the retrieved temperature information is further used to calculate dry air columns and mixing ratios. Second, I found that fluctuations of the transmitted light intensity due to refraction in a turbulent atmosphere modifies the ILS for each measured spectrum individually. As a result, the retrieved gas CDs contain systematic errors, which partially cancel out when calculating

ratios, resulting in lower than expected noise for mixing ratios. In the presented case, this reduced the noise of mixing ratios even below the noise for the individual CDs, but for setups with higher light throughput the noise reduction might not be as severe. This concerns all types of FTIR open-path setups and is similar to intensity fluctuations encountered with sun-viewing measurements using FTIR instruments, where typically a so-called DC correction is employed to compensate. This invites further research into how this method can be adapted for open-path setups, since this method is likely not directly applicable to this type of measurement.

The open-path measured CO₂ and CH₄ data are overall in good agreement with a co-deployed in-situ instrument. Both records show the seasonal decrease of CO₂ from mid April onward, which results from increased gross primary production in the northern hemisphere. They also follow the same general diurnal cycle, which is dominated by an accumulation of CO₂ over night in the planetary boundary layer, followed by a subsequent sharp drop with the onset of solar heating and resulting mixing of the boundary layer. The two instruments show some differences in the afternoon and early evening, especially when comparing weekday and weekend signals, potentially a result of different sensitivities to traffic emissions.

The comparison of open-path and in-situ measurements also revealed two major inconsistencies: First, the differences between the instruments for xCH₄ measurements showed a larger variance than expected (around 65 ppb instead of 47 ppb). This is likely caused by the spatially and temporally irregular emissions from leaks in the natural gas distribution system. They are the dominant source for CH₄ emissions in the area (Wietzel and Schmidt, 2023) and are not captured by both instruments equally. Second, the comparison revealed a substantial number of measurements where the in-situ instrument measured significantly (10 ppm and more) higher xCO₂ values than the open-path instrument. These measurements correspond to around ten specific nighttime events in February and March and showed a strong correlation with wind direction, occurring only together with firm winds from $135^\circ \pm 15^\circ$. While there are multiple possible explanations, this difference is most likely the result of a local atmospheric transport phenomenon. As a result, the two instruments measure air masses of different origin and have a different sensitivity to local emission patterns. In summary, both of these inconsistencies between the two instruments likely result from their respective spatial averaging scales. Detailed modelling of such point-based and path averaged measurements on a scale of tens of meters in combination with

the measured data could provide further insight in the origin of the instrument differences and increase the significance of the results. To reconcile the measured CO₂ differences for emission estimates, it is likely necessary to resolve the underlying local transport effect, requiring modeling of the atmospheric transport at grid scales below one kilometer. However, it is unrealistic that emission patterns like those of the CH₄ leaks can be accurately captured by the current model approaches on the basis of emission inventories, rendering an accurate capture and local attribution of such emissions by atmospheric inversion techniques unlikely. In conclusion, the dataset obtained with the presented open-path observatory for GHGs fulfills its primary objective to provide information on the representativeness of in-situ systems on the kilometer scale and can inform on the importance of sub-grid processes unresolvable by the mesoscale atmospheric transport models used for emission estimates.

Continuous operation of the open-path observatory will steadily expand the presented dataset. High resolution measurements will provide a valuable testing ground for spectroscopic databases. They bridge the gap between highly controlled laboratory settings with absorption paths on the order of tens to hundreds of meters to a real and variable atmosphere with an absorption path of kilometers, while keeping the overall radiative transport and environmental conditions rather simple. Substantial improvements of cross-section databases would improve on the native accuracy of GHG remote sensing techniques and could reduce their current reliability on in-situ data for bias correction. A long time-series of open-path xCO₂ and xCH₄ measurements in combination with in-situ data will provide a great basis to further explore the representativeness of in-situ instruments on the kilometer scale. Combining this data with combinations of atmospheric transport models and a-priori emission data will in turn provide insights into the representativeness of the respective models and weather they can resolve such effects and differences. Both applications contribute to bridge between in-situ measurements and spatially averaged measurements like satellite data, helping to synthesize their information and to improve on emission estimations.

Acknowledgements

As is the case for almost any project, many people contributed to enable it, to enable me to succeed. Here, I would like to acknowledge the help of everyone involved in this journey. Many thanks go to:

Prof. Dr. André Butz, for providing me this opportunity and for the always purposeful and constructive work relationship; for guiding my research with his experience and knowledge, while leaving me freedom and independence to solve problems on my own and my way.

Dr. Frank Hase, for sharing his knowledge, especially on FTIR spectroscopy; for the curiosity driven exchange on many technical matters, and for the positive and encouraging feedback.

Prof. Dr. David W. T. Griffith, for sharing his experiences with the pioneering setup and for helping to hunt down technical details and differences.

Dr. Manfred Birk and Dr. Georg Wagner, for showing me their lab, discussions on FTIR spectroscopy and helping me navigate the notation jungle surrounding rotational-vibrational transitions.

Benedikt Löw, for being a constant and companion throughout my studies of physics and environmental physics in particular; for often posing the critical and important questions, thereby providing a corrective when I got carried away by enthusiasm; for all the constructive and enjoyable conversations and shared discoveries.

Jonas Kuhn, for enabling me to get a first foot on the ground in all of this “instrument-designing-business”; for all the time investment in discussions on interesting optics and physics problems and the humble, down-to-earth attitude to approach them.

Dr. Sanam Vardag, for her advice on many topics, including everything related to modeling, but also writing style and presentation; for often providing fresh and different perspectives on many results in this work.

Prof. Dr. Norbert Frank, for providing me with his perspective and orientation on the last three decades of paleoclimate studies when I struggled to navigate that field in the final stages of writing this thesis; for getting me into environmental physics in the first place with his motivating style of giving lectures.

Ralph Kleinscheck, for providing indispensable technical and operational support for a successful long term deployment of the open-path system; for all the hours of collaborative work in the lab, and for all the collaborative pondering over possible solutions to problems.

Angelika Gassama, for providing necessary order and structure in many places of the institute, where otherwise chaos would reign.

Lukas Pilz, for his relentless support and push for better software standards and practices, from which all of my software in the last years and the future profited and continues to profit.

Robert Maiwald and Lukas Pilz, for providing me with preprocessed emission inventory data and corresponding example plots.

Maximilian May, for providing the wind simulation data and a corresponding example plot.

Dr. Martina Schmidt, William Cranton, and Julia Wietzel, for operating the in-situ analyzer at our institute and providing me with the necessary data.

Prof. Grant Petty and Julia Wietzel, for kindly allowing me to use figures from their respective works.

Antje Hoheisel, for sharing her expertise on in-situ instrumentation and analysis of time series.

Dr. Samuel Hammer, Susanne Preunkert, and Angelika Gassama for keeping the institute weather station running reliably.

Dr. Stefan Schmitt, for sharing his open-path experience with me.

Lukas Weis, Thomas Plewa, Victor Ksoll, Eva Metz, Jonathan Langenbach, Benedikt Löw, Martin Braß, Simon Heidrich, Samuel Hammer, and Sanam Vardag for providing valuable feedback on the script of this thesis.

Felix Klein, Felix Kühlheim, and Paul Edinger, for joining me and my research for their respective theses; for putting up with the less than ideal boundary conditions of a pandemic and all the challenges that came with it: be it the drop of intended lab work, or less supervision than anticipated.

Marvin Knapp, for his positive attitude and cheerful mood, which often lightens the spirits in the office; for having different approaches to many challenges in work and life than I do, and thus enabling me to look beyond the horizon and learning a lot for the future.

Eva Metz, for the shared tea breaks, whenever it was necessary or just delightful; for the professional, constructive, and solution oriented feedback on my science and the related argumentation and communication.

Thomas Plewa, for great conversations ranging from mundane to the depths (to me) of general relativity or statistical physics.

Karolin Voss and Philip Holzbeck, for great discussion and conversations shared in the lab or over a cup of tea.

Chrissy Proß, for in depth conversations about physics and the shared urge of wanting to get to the bottom of something; for sharing her work with me, and for the drive and motivation she emanates.

The whole atmo-group, for the collegial, up-lifting atmosphere; for all the fun times and good and constructive conversations, which I could not mention explicitly, or simply forgot.

The Heidelberg Center for the Environment and the HCE-College, for providing a platform for exchange between different disciplines, and for the financial support.

Felix Steiner, in general for his practical approach to engineering and problem solving; more precisely for serving as a discussion partner concerning electronics, amplification and noise.

Victor Ksoll, for his thorough comments to any question or discussion brought before him; for providing feedback on the manuscript's draft on short notice; for providing excellent feedback on writing style, but also on miscellaneous questions, sometimes quite late at night.

Martin Braß, in my opinion one of the brightest minds my generation of physicists has to offer, for always being open minded and curious for any physics problem; for spending countless hours discussing physics with me and helping me to make connections in ways I could not have done on my own; and last but not least, for taking up the inglorious task of checking my calculations, where I did not fully trust them.

Jonathan Langenbach, for providing unique perspectives on a plethora of topics and making me a better scholar; for sticking to our long tradition of making sure that the other is not consumed by his work.

Anne Föllner, for her understanding and support, especially in the final phases of this work; for providing a safe haven to unwind and gather energy for the tasks before me.

My parents, for their support, care to keep the motivation high, and literature on electronics, which I definitely borrowed longer than necessary.

Bibliography

- An, N., Mustafa, F., Bu, L., Xu, M., Wang, Q., Shahzaman, M., Bilal, M., Ullah, S., and Feng, Z.: Monitoring of Atmospheric Carbon Dioxide over Pakistan Using Satellite Dataset, *Remote Sensing*, 14, 5882, <https://doi.org/10.3390/rs14225882>, 2022.
- Arioli, M. S., D'Agosto, M. D. A., Amaral, F. G., and Cybis, H. B. B.: The Evolution of City-Scale GHG Emissions Inventory Methods: A Systematic Review, *Environmental Impact Assessment Review*, 80, 106316, <https://doi.org/10.1016/j.eiar.2019.106316>, 2020.
- Aubinet, M., Grelle, A., Ibrom, A., Rannik, Ü., Moncrieff, J., Foken, T., Kowalski, A., Martin, P., Berbigier, P., Bernhofer, Ch., Clement, R., Elbers, J., Granier, A., Grünwald, T., Morgenstern, K., Pilegaard, K., Rebmann, C., Snijders, W., Valentini, R., and Vesala, T.: Estimates of the Annual Net Carbon and Water Exchange of Forests: The EUROFLUX Methodology, in: *Advances in Ecological Research*, vol. 30, pp. 113–175, Elsevier, [https://doi.org/10.1016/S0065-2504\(08\)60018-5](https://doi.org/10.1016/S0065-2504(08)60018-5), 1999.
- Bai, M., Flesch, T., Trouvé, R., Coates, T., Butterly, C., Bhatta, B., Hill, J., and Chen, D.: Gas Emissions during Cattle Manure Composting and Stockpiling, *J Environ Qual*, 49, 228–235, <https://doi.org/10.1002/jeq2.20029>, 2020.
- Bailey, D. M., Adkins, E. M., and Miller, J. H.: An Open-Path Tunable Diode Laser Absorption Spectrometer for Detection of Carbon Dioxide at the Bonanza Creek Long-Term Ecological Research Site near Fairbanks, Alaska, *Appl Phys B*, 123, 245, <https://doi.org/10.1007/s00340-017-6814-8>, 2017.
- Baklanov, A., Schlünzen, K., Suppan, P., Baldasano, J., Brunner, D., Aksoyoglu, S., Carmichael, G., Douros, J., Flemming, J., Forkel, R., Galmarini, S., Gauss, M., Grell, G., Hirtl, M., Joffre, S., Jorba, O., Kaas, E., Kaasik, M., Kallos, G., Kong, X., Korsholm, U., Kurganskiy, A., Kushta, J., Lohmann, U., Mahura, A., Manders-Groot, A., Maurizi, A., Moussiopoulos, N., Rao, S. T., Savage, N., Seigneur, C., Sokhi, R. S., Solazzo, E., Solomos, S., Sørensen, B., Tsegas, G., Vignati, E., Vogel,

- B., and Zhang, Y.: Online Coupled Regional Meteorology Chemistry Models in Europe: Current Status and Prospects, *Atmos. Chem. Phys.*, 14, 317–398, <https://doi.org/10.5194/acp-14-317-2014>, 2014.
- Basu, S., Guerlet, S., Butz, A., Houweling, S., Hasekamp, O., Aben, I., Krummel, P., Steele, P., Langenfelds, R., Torn, M., Biraud, S., Stephens, B., Andrews, A., and Worthy, D.: Global CO₂ Fluxes Estimated from GOSAT Retrievals of Total Column CO₂, *Atmos. Chem. Phys.*, 13, 8695–8717, <https://doi.org/10.5194/acp-13-8695-2013>, 2013.
- Beck, V., Gerbig, C., Koch, T., Bela, M. M., Longo, K. M., Freitas, S. R., Kaplan, J. O., Prigent, C., Bergamaschi, P., and Heimann, M.: WRF-Chem Simulations in the Amazon Region during Wet and Dry Season Transitions: Evaluation of Methane Models and Wetland Inundation Maps, *Atmos. Chem. Phys.*, 13, 7961–7982, <https://doi.org/10.5194/acp-13-7961-2013>, 2013.
- Berchet, A., Zink, K., Muller, C., Oetl, D., Brunner, J., Emmenegger, L., and Brunner, D.: A Cost-Effective Method for Simulating City-Wide Air Flow and Pollutant Dispersion at Building Resolving Scale, *Atmospheric Environment*, 158, 181–196, <https://doi.org/10.1016/j.atmosenv.2017.03.030>, 2017a.
- Berchet, A., Zink, K., Oetl, D., Brunner, J., Emmenegger, L., and Brunner, D.: Evaluation of High-Resolution GRAMM–GRAL (V15.12/V14.8) NO_x Simulations over the City of Zürich, Switzerland, *Geosci. Model Dev.*, 10, 3441–3459, <https://doi.org/10.5194/gmd-10-3441-2017>, 2017b.
- Bernath, P. F.: *Spectra of Atoms and Molecules*, Oxford University Press, New York, 2nd ed edn., 2005.
- Birk, M., Röske, C., and Wagner, G.: High Accuracy CO₂ Fourier Transform Measurements in the Range 6000–7000 Cm⁻¹, *J QUANT SPECTROSC RA*, 272, 107791, <https://doi.org/10.1016/j.jqsrt.2021.107791>, 2021.
- Bousquet, P., Gaudry, A., Ciais, P., Kazan, V., Monfray, P., Simmonds, P., Jennings, S., and O'Connor, T.: Atmospheric CO₂ Concentration Variations Recorded at Mace Head, Ireland, from 1992 to 1994, *Physics and Chemistry of the Earth*, 21, 477–481, [https://doi.org/10.1016/S0079-1946\(97\)81145-7](https://doi.org/10.1016/S0079-1946(97)81145-7), 1996.
- Bransden, B. H., Joachain, C. J., and Joachain, C. J.: *Physics of Atoms and Molecules*, Prentice Hall, Harlow Munich, 2. ed., [nachdr.] edn., 2003.

- Brault, J. W.: New Approach to High-Precision Fourier Transform Spectrometer Design, *Appl. Opt.*, 35, 2891, <https://doi.org/10.1364/AO.35.002891>, 1996.
- Brioude, J., Kim, S.-W., Angevine, W. M., Frost, G. J., Lee, S.-H., McKeen, S. A., Trainer, M., Fehsenfeld, F. C., Holloway, J. S., Ryerson, T. B., Williams, E. J., Petron, G., and Fast, J. D.: Top-down Estimate of Anthropogenic Emission Inventories and Their Interannual Variability in Houston Using a Mesoscale Inverse Modeling Technique, *J. Geophys. Res.*, 116, D20 305, <https://doi.org/10.1029/2011JD016215>, 2011.
- Brioude, J., Angevine, W. M., Ahmadov, R., Kim, S.-W., Evan, S., McKeen, S. A., Hsie, E.-Y., Frost, G. J., Neuman, J. A., Pollack, I. B., Peischl, J., Ryerson, T. B., Holloway, J., Brown, S. S., Nowak, J. B., Roberts, J. M., Wofsy, S. C., Santoni, G. W., Oda, T., and Trainer, M.: Top-down Estimate of Surface Flux in the Los Angeles Basin Using a Mesoscale Inverse Modeling Technique: Assessing Anthropogenic Emissions of CO, NO_x and CO₂ and Their Impacts, *Atmos. Chem. Phys.*, 13, 3661–3677, <https://doi.org/10.5194/acp-13-3661-2013>, 2013.
- Butz, A., Guerlet, S., Hasekamp, O., Schepers, D., Galli, A., Aben, I., Frankenberg, C., Hartmann, J.-M., Tran, H., Kuze, A., Keppel-Aleks, G., Toon, G., Wunch, D., Wennberg, P., Deutscher, N., Griffith, D., Macatangay, R., Messerschmidt, J., Notholt, J., and Warneke, T.: Toward Accurate CO₂ and CH₄ Observations from GOSAT: GOSAT CO₂ and CH₄ Validation, *Geophys. Res. Lett.*, 38, n/a–n/a, <https://doi.org/10.1029/2011GL047888>, 2011.
- Chandra, N., Patra, P. K., Niwa, Y., Ito, A., Iida, Y., Goto, D., Morimoto, S., Kondo, M., Takigawa, M., Hajima, T., and Watanabe, M.: Estimated Regional CO₂ Flux and Uncertainty Based on an Ensemble of Atmospheric CO₂ Inversions, *Atmos. Chem. Phys.*, 22, 9215–9243, <https://doi.org/10.5194/acp-22-9215-2022>, 2022.
- Chevallier, F., Broquet, G., Zheng, B., Ciais, P., and Eldering, A.: Large CO₂ Emitters as Seen From Satellite: Comparison to a Gridded Global Emission Inventory, *Geophysical Research Letters*, 49, e2021GL097 540, <https://doi.org/10.1029/2021GL097540>, 2022.
- Coddington, I., Newbury, N., and Swann, W.: Dual-Comb Spectroscopy, *OPTICA*, 3, 414, <https://doi.org/10.1364/OPTICA.3.000414>, 2016.

- Collins, M., An, S.-I., Cai, W., Ganachaud, A., Guilyardi, E., Jin, F.-F., Jochum, M., Lengaigne, M., Power, S., Timmermann, A., Vecchi, G., and Wittenberg, A.: The Impact of Global Warming on the Tropical Pacific Ocean and El Niño, *Nature Geosci*, 3, 391–397, <https://doi.org/10.1038/ngeo868>, 2010.
- Cusworth, D. H., Duren, R. M., Thorpe, A. K., Eastwood, M. L., Green, R. O., Dennison, P. E., Frankenberg, C., Heckler, J. W., Asner, G. P., and Miller, C. E.: Quantifying Global Power Plant Carbon Dioxide Emissions With Imaging Spectroscopy, *AGU Advances*, 2, e2020AV000350, <https://doi.org/10.1029/2020AV000350>, 2021.
- Davis, K. J., Deng, A., Lauvaux, T., Miles, N. L., Richardson, S. J., Sarmiento, D. P., Gurney, K. R., Hardesty, R. M., Bonin, T. A., Brewer, W. A., Lamb, B. K., Shepson, P. B., Harvey, R. M., Cambaliza, M. O., Sweeney, C., Turnbull, J. C., Whetstone, J., and Karion, A.: The Indianapolis Flux Experiment (INFLUX): A Test-Bed for Developing Urban Greenhouse Gas Emission Measurements, *Elementa: Science of the Anthropocene*, 5, 21, <https://doi.org/10.1525/elementa.188>, 2017.
- Derwent, R., Ryall, D., Manning, A., Simmonds, P., O'Doherty, S., Biraud, S., Ciais, P., Ramonet, M., and Jennings, S.: Continuous Observations of Carbon Dioxide at Mace Head, Ireland from 1995 to 1999 and Its Net European Ecosystem Exchange, *Atmospheric Environment*, 36, 2799–2807, [https://doi.org/10.1016/S1352-2310\(02\)00203-0](https://doi.org/10.1016/S1352-2310(02)00203-0), 2002.
- Deutscher, N. M., Naylor, T. A., Caldwor, C. G. R., McDougall, H. L., Carter, A. G., and Griffith, D. W. T.: Performance of an Open-Path near-Infrared Measurement System for Measurements of CO₂ and CH₄ during Extended Field Trials, *ATMOS MEAS TECH*, 14, 3119–3130, <https://doi.org/10.5194/amt-14-3119-2021>, 2021.
- Diffenbaugh, N. S. and Scherer, M.: Observational and Model Evidence of Global Emergence of Permanent, Unprecedented Heat in the 20th and 21st Centuries: A Letter, *Climatic Change*, 107, 615–624, <https://doi.org/10.1007/s10584-011-0112-y>, 2011.
- Dobler, J., Braun, M., Blume, N., and Zaccheo, T.: A New Laser Based Approach for Measuring Atmospheric Greenhouse Gases, *REMOTE SENS-BASEL*, 5, 6284–6304, <https://doi.org/10.3390/rs5126284>, 2013.

- Dou, X., Hong, J., Ciais, P., Chevallier, F., Yan, F., Yu, Y., Hu, Y., Huo, D., Sun, Y., Wang, Y., Davis, S. J., Crippa, M., Janssens-Maenhout, G., Guizzardi, D., Solazzo, E., Lin, X., Song, X., Zhu, B., Cui, D., Ke, P., Wang, H., Zhou, W., Huang, X., Deng, Z., and Liu, Z.: Near-Real-Time Global Gridded Daily CO₂ Emissions 2021, *Sci Data*, 10, 69, <https://doi.org/10.1038/s41597-023-01963-0>, 2023.
- Etminan, M., Myhre, G., Highwood, E. J., and Shine, K. P.: Radiative Forcing of Carbon Dioxide, Methane, and Nitrous Oxide: A Significant Revision of the Methane Radiative Forcing, *Geophysical Research Letters*, 43, <https://doi.org/10.1002/2016GL071930>, 2016.
- Fiehn, A., Kostinek, J., Eckl, M., Klausner, T., Gałkowski, M., Chen, J., Gerbig, C., Röckmann, T., Maazallahi, H., Schmidt, M., Korbeń, P., Nečki, J., Jagoda, P., Wildmann, N., Mallaun, C., Bun, R., Nickl, A.-L., Jöckel, P., Fix, A., and Roiger, A.: Estimating CH₄, CO₂ and CO Emissions from Coal Mining and Industrial Activities in the Upper Silesian Coal Basin Using an Aircraft-Based Mass Balance Approach, *ATMOS CHEM PHYS*, 20, 12 675–12 695, <https://doi.org/10.5194/acp-20-12675-2020>, 2020.
- Fleurbaey, H., Reed, Z. D., Adkins, E. M., Long, D. A., and Hodges, J. T.: High Accuracy Spectroscopic Parameters of the 1.27 Mm Band of O₂ Measured with Comb-Referenced, Cavity Ring-down Spectroscopy, *Journal of Quantitative Spectroscopy and Radiative Transfer*, 270, 107 684, <https://doi.org/10.1016/j.jqsrt.2021.107684>, 2021.
- Frankenberg, C., Bergamaschi, P., Butz, A., Houweling, S., Meirink, J. F., Notholt, J., Petersen, A. K., Schrijver, H., Warneke, T., and Aben, I.: Tropical Methane Emissions: A Revised View from SCIAMACHY Onboard ENVISAT, *Geophysical Research Letters*, 35, 2008GL034 300, <https://doi.org/10.1029/2008GL034300>, 2008.
- Frey, M., Sha, M. K., Hase, F., Kiel, M., Blumenstock, T., Harig, R., Surawicz, G., Deutscher, N. M., Shiomi, K., Franklin, J. E., Bösch, H., Chen, J., Grutter, M., Ohyama, H., Sun, Y., Butz, A., Mengistu Tsidu, G., Ene, D., Wunch, D., Cao, Z., Garcia, O., Ramonet, M., Vogel, F., and Orphal, J.: Building the COllaborative Carbon Column Observing Network (COCCON): Long-Term Stability and Ensemble Performance of the EM27/SUN Fourier Transform Spectrometer, *ATMOS MEAS TECH*, 12, 1513–1530, <https://doi.org/10.5194/amt-12-1513-2019>, 2019.

- Galtier, S., Pivard, C., and Rairoux, P.: Towards DCS in the UV Spectral Range for Remote Sensing of Atmospheric Trace Gases, *Remote Sensing*, 12, 3444, <https://doi.org/10.3390/rs12203444>, 2020.
- Gerbig, C., Korner, S., and Lin, J. C.: Vertical Mixing in Atmospheric Tracer Transport Models: Error Characterization and Propagation, *Atmos. Chem. Phys.*, 2008.
- Gillett, N. P., Kirchmeier-Young, M., Ribes, A., Shiogama, H., Hegerl, G. C., Knutti, R., Gastineau, G., John, J. G., Li, L., Nazarenko, L., Rosenbloom, N., Seland, Ø., Wu, T., Yukimoto, S., and Ziehn, T.: Constraining Human Contributions to Observed Warming since the Pre-Industrial Period, *Nat. Clim. Chang.*, 11, 207–212, <https://doi.org/10.1038/s41558-020-00965-9>, 2021.
- Giorgetta, F. R., Peischl, J., Herman, D. I., Ycas, G., Coddington, I., Newbury, N. R., and Cossel, K. C.: Open-Path Dual-Comb Spectroscopy for Multispecies Trace Gas Detection in the 4.5–5 Mm Spectral Region, *Laser & Photonics Reviews*, 15, 2000583, <https://doi.org/10.1002/lpor.202000583>, 2021.
- Gisi, M., Hase, F., Dohe, S., Blumenstock, T., Simon, A., and Keens, A.: XCO₂-Measurements with a Tabletop FTS Using Solar Absorption Spectroscopy, *Atmos. Meas. Tech.*, 5, 2969–2980, <https://doi.org/10.5194/amt-5-2969-2012>, 2012.
- Gordon, I., Rothman, L., Hargreaves, R., Hashemi, R., Karlovets, E., Skinner, F., Conway, E., Hill, C., Kochanov, R., Tan, Y., Wcisło, P., Finenko, A., Nelson, K., Bernath, P., Birk, M., Boudon, V., Campargue, A., Chance, K., Coustenis, A., Drouin, B., Flaud, J., Gamache, R., Hodges, J., Jacquemart, D., Mlawer, E., Nikitin, A., Perevalov, V., Rotger, M., Tennyson, J., Toon, G., Tran, H., Tyuterev, V., Adkins, E., Baker, A., Barbe, A., Canè, E., Császár, A., Dudaryonok, A., Egorov, O., Fleisher, A., Fleurbaey, H., Foltynowicz, A., Furtenbacher, T., Harrison, J., Hartmann, J., Horneman, V., Huang, X., Karman, T., Karns, J., Kassi, S., Kleiner, I., Kofman, V., Kwabia-Tchana, F., Lavrentieva, N., Lee, T., Long, D., Lukashevskaya, A., Lyulin, O., Makhnev, V.Yu., Matt, W., Massie, S., Melosso, M., Mikhailenko, S., Mondelain, D., Müller, H., Naumenko, O., Perrin, A., Polyansky, O., Raddaoui, E., Raston, P., Reed, Z., Rey, M., Richard, C., Tóbiás, R., Sadiq, I., Schwenke, D., Starikova, E., Sung, K., Tamassia, F., Tashkun, S., Vander Auwera, J., Vasilenko, I., Viganin, A., Villanueva, G., Vispoel, B., Wagner, G., Yachmenev, A., and Yurchenko, S.: The HITRAN2020 Molecular Spec-

- troscopic Database, *J QUANT SPECTROSC RA*, 277, 107 949, <https://doi.org/10.1016/j.jqsrt.2021.107949>, 2022.
- Gordon, I. E., Kassi, S., Campargue, A., and Toon, G. C.: First Identification of the Electric Quadrupole Transitions of Oxygen in Solar and Laboratory Spectra, *Journal of Quantitative Spectroscopy and Radiative Transfer*, 111, 1174–1183, <https://doi.org/10.1016/j.jqsrt.2010.01.008>, 2010.
- Grell, G. A., Peckham, S. E., Schmitz, R., McKeen, S. A., Frost, G., Skamarock, W. C., and Eder, B.: Fully Coupled “Online” Chemistry within the WRF Model, *Atmospheric Environment*, 39, 6957–6975, <https://doi.org/10.1016/j.atmosenv.2005.04.027>, 2005.
- Griffith, D. W. T., Pöhler, D., Schmitt, S., Hammer, S., Vardag, S. N., and Platt, U.: Long Open-Path Measurements of Greenhouse Gases in Air Using near-Infrared Fourier Transform Spectroscopy, *ATMOS MEAS TECH*, 11, 1549–1563, <https://doi.org/10.5194/amt-11-1549-2018>, 2018.
- Griffiths, P. R. and De Haseth, J. A.: Fourier Transform Infrared Spectrometry, no. 171 in *Chemical Analysis*, Wiley-Interscience, Hoboken, N.J, 2nd edn., 2007.
- Guanter, L., Irakulis-Loitxate, I., Gorroño, J., Sánchez-García, E., Cusworth, D. H., Varon, D. J., Cogliati, S., and Colombo, R.: Mapping Methane Point Emissions with the PRISMA Spaceborne Imaging Spectrometer, *Remote Sensing of Environment*, 265, 112 671, <https://doi.org/10.1016/j.rse.2021.112671>, 2021.
- Gurney, K. and Shepson, P.: The Power and Promise of Improved Climate Data Infrastructure, *Proc. Natl. Acad. Sci. U.S.A.*, 118, e2114115118, <https://doi.org/10.1073/pnas.2114115118>, 2021.
- Gurney, K. R., Law, R. M., Denning, A. S., Rayner, P. J., Baker, D., Bousquet, P., Bruhwiler, L., Chen, Y.-H., Ciais, P., Fan, S., Fung, I. Y., Gloor, M., Heimann, M., Higuchi, K., John, J., Maki, T., Maksyutov, S., Masarie, K., Peylin, P., Prather, M., Pak, B. C., Randerson, J., Sarmiento, J., Taguchi, S., Takahashi, T., and Yuen, C.-W.: Towards Robust Regional Estimates of CO₂ Sources and Sinks Using Atmospheric Transport Models, *Nature*, 415, 626–630, <https://doi.org/10.1038/415626a>, 2002.
- Gurney, K. R., Liang, J., Roest, G., Song, Y., Mueller, K., and Lauvaux, T.: Under-Reporting of Greenhouse Gas Emissions in U.S. Cities, *NAT COMMUN*, 12, 553, <https://doi.org/10.1038/s41467-020-20871-0>, 2021.

- Hakkarainen, J., Ialongo, I., and Tamminen, J.: Direct Space-based Observations of Anthropogenic CO₂ Emission Areas from OCO-2, *Geophysical Research Letters*, 43, <https://doi.org/10.1002/2016GL070885>, 2016.
- Hall, B. D., Crotwell, A. M., Kitzis, D. R., Mefford, T., Miller, B. R., Schibig, M. F., and Tans, P. P.: Revision of the World Meteorological Organization Global Atmosphere Watch (WMO/GAW) CO₂ Calibration Scale, *ATMOS MEAS TECH*, 14, 3015–3032, <https://doi.org/10.5194/amt-14-3015-2021>, 2021.
- Hammerling, D. M., Michalak, A. M., O'Dell, C., and Kawa, S. R.: Global CO₂ Distributions over Land from the Greenhouse Gases Observing Satellite (GOSAT), *Geophysical Research Letters*, 39, 2012GL051203, <https://doi.org/10.1029/2012GL051203>, 2012.
- Hartmann, J.-M., Tran, H., and Toon, G. C.: Influence of Line Mixing on the Retrievals of Atmospheric CO₂ from Spectra in the 1.6 and 2.1 Mm Regions, *ATMOS CHEM PHYS*, 9, 7303–7312, <https://doi.org/10.5194/acp-9-7303-2009>, 2009.
- Hartmann, J.-M., Tran, H., Armante, R., Boulet, C., Campargue, A., Forget, F., Gianfrani, L., Gordon, I., Guerlet, S., Gustafsson, M., Hodges, J. T., Kassi, S., Lisak, D., Thibault, F., and Toon, G. C.: Recent Advances in Collisional Effects on Spectra of Molecular Gases and Their Practical Consequences, *Journal of Quantitative Spectroscopy and Radiative Transfer*, 213, 178–227, <https://doi.org/10.1016/j.jqsrt.2018.03.016>, 2018.
- Hartmann, J.-M., Boulet, C., and Robert, D.: *Collisional Effects on Molecular Spectra: Laboratory Experiments and Models, Consequences for Applications*, Elsevier, Amsterdam Oxford Cambridge, MA, second edition edn., 2021.
- Hase, F.: Messung des Apparateprofils eines hochauflösenden FTIR-Spektrometers, diploma thesis, Universität Karlsruhe, 1995.
- Hase, F.: Inversion von Spurengasprofilen aus hochaufgelösten bodengebundenen FTIR-Messungen in Absorption, Ph.D. thesis, Universität Karlsruhe, 2000.
- Hase, F., Blumenstock, T., and Paton-Walsh, C.: Analysis of the Instrumental Line Shape of High-Resolution Fourier Transform IR Spectrometers with Gas Cell Measurements and New Retrieval Software, *APPL OPTICS*, 38, 3417, <https://doi.org/10.1364/AO.38.003417>, 1999.

- Hase, F., Frey, M., Blumenstock, T., Groß, J., Kiel, M., Kohlhepp, R., Mengistu Tsidu, G., Schäfer, K., Sha, M. K., and Orphal, J.: Application of Portable FTIR Spectrometers for Detecting Greenhouse Gas Emissions of the Major City Berlin, *Atmos. Meas. Tech.*, 8, 3059–3068, <https://doi.org/10.5194/amt-8-3059-2015>, 2015.
- Haustein, K., Allen, M. R., Forster, P. M., Otto, F. E. L., Mitchell, D. M., Matthews, H. D., and Frame, D. J.: A Real-Time Global Warming Index, *Sci Rep*, 7, 15417, <https://doi.org/10.1038/s41598-017-14828-5>, 2017.
- Haustein, K., Otto, F. E. L., Venema, V., Jacobs, P., Cowtan, K., Hausfather, Z., Way, R. G., White, B., Subramanian, A., and Schurer, A. P.: A Limited Role for Unforced Internal Variability in Twentieth-Century Warming, *Journal of Climate*, 32, 4893–4917, <https://doi.org/10.1175/JCLI-D-18-0555.1>, 2019.
- Herzberg, G.: *Molecular Spectra and Molecular Structure. 1: Spectra of Diatomic Molecules*, Krieger, Malabar, Fla, 2. ed., repr. with corr edn., 1989.
- Herzberg, G.: *Molecular Spectra and Molecular Structure. 2: Infrared and Raman Spectra of Polyatomic Molecules*, Krieger, Malabar, Fla, repr. ed. with corr edn., 1991.
- Hobbs, P. C.: *Photodiode Front Ends: The Real Story*, Optics & Photonics News, 12, 44, <https://doi.org/10.1364/OPN.12.4.000044>, 2001.
- Hobbs, P. C.: *Building Electro-Optical Systems: Making It All Work.*, John Wiley & Sons, 2 edn., 2009.
- Hoheisel, A.: *Evaluation of Greenhouse Gas Time Series to Characterise Local and Regional Emissions*, Ph.D. thesis, Heidelberg University, URL <http://archiv.ub.uni-heidelberg.de/volltextserver/id/eprint/30321> (lastaccessdate:2023-08-02), 2021.
- Hoheisel, A., Yeman, C., Dinger, F., Eckhardt, H., and Schmidt, M.: An Improved Method for Mobile Characterisation of $\delta^{13}\text{C}\text{H}_4$ Source Signatures and Its Application in Germany, *ATMOS MEAS TECH*, 12, 1123–1139, <https://doi.org/10.5194/amt-12-1123-2019>, 2019.
- Hu, H., Landgraf, J., Detmers, R., Borsdorff, T., Aan De Brugh, J., Aben, I., Butz, A., and Hasekamp, O.: Toward Global Mapping of Methane With TROPOMI: First Results and Intersatellite Comparison to GOSAT, *Geophysical Research Letters*, 45, 3682–3689, <https://doi.org/10.1002/2018GL077259>, 2018.

- Intergovernmental Panel On Climate Change: Global Warming of 1.5°C: IPCC Special Report on Impacts of Global Warming of 1.5°C above Pre-industrial Levels in Context of Strengthening Response to Climate Change, Sustainable Development, and Efforts to Eradicate Poverty, Cambridge University Press, 1 edn., <https://doi.org/10.1017/9781009157940>, 2022.
- Intergovernmental Panel On Climate Change: Climate Change 2021 – The Physical Science Basis: Working Group I Contribution to the Sixth Assessment Report of the Intergovernmental Panel on Climate Change, Cambridge University Press, 1 edn., <https://doi.org/10.1017/9781009157896>, 2023.
- Jouzel, J.: A Brief History of Ice Core Science over the Last 50 Yr, *Clim. Past*, 9, 2525–2547, <https://doi.org/10.5194/cp-9-2525-2013>, 2013.
- Jungmann, M., Vardag, S. N., Kutzner, F., Keppler, F., Schmidt, M., Aeschbach, N., Gerhard, U., Zipf, A., Lautenbach, S., Siegmund, A., Goeschl, T., and Butz, A.: Zooming-in for Climate Action—Hyperlocal Greenhouse Gas Data for Mitigation Action?, *Clim Action*, 1, 8, <https://doi.org/10.1007/s44168-022-00007-4>, 2022.
- Kaminski, T., Rayner, P. J., Heimann, M., and Enting, I. G.: On Aggregation Errors in Atmospheric Transport Inversions, *J. Geophys. Res.*, 106, 4703–4715, <https://doi.org/10.1029/2000JD900581>, 2001.
- Karman, T., Gordon, I. E., van der Avoird, A., Baranov, Y. I., Boulet, C., Drouin, B. J., Groenenboom, G. C., Gustafsson, M., Hartmann, J.-M., Kurucz, R. L., Rothman, L. S., Sun, K., Sung, K., Thalman, R., Tran, H., Wishnow, E. H., Wordsworth, R., Vigasin, A. A., Volkamer, R., and van der Zande, W. J.: Update of the HITRAN Collision-Induced Absorption Section, *Icarus*, 328, 160–175, <https://doi.org/10.1016/j.icarus.2019.02.034>, 2019.
- Kaufman, D. S. and McKay, N. P.: Technical Note: Past and Future Warming – Direct Comparison on Multi-Century Timescales, *Clim. Past*, 18, 911–917, <https://doi.org/10.5194/cp-18-911-2022>, 2022.
- Keeling, R. F. and Keeling, C. D.: Atmospheric Monthly In Situ CO₂ Data - Mauna Loa Observatory, Hawaii. In Scripps CO₂ Program Data, <https://doi.org/10.6075/J08W3BHW>, 2017.
- Kiel, M., Eldering, A., Roten, D. D., Lin, J. C., Feng, S., Lei, R., Lauvaux, T., Oda, T., Roehl, C. M., Blavier, J.-F., and Iraci, L. T.: Urban-Focused Satellite CO₂

- Observations from the Orbiting Carbon Observatory-3: A First Look at the Los Angeles Megacity, *REMOTE SENS ENVIRON*, 258, 112 314, <https://doi.org/10.1016/j.rse.2021.112314>, 2021.
- Kochanov, R., Gordon, I., Rothman, L., Wcisło, P., Hill, C., and Wilzewski, J.: HITRAN Application Programming Interface (HAPI): A Comprehensive Approach to Working with Spectroscopic Data, *J QUANT SPECTROSC RA*, 177, 15–30, <https://doi.org/10.1016/j.jqsrt.2016.03.005>, 2016.
- Kort, E. A., Frankenberg, C., Miller, C. E., and Oda, T.: Space-based Observations of Megacity Carbon Dioxide, *Geophysical Research Letters*, 39, 2012GL052738, <https://doi.org/10.1029/2012GL052738>, 2012.
- Kostinek, J., Roiger, A., Eckl, M., Fiehn, A., Luther, A., Wildmann, N., Klausner, T., Fix, A., Knote, C., Stohl, A., and Butz, A.: Estimating Upper Silesian Coal Mine Methane Emissions from Airborne in Situ Observations and Dispersion Modeling, *Atmos. Chem. Phys.*, 21, 8791–8807, <https://doi.org/10.5194/acp-21-8791-2021>, 2021.
- Kountouris, P., Gerbig, C., Rödenbeck, C., Karstens, U., Koch, T. F., and Heimann, M.: Atmospheric CO₂ Inversions on the Mesoscale Using Data-Driven Prior Uncertainties: Quantification of the European Terrestrial CO₂ Fluxes, *Atmos. Chem. Phys.*, 18, 3047–3064, <https://doi.org/10.5194/acp-18-3047-2018>, 2018.
- Kuhn, J., Bobrowski, N., Boudoire, G., Calabrese, S., Giuffrida, G., Liuzzo, M., Karume, K., Tedesco, D., Wagner, T., and Platt, U.: High-Spectral-Resolution Fabry-Pérot Interferometers Overcome Fundamental Limitations of Present Volcanic Gas Remote Sensing Techniques, *Front. Earth Sci.*, 11, 1039 093, <https://doi.org/10.3389/feart.2023.1039093>, 2023.
- Lian, J., Bréon, F.-M., Broquet, G., Zaccheo, T. S., Dobler, J., Ramonet, M., Stauffer, J., Santaren, D., Xueref-Remy, I., and Ciais, P.: Analysis of Temporal and Spatial Variability of Atmospheric CO₂ Concentration within Paris from the Green-LITE™ Laser Imaging Experiment, *ATMOS CHEM PHYS*, 19, 13 809–13 825, <https://doi.org/10.5194/acp-19-13809-2019>, 2019.
- Louergue, L., Schilt, A., Spahni, R., Masson-Delmotte, V., Blunier, T., Lemieux, B., Barnola, J.-M., Raynaud, D., Stocker, T. F., and Chappellaz, J.: Orbital and Millennial-Scale Features of Atmospheric CH₄ over the Past 800,000 Years, *Nature*, 453, 383–386, <https://doi.org/10.1038/nature06950>, 2008.

- Luther, A., Kostinek, J., Kleinschek, R., Defratyka, S., Stanisavljević, M., Forstmaier, A., Dandocsi, A., Scheidweiler, L., Dubravica, D., Wildmann, N., Hase, F., Frey, M. M., Chen, J., Dietrich, F., Nečki, J., Swolkień, J., Knote, C., Vardag, S. N., Roiger, A., and Butz, A.: Observational Constraints on Methane Emissions from Polish Coal Mines Using a Ground-Based Remote Sensing Network, *Atmos. Chem. Phys.*, 22, 5859–5876, <https://doi.org/10.5194/acp-22-5859-2022>, 2022.
- Lüthi, D., Le Floch, M., Bereiter, B., Blunier, T., Barnola, J.-M., Siegenthaler, U., Raynaud, D., Jouzel, J., Fischer, H., Kawamura, K., and Stocker, T. F.: High-Resolution Carbon Dioxide Concentration Record 650,000–800,000 Years before Present, *Nature*, 453, 379–382, <https://doi.org/10.1038/nature06949>, 2008.
- Malarich, N. A., Washburn, B. R., Cossel, K. C., Mead, G. J., Giorgetta, F. R., Herman, D. I., Newbury, N. R., and Coddington, I.: Validation of Open-Path Dual-Comb Spectroscopy against an O₂ Background, *OPT EXPRESS*, 31, 5042, <https://doi.org/10.1364/OE.480301>, 2023.
- Mann, M. E.: Climate Over the Past Two Millennia, *Annu. Rev. Earth Planet. Sci.*, 35, 111–136, <https://doi.org/10.1146/annurev.earth.35.031306.140042>, 2007.
- Mann, M. E., Bradley, R. S., and Hughes, M. K.: Northern Hemisphere Temperatures during the Past Millennium: Inferences, Uncertainties, and Limitations, *Geophysical Research Letters*, 26, 759–762, <https://doi.org/10.1029/1999GL900070>, 1999.
- Marcotullio, P. J., Sarzynski, A., Albrecht, J., Schulz, N., and Garcia, J.: The Geography of Global Urban Greenhouse Gas Emissions: An Exploratory Analysis, *CLIMATIC CHANGE*, 121, 621–634, <https://doi.org/10.1007/s10584-013-0977-z>, 2013.
- Masarie, K. A., Peters, W., Jacobson, A. R., and Tans, P. P.: ObsPack: A Framework for the Preparation, Delivery, and Attribution of Atmospheric Greenhouse Gas Measurements, *Earth Syst. Sci. Data*, 6, 375–384, <https://doi.org/10.5194/essd-6-375-2014>, 2014.
- Mattick, A. T., Sanchez, A., Kurnit, N. A., and Javan, A.: Velocity Dependence of Collision-Broadening Cross Section Observed in an Infrared Transition of NH₃ Gas at Room Temperature, *Applied Physics Letters*, 23, 675–678, <https://doi.org/10.1063/1.1654787>, 1973.

- Merten, A., Tschirter, J., and Platt, U.: Design of Differential Optical Absorption Spectroscopy Long-Path Telescopes Based on Fiber Optics, *APPL OPTICS*, 50, 738, <https://doi.org/10.1364/AO.50.000738>, 2011.
- Mertz, L.: Auxiliary Computation for Fourier Spectrometry, *Infrared Physics*, 7, 17–23, [https://doi.org/10.1016/0020-0891\(67\)90026-7](https://doi.org/10.1016/0020-0891(67)90026-7), 1967.
- Messerschmidt, J., Geibel, M. C., Blumenstock, T., Chen, H., Deutscher, N. M., Engel, A., Feist, D. G., Gerbig, C., Gisi, M., Hase, F., Katrynski, K., Kolle, O., Lavrič, J. V., Notholt, J., Palm, M., Ramonet, M., Rettinger, M., Schmidt, M., Sussmann, R., Toon, G. C., Truong, F., Warneke, T., Wennberg, P. O., Wunch, D., and Xueref-Remy, I.: Calibration of TCCON Column-Averaged CO₂: The First Aircraft Campaign over European TCCON Sites, *Atmos. Chem. Phys.*, 11, 10765–10777, <https://doi.org/10.5194/acp-11-10765-2011>, 2011.
- Metz, E.-M., Vardag, S. N., Basu, S., Jung, M., Ahrens, B., El-Madany, T., Sitch, S., Arora, V. K., Briggs, P. R., Friedlingstein, P., Goll, D. S., Jain, A. K., Kato, E., Lombardozzi, D., Nabel, J. E. M. S., Poulter, B., Séférian, R., Tian, H., Wiltshire, A., Yuan, W., Yue, X., Zaehle, S., Deutscher, N. M., Griffith, D. W. T., and Butz, A.: Soil Respiration–Driven CO₂ Pulses Dominate Australia’s Flux Variability, *Science*, 379, 1332–1335, <https://doi.org/10.1126/science.add7833>, 2023.
- Morse, P. M.: Diatomic Molecules According to the Wave Mechanics. II. Vibrational Levels, *Phys. Rev.*, 34, 57–64, <https://doi.org/10.1103/PhysRev.34.57>, 1929.
- Mueller, K. L., Lauvaux, T., Gurney, K. R., Roest, G., Ghosh, S., Gourджи, S. M., Karion, A., DeCola, P., and Whetstone, J.: An Emerging GHG Estimation Approach Can Help Cities Achieve Their Climate and Sustainability Goals, *ENVIRON RES LETT*, 16, 084003, <https://doi.org/10.1088/1748-9326/ac0f25>, 2021.
- Nassar, R., Hill, T. G., McLinden, C. A., Wunch, D., Jones, D. B. A., and Crisp, D.: Quantifying CO₂ Emissions From Individual Power Plants From Space, *GEOPHYS RES LETT*, 44, <https://doi.org/10.1002/2017GL074702>, 2017.
- Nasse, J.-M., Eger, P. G., Pöhler, D., Schmitt, S., Frieß, U., and Platt, U.: Recent Improvements of Long-Path DOAS Measurements: Impact on Accuracy and Stability of Short-Term and Automated Long-Term Observations, *Atmos. Meas. Tech.*, 12, 4149–4169, <https://doi.org/10.5194/amt-12-4149-2019>, 2019.

- Ngo, N., Lisak, D., Tran, H., and Hartmann, J.-M.: An Isolated Line-Shape Model to Go beyond the Voigt Profile in Spectroscopic Databases and Radiative Transfer Codes, *Journal of Quantitative Spectroscopy and Radiative Transfer*, 129, 89–100, <https://doi.org/10.1016/j.jqsrt.2013.05.034>, 2013.
- Ngo, N., Lisak, D., Tran, H., and Hartmann, J.-M.: Erratum to “An Isolated Line-Shape Model to Go beyond the Voigt Profile in Spectroscopic Databases and Radiative Transfer Codes” [*J. Quant. Spectrosc. Radiat. Transf.* 129 (2013) 89–100], *Journal of Quantitative Spectroscopy and Radiative Transfer*, 134, 105, <https://doi.org/10.1016/j.jqsrt.2013.10.016>, 2014.
- Norton, R. H. and Beer, R.: New Apodizing Functions for Fourier Spectrometry, *J. Opt. Soc. Am.*, 66, 259, <https://doi.org/10.1364/JOSA.66.000259>, 1976.
- Oda, T., Maksyutov, S., and Andres, R. J.: The Open-source Data Inventory for Anthropogenic CO₂, Version 2016 (ODIAC2016): A Global Monthly Fossil Fuel CO₂ Gridded Emissions Data Product for Tracer Transport Simulations and Surface Flux Inversions, *Earth Syst. Sci. Data*, 10, 87–107, <https://doi.org/10.5194/essd-10-87-2018>, 2018.
- Oda, T., Bun, R., Kinakh, V., Topylko, P., Halushchak, M., Marland, G., Lauvaux, T., Jonas, M., Maksyutov, S., Nahorski, Z., Lesiv, M., Danylo, O., and Horabik-Pyzel, J.: Errors and Uncertainties in a Gridded Carbon Dioxide Emissions Inventory, *Mitig Adapt Strateg Glob Change*, 24, 1007–1050, <https://doi.org/10.1007/s11027-019-09877-2>, 2019.
- Oettl, D.: Documentation of the Prognostic Mesoscale Model GRAMM (Graz Mesoscale Model) Version 19.1, 2019a.
- Oettl, D.: Documentation of the Lagrangian Particle Model GRAL (Graz Lagrangian Model) Vs. 19.1, 2019b.
- Olson, J., Ou, Y. H., Azarm, A., and Kieu, K.: Bi-Directional Mode-Locked Thulium Fiber Laser as a Single-Cavity Dual-Comb Source, *IEEE Photon. Technol. Lett.*, 30, 1772–1775, <https://doi.org/10.1109/LPT.2018.2868940>, 2018.
- Park, C., Park, S.-Y., Gurney, K. R., Gerbig, C., DiGangi, J. P., Choi, Y., and Lee, H. W.: Numerical Simulation of Atmospheric CO₂ Concentration and Flux over the Korean Peninsula Using WRF-VPRM Model during Korus-AQ 2016 Campaign, *PLoS ONE*, 15, e0228106, <https://doi.org/10.1371/journal.pone.0228106>, 2020.

- Petty, G. W.: *A First Course in Atmospheric Radiation*, Sundog Publ, Madison, Wisc, 2. ed edn., 2006.
- Rebmann, C., Aubinet, M., Schmid, H., Arriga, N., Aurela, M., Burba, G., Clement, R., De Ligne, A., Fratini, G., Gielen, B., Grace, J., Graf, A., Gross, P., Haapanala, S., Herbst, M., Hörtnagl, L., Ibrom, A., Joly, L., Kljun, N., Kolle, O., Kowalski, A., Lindroth, A., Loustau, D., Mammarella, I., Mauder, M., Merbold, L., Metzger, S., Mölder, M., Montagnani, L., Papale, D., Pavelka, M., Peichl, M., Roland, M., Serrano-Ortiz, P., Siebicke, L., Steinbrecher, R., Tuovinen, J.-P., Vesala, T., Wohlfahrt, G., and Franz, D.: ICOS Eddy Covariance Flux-Station Site Setup: A Review, *International Agrophysics*, 32, 471–494, <https://doi.org/10.1515/intag-2017-0044>, 2018.
- Rieger, D., Bangert, M., Bischoff-Gauss, I., Förstner, J., Lundgren, K., Reinert, D., Schröter, J., Vogel, H., Zängl, G., Ruhnke, R., and Vogel, B.: ICON-ART 1.0 – a New Online-Coupled Model System from the Global to Regional Scale, Preprint, *Atmospheric Sciences*, <https://doi.org/10.5194/gmdd-8-567-2015>, 2015.
- Rodenbeck, C., Houweling, S., Gloor, M., and Heimann, M.: CO₂ Flux History 1982–2001 Inferred from Atmospheric Data Using a Global Inversion of Atmospheric Transport, *Atmos. Chem. Phys.*, 2003.
- Rohde, R. A. and Hausfather, Z.: The Berkeley Earth Land/Ocean Temperature Record, *Earth Syst. Sci. Data*, 12, 3469–3479, <https://doi.org/10.5194/essd-12-3469-2020>, 2020.
- Rothman, L., Jacquemart, D., Barbe, A., Chris Benner, D., Birk, M., Brown, L., Carleer, M., Chackerian, C., Chance, K., Coudert, L., Dana, V., Devi, V., Flaud, J.-M., Gamache, R., Goldman, A., Hartmann, J.-M., Jucks, K., Maki, A., Mandin, J.-Y., Massie, S., Orphal, J., Perrin, A., Rinsland, C., Smith, M., Tennyson, J., Tolchenov, R., Toth, R., Vander Auwera, J., Varanasi, P., and Wagner, G.: The HITRAN 2004 Molecular Spectroscopic Database, *Journal of Quantitative Spectroscopy and Radiative Transfer*, 96, 139–204, <https://doi.org/10.1016/j.jqsrt.2004.10.008>, 2005.
- Rothman, L., Gordon, I., Babikov, Y., Barbe, A., Chris Benner, D., Bernath, P., Birk, M., Bizzocchi, L., Boudon, V., Brown, L., Campargue, A., Chance, K., Cohen, E., Coudert, L., Devi, V., Drouin, B., Fayt, A., Flaud, J.-M., Gamache, R., Harrison, J., Hartmann, J.-M., Hill, C., Hodges, J., Jacquemart, D., Jolly, A., Lamouroux,

- J., Le Roy, R., Li, G., Long, D., Lyulin, O., Mackie, C., Massie, S., Mikhailenko, S., Müller, H., Naumenko, O., Nikitin, A., Orphal, J., Perevalov, V., Perrin, A., Polovtseva, E., Richard, C., Smith, M., Starikova, E., Sung, K., Tashkun, S., Tenyson, J., Toon, G., Tyuterev, V.I., and Wagner, G.: The HITRAN2012 Molecular Spectroscopic Database, *Journal of Quantitative Spectroscopy and Radiative Transfer*, 130, 4–50, <https://doi.org/10.1016/j.jqsrt.2013.07.002>, 2013.
- Rothman, L. S., Gamache, R. R., Goldman, A., Brown, L. R., Toth, R. A., Pickett, H. M., Poynter, R. L., Flaud, J.-M., Camy-Peyret, C., Barbe, A., Husson, N., Rinsland, C. P., and Smith, M. A. H.: The HITRAN Database: 1986 Edition, *Appl. Opt.*, 26, 4058, <https://doi.org/10.1364/AO.26.004058>, 1987.
- Sargent, M., Barrera, Y., Nehrkorn, T., Hutyrá, L. R., Gately, C. K., Jones, T., McKain, K., Sweeney, C., Hegarty, J., Hardiman, B., Wang, J. A., and Wofsy, S. C.: Anthropogenic and Biogenic CO₂ Fluxes in the Boston Urban Region, *Proc. Natl. Acad. Sci. U.S.A.*, 115, 7491–7496, <https://doi.org/10.1073/pnas.1803715115>, 2018.
- Schilt, A., Baumgartner, M., Blunier, T., Schwander, J., Spahni, R., Fischer, H., and Stocker, T. F.: Glacial–Interglacial and Millennial-Scale Variations in the Atmospheric Nitrous Oxide Concentration during the Last 800,000 Years, *Quaternary Science Reviews*, 29, 182–192, <https://doi.org/10.1016/j.quascirev.2009.03.011>, 2010.
- Schmitt, T. D., Kuhn, J., Kleinschek, R., Löw, B. A., Schmitt, S., Cranton, W., Schmidt, M., Vardag, S. N., Hase, F., Griffith, D. W. T., and Butz, A.: An Open-Path Observatory for Greenhouse Gases Based on near-Infrared Fourier Transform Spectroscopy, *Atmospheric Measurement Techniques*, 16, 6097–6110, <https://doi.org/10.5194/amt-16-6097-2023>, 2023.
- Shekhar, A., Chen, J., Paetzold, J. C., Dietrich, F., Zhao, X., Bhattacharjee, S., Ruisinger, V., and Wofsy, S. C.: Anthropogenic CO₂ Emissions Assessment of Nile Delta Using XCO₂ and SIF Data from OCO-2 Satellite, *Environ. Res. Lett.*, 15, 095010, <https://doi.org/10.1088/1748-9326/ab9cfe>, 2020.
- Shepherd, T. G.: Atmospheric Circulation as a Source of Uncertainty in Climate Change Projections, *Nature Geosci*, 7, 703–708, <https://doi.org/10.1038/ngeo2253>, 2014.
- Shin, H. H. and Dudhia, J.: Evaluation of PBL Parameterizations in WRF at Sub-kilometer Grid Spacings: Turbulence Statistics in the Dry Convective Bound-

- ary Layer, *Monthly Weather Review*, 144, 1161–1177, <https://doi.org/10.1175/MWR-D-15-0208.1>, 2016.
- Shusterman, A. A., Teige, V. E., Turner, A. J., Newman, C., Kim, J., and Cohen, R. C.: The BERkeley Atmospheric CO₂ Observation Network: Initial Evaluation, *ATMOS CHEM PHYS*, 16, 13 449–13 463, <https://doi.org/10.5194/acp-16-13449-2016>, 2016.
- Sindelarova, K., Markova, J., Simpson, D., Huszar, P., Karlicky, J., Darras, S., and Granier, C.: High-Resolution Biogenic Global Emission Inventory for the Time Period 2000–2019 for Air Quality Modelling, *Earth Syst. Sci. Data*, 14, 251–270, <https://doi.org/10.5194/essd-14-251-2022>, 2022.
- Solazzo, E., Crippa, M., Guizzardi, D., Muntean, M., Choulga, M., and Janssens-Maenhout, G.: Uncertainties in the Emissions Database for Global Atmospheric Research (EDGAR) Emission Inventory of Greenhouse Gases, *Atmos. Chem. Phys.*, 21, 5655–5683, <https://doi.org/10.5194/acp-21-5655-2021>, 2021.
- Stagakis, S., Chrysoulakis, N., Spyridakis, N., Feigenwinter, C., and Vogt, R.: Eddy Covariance Measurements and Source Partitioning of CO₂ Emissions in an Urban Environment: Application for Heraklion, Greece, *Atmospheric Environment*, 201, 278–292, <https://doi.org/10.1016/j.atmosenv.2019.01.009>, 2019.
- Stagakis, S., Feigenwinter, C., Vogt, R., and Kalberer, M.: A High-Resolution Monitoring Approach of Urban CO₂ Fluxes. Part 1 - Bottom-up Model Development, *Science of The Total Environment*, 858, 160 216, <https://doi.org/10.1016/j.scitotenv.2022.160216>, 2023.
- Stauffer, J., Broquet, G., Bréon, F.-M., Puygrenier, V., Chevallier, F., Xueref-Rémy, I., Dieudonné, E., Lopez, M., Schmidt, M., Ramonet, M., Perrussel, O., Lac, C., Wu, L., and Ciais, P.: The First 1-Year-Long Estimate of the Paris Region Fossil Fuel CO₂ Emissions Based on Atmospheric Inversion, *Atmos. Chem. Phys.*, 16, 14 703–14 726, <https://doi.org/10.5194/acp-16-14703-2016>, 2016.
- Super, I., Dellaert, S. N. C., Visschedijk, A. J. H., and Denier Van Der Gon, H. A. C.: Uncertainty Analysis of a European High-Resolution Emission Inventory of CO₂ and CO to Support Inverse Modelling and Network Design, *Atmos. Chem. Phys.*, 20, 1795–1816, <https://doi.org/10.5194/acp-20-1795-2020>, 2020.
- Swinbank, W. C.: THE MEASUREMENT OF VERTICAL TRANSFER OF HEAT AND WATER VAPOR BY EDDIES IN THE LOWER ATMOSPHERE, *J. Meteor.*,

8, 135–145, [https://doi.org/10.1175/1520-0469\(1951\)008<0135:TMOVTO>2.0.CO;2](https://doi.org/10.1175/1520-0469(1951)008<0135:TMOVTO>2.0.CO;2), 1951.

Tennyson, J., Bernath, P. F., Campargue, A., Császár, A. G., Daumont, L., Gamache, R. R., Hodges, J. T., Lisak, D., Naumenko, O. V., Rothman, L. S., Tran, H., Zobov, N. F., Buldyreva, J., Boone, C. D., De Vizia, M. D., Gianfrani, L., Hartmann, J.-M., McPheat, R., Weidmann, D., Murray, J., Ngo, N. H., and Polyansky, O. L.: Recommended Isolated-Line Profile for Representing High-Resolution Spectroscopic Transitions (IUPAC Technical Report), *Pure and Applied Chemistry*, 86, 1931–1943, <https://doi.org/10.1515/pac-2014-0208>, 2014.

Truong, G.-W., Waxman, E. M., Cossel, K. C., Baumann, E., Klose, A., Giorgetta, F. R., Swann, W. C., Newbury, N. R., and Coddington, I.: Accurate Frequency Referencing for Fieldable Dual-Comb Spectroscopy, *OPT EXPRESS*, 24, 30 495, <https://doi.org/10.1364/OE.24.030495>, 2016.

Ulrich, V., Brückner, J., Schultz, M., Vardag, S. N., Ludwig, C., Fürle, J., Zia, M., Lautenbach, S., and Zipf, A.: Private Vehicles Greenhouse Gas Emission Estimation at Street Level for Berlin Based on Open Data, *IJGI*, 12, 138, <https://doi.org/10.3390/ijgi12040138>, 2023.

United Nations Framework Convention on Climate Change (UNFCCC): The Paris Agreement, 2015.

Vardag, S. N. and Maiwald, R.: Optimising Urban Measurement Networks for CO₂ Flux Estimation: A High-Resolution Observing System Simulation Experiment Using GRAMM/GRAL, Preprint, *Atmospheric sciences*, <https://doi.org/10.5194/gmd-2023-192>, 2023.

Velasco, E. and Roth, M.: Cities as Net Sources of CO₂ : Review of Atmospheric CO₂ Exchange in Urban Environments Measured by Eddy Covariance Technique, *Geography Compass*, 4, 1238–1259, <https://doi.org/10.1111/j.1749-8198.2010.00384.x>, 2010.

Wang, J., Christopher, S. A., Nair, U. S., Reid, J. S., Prins, E. M., Szykman, J., and Hand, J. L.: Mesoscale Modeling of Central American Smoke Transport to the United States: 1. “Top-down” Assessment of Emission Strength and Diurnal Variation Impacts, *J. Geophys. Res.*, 111, 2005JD006 416, <https://doi.org/10.1029/2005JD006416>, 2006.

- Wang, J. S., Kawa, S. R., Collatz, G. J., Sasakawa, M., Gatti, L. V., Machida, T., Liu, Y., and Manyin, M. E.: A Global Synthesis Inversion Analysis of Recent Variability in CO₂ Fluxes Using GOSAT and in Situ Observations, *Atmos. Chem. Phys.*, 18, 11 097–11 124, <https://doi.org/10.5194/acp-18-11097-2018>, 2018.
- Waxman, E. M., Cossel, K. C., Giorgetta, F., Truong, G.-W., Swann, W. C., Codrington, I., and Newbury, N. R.: Estimating Vehicle Carbon Dioxide Emissions from Boulder, Colorado, Using Horizontal Path-Integrated Column Measurements, *ATMOS CHEM PHYS*, 19, 4177–4192, <https://doi.org/10.5194/acp-19-4177-2019>, 2019.
- Weller, Z. D., Yang, D. K., and Von Fischer, J. C.: An Open Source Algorithm to Detect Natural Gas Leaks from Mobile Methane Survey Data, *PLoS ONE*, 14, e0212 287, <https://doi.org/10.1371/journal.pone.0212287>, 2019.
- Wiacek, A., Li, L., Tobin, K., and Mitchell, M.: Characterization of Trace Gas Emissions at an Intermediate Port, *ATMOS CHEM PHYS*, 18, 13 787–13 812, <https://doi.org/10.5194/acp-18-13787-2018>, 2018.
- Wietzel, J. B. and Schmidt, M.: Methane Emission Mapping and Quantification in Two Medium-Sized Cities in Germany: Heidelberg and Schwetzingen, *Atmospheric Environment: X*, 20, 100 228, <https://doi.org/10.1016/j.aeaoa.2023.100228>, 2023.
- Wunch, D., Toon, G. C., Wennberg, P. O., Wofsy, S. C., Stephens, B. B., Fischer, M. L., Uchino, O., Abshire, J. B., Bernath, P., Biraud, S. C., Blavier, J.-F. L., Boone, C., Bowman, K. P., Browell, E. V., Campos, T., Connor, B. J., Daube, B. C., Deutscher, N. M., Diao, M., Elkins, J. W., Gerbig, C., Gottlieb, E., Griffith, D. W. T., Hurst, D. F., Jiménez, R., Keppel-Aleks, G., Kort, E., Macatangay, R., Machida, T., Matsueda, H., Moore, F., Morino, I., Park, S., Robinson, J., Roehl, C. M., Sawa, Y., Sherlock, V., Sweeney, C., Tanaka, T., and Zondlo, M. A.: Calibration of the Total Carbon Column Observing Network Using Aircraft Profile Data, Preprint, *Gases/Remote Sensing/Validation and Intercomparisons*, <https://doi.org/10.5194/amtd-3-2603-2010>, 2010.
- Wunch, D., Toon, G. C., Blavier, J.-F. L., Washenfelder, R. A., Notholt, J., Connor, B. J., Griffith, D. W. T., Sherlock, V., and Wennberg, P. O.: The Total Carbon Column Observing Network, *PHILOS T R SOC A*, 369, 2087–2112, <https://doi.org/10.1098/rsta.2010.0240>, 2011.

- Xu, C., Kohler, T. A., Lenton, T. M., Svenning, J.-C., and Scheffer, M.: Future of the Human Climate Niche, *Proc Natl Acad Sci USA*, 117, 11 350–11 355, <https://doi.org/10.1073/pnas.1910114117>, 2020.
- Yokelson, R. J., Susott, R., Ward, D. E., Reardon, J., and Griffith, D. W. T.: Emissions from Smoldering Combustion of Biomass Measured by Open-path Fourier Transform Infrared Spectroscopy, *J. Geophys. Res.*, 102, 18 865–18 877, <https://doi.org/10.1029/97JD00852>, 1997.
- You, Y., Moussa, S. G., Zhang, L., Fu, L., Beck, J., and Staebler, R. M.: Quantifying Fugitive Gas Emissions from an Oil Sands Tailings Pond with Open-Path Fourier Transform Infrared Measurements, *ATMOS MEAS TECH*, 14, 945–959, <https://doi.org/10.5194/amt-14-945-2021>, 2021.
- Zhao, X., Marshall, J., Hachinger, S., Gerbig, C., Frey, M., Hase, F., and Chen, J.: Analysis of Total Column CO₂ and CH₄ Measurements in Berlin with WRF-GHG, *Atmos. Chem. Phys.*, 19, 11 279–11 302, <https://doi.org/10.5194/acp-19-11279-2019>, 2019.
- Zhao, X., Chen, J., Marshall, J., Gałkowski, M., Hachinger, S., Dietrich, F., Shekhar, A., Gensheimer, J., Wenzel, A., and Gerbig, C.: Understanding Greenhouse Gas (GHG) Column Concentrations in Munich Using the Weather Research and Forecasting (WRF) Model, *Atmos. Chem. Phys.*, 23, 14 325–14 347, <https://doi.org/10.5194/acp-23-14325-2023>, 2023.
- Zheng, T., Nassar, R., and Baxter, M.: Estimating Power Plant CO₂ Emission Using OCO-2 XCO₂ and High Resolution WRF-Chem Simulations, *Environ. Res. Lett.*, 14, 085 001, <https://doi.org/10.1088/1748-9326/ab25ae>, 2019.
- Zhong, J., Cai, X.-M., and Bloss, W. J.: Coupling Dynamics and Chemistry in the Air Pollution Modelling of Street Canyons: A Review, *Environmental Pollution*, 214, 690–704, <https://doi.org/10.1016/j.envpol.2016.04.052>, 2016.